Numerical Study on the Dynamics of Cellular Structures in Gaseous Detonations

Thesis by

Kazuaki Inaba

School of Science

for Open and Environmental Systems

Graduate School of Science and Technology

Keio University

Yokohama, JAPAN

2004

(Submitted November 11, 2004)

Acknowledgements

There are several people who deserve thanks for the assistance they given me over the years at Keio University. First and foremost, my advisor Akiko Matsuo has supported in all aspects of my research, especially in CFD, presentation skills, and intellectual vitality. Joseph E. Shepherd at Caltech gave me a great chance to study abroad and encouraged me to deliberate experimental and numerical problems carefully, logically, and aggressively. Katsumi Tanaka at AIST has provided his software package AISTJAN and KHT. Takuma Endo at Hiroshima University and Jiro Kasahara at University of Tsukuba gave me the insight into the theoretical and experimental works of PDEs. Kozo Fujii at JAXA & Yoshiaki Tamura at Toyo University have provided their software package Post_kun. All numerical results are visualized by the Post_kun. Nobuyuki Tsuboi at JAXA has showed exiting numerical results and stimulated me to perform detonation simulations.

I would like to thank all researchers in Matsuo laboratory for their assistance with issues ranging from detonations to general computing, especially Yu Daimon, Yusuke Kamiyama, and Shigeru Sato. I deeply appreciate useful discussion for Toshi Fujiwara at Ates, Shiro Taki and Tomoaki Yatsufusa at Hiroshima University, Shigeharu Oyagi and Tsuyoshi Sakurai at Saitama University, A. Koichi Hayashi at Aoyama Gakuin University, Takao Tsuboi and Kazuhiro Ishii at Yokohama National University, Mitsuo Koshi at Tokyo University, Masahide Katayama at CRC, Shigeru Aso at Kyushu University, Hans Hornung, Patric Hung, Scott Jackson, Amy K. W. Lam, Daniel Lieberman and Florian Pintgen at Caltech, Marco Arienti at UTRC, Joanna M. Austin at UIUC, Tong Wa Chao at Intel, Marcia Cooper at SNL, Eric Wintenberger at GE, John H. S. Lee and Hoi D. Ng at McGill, Pierre J. Van Tiggelen at Louvain,

Elaine S. Oran and Vadim Gamezo at Naval. Suzy Dake's secretarial assistance in studying at Caltech was appreciated.

I am grateful for the service of my thesis committee members Takahiko Tanahashi, Masahiko Mizomoto, and Shinnosuke Obi at Keio University.

Finally, and most importantly, I am eternally grateful to my wife Koko, parents Tomiaki & Hiroko, and sister Chizuko for moral support and patience.

This research was supported by the research fellowships of the Japan Society for the Promotion of Science for Young Scientists, Hattori-houkoukai foundation, and Keio Leading-edge Laboratory of Science & Technology.

Abstract

This thesis examines two dynamics of cellular structures in detonation phenomena: transverse wave properties and the mechanism of soot track formation. The first part of the thesis is concerned with one- and two-dimensional gaseous hydrogen detonations. The second part of the thesis is concerned with the soot track formation that has been unsolved for more than 40 years. Chapter 1 gives the background and the motivation of the thesis. Chapter 2 reveals the characteristics of longitudinal oscillations due to the interaction between the shock front and the reaction front. In Chapter 2, one- and two-dimensional detonation simulations are performed with a simplified reaction mechanism to compare their oscillations. Chapter 3 treats two-dimensional detonations with a detailed reaction mechanism to clarify the characteristics of transverse oscillations that play a prominent role in detonation propagation. According to Chapters 2 and 3, transverse wave intensity is newly proposed as a guide to understand the mixture properties. It gives us the insight into control of detonation in safety engineering and application in aerospace engineering. Chapter 4 proposes the mechanism of the soot track formation that has been widely applied to observe detonations. Mach reflection experiments record soot tracks. Features of the soot tracks in experiments are explained in terms of shear stress variations in direction and magnitude created by a boundary layer adjacent to a soot foil. Numerical soot foils are redistributed by shear stress histories of three-dimensional air flow. The agreement of experimental and numerical soot foils leads us to suggest that the mechanism is also applied to detonation soot tracks. Chapter 5 gives the conclusions of the thesis.

Contents

List of Figures

List of Tables

Nomenclature

SI Units

Roman characters

a	detonation cell length	m
A_l	pre-exponential factor in reaction rate of elementary reaction l	(various)
b	detonation cell width	m
c	frozen speed of sound	m/s
C_f	friction coefficient	
C_p	specific heat at constant pressure	J/kg/K
d	thickness of moving layers	m
D	detonation wave speed	m/s
e	specific internal energy	J/m^3
E	internal energy	J/m^3
E_1, E_2	activation energy for two-step reaction mechanism [see eq.(2.1, 2.2)]	J/kg
E_c	critical energy [see page 35]	J/m^2
E_{init}	initial energy release in blast initiation	J/m^2
E_l	activation energy of elementary reaction l	J/kg
f	degree of overdrive (= D^2/D_{CJ}^2)	
f_x, f_z	tractional forces of soot particles in x and z directions	N
F, G	inviscid flux vectors in x and y directions	(various)
h	specific enthalpy	J/kg

h°	standard heat of formation per unit mass at temperature T°	J/kg
h	soot height	m
I_{sp}	specific impulse	s
I_{tw}	transverse wave intensity	
k_1	rate constant for two-step reaction mechanism [see eq.(2.1)]	$m^3/kg/s$
k_2	rate constant for two-step reaction mechanism [see eq.(2.2)]	$m^4/N^2/s$
l_i	initiation blast length	m
l_x	distance from shock wave along x-axis	m
$L_{1/2}$	half reaction length	m
L_{ind}	induction length	m
m_p	mass of soot particle	kg
M_S	shock Mach number	
n	mode number (number of transverse waves across a channel)	
n_l	constant of elementary reaction l [see Table A.1]	
P	pressure	Pa
P_{max}	maximum pressure	Pa
Pr	Prandtl number	
ΔP	amplitude of oscillation	Pa
Q	exothermicity	J/kg
r_p	soot particle radius	m
R	gas constant	J/kg/K
Re	Reynolds number	1/m
R_u	universal gas constant (R_u = 8314.4)	J/kg/K
S	chemical source vector	(various)

S	transverse wave strength	
t	time	s
T	temperature	K
u	flow or particle velocity in x direction	m/s
u_p	piston speed	m/s
U	velocity of shock front; external flow velocity	m/s
$\mathbf{U}$	conservative solution vector	(various)
v	flow velocity in y direction	m/s
V	volume	m^3
w	flow velocity in z direction	m/s
w_i	initiation blast width	m
W	channel width; external flow velocity	m; m/s
W_i	molar mass of species i	kg/mol
W_{max}	maximum channel width where a single transverse wave appears across a channel	m
x	Cartesian coordinate	m
y	Cartesian coordinate	m
z	Cartesian coordinate	m

Greek characters

α	reaction progress variables [see page eq. (2.1)]
β	reaction progress variables [see page eq. (2.2)]
γ	ratio of mixture specific heats
$\delta_{b.l.}$	vorticity boundary layer thickness
η	transformed coordinate normal to the body; boundary layer variable

ϵ	ratio of velocities external and internal boundary layer	
θ_w	apex angle of wedges	$^\circ$
χ	trajectory angles of soot track, triple points	$^\circ$
μ	coefficient of (shear) viscosity	Pa s
ν	kinematic viscosity	m^2/s
ξ	transformed coordinate along the body	
ρ	density	kg/m^3
ρ_i	density of species *i*	kg/m^3
τ	period of oscillation	s
τ_{ind}	induction time	N/m^2
τ_{yx}, τ_{yz}	shear stress in *x* or *z* direction	N/m^2
ω	reaction rate [see page eq. (2.1, 2.2)]	kg/m^3s

Acronums

1-D	one-dimensional
2-D	two-dimensional
3-D	three-dimensional
AMR	adaptive mesh refinement
CFD	computational fluid dynamics
CFL	Courant-Friedrichs-Lewy
CJ	Chapman-Jouguet
CPU	central processing unit
GALCIT	Graduate Aeronautical Laboratories, California Institute of Technology
MF	Mach funnel

PDE pulse detonation engine

PDRE pulse detonation rocket engine

ZND Zel’dovich-von Neumann-Döering

Operators

Δ difference

$[\cdot]$ molar concentration

Subscripts

0 initial condition

1 post-shock condition (incident shock)

1/2 half-reaction state

3 post-shock condition (reflected shock)

20 results with 20 grid points/$L_{1/2}$

40 results with 40 grid points/$L_{1/2}$

Ave average

c critical

CJ Chapman-Jouguet

D driven section [see p.82]

e external

M Mach stem

i species index

ind induction state

init initial blast condition

I incident shock

l	index of reaction progress variable
max	maximum
min	minimum
p	piston; particle
s	shock; soot
ss	post-shock state
T	transverse wave; test section [see p.82]
$triple$	triple point
w	wall

Superscripts

n	time-step counter
$\circ$	standard state

Accents

$\bar{}$	average
$\hat{}$	Roe-average
$\tilde{}$	non-dimensional quantity

Chapter 1

Introduction

Detonations are processes where a shock-induced combustion wave is propagating through a reactive mixture or exothermic compound. Since a shock wave is always observed to precede a reaction zone in a detonation, propagation velocity is always supersonic relative to the upstream speed of sound. The very rapid energy conversion in explosives is the property that makes them useful. Detonation is finding wide application today in various industries: aerospace propulsion, gas-turbine engines, explosive welding, dismantling of decrepit structures, and so on. Although a detonation can produce high-efficiency combustion, it is hazardous; e.g. a hydrogen detonation event was reported in the accident at Hamaoka nuclear power plant in 2001. In the present thesis, only gas-phase detonations will be studied while phenomena of gaseous detonations are known to be similar for condensed systems such as solids and liquids.

1.1 Historical Background in Detonation Research

In 1899, Chapman stated the 1-D flow requirements and compared the minimum theoretical velocity against experimental gaseous detonations. In 1905, Jouguet independently restated Chapman's theory that the tangency point of the Rayleigh line and Hugoniot curve should represent the proper end state of detonations. Hence, a detonation velocity can be calculated from thermodynamic considerations, now well-known to the upper Chapman-Jouguet (CJ) point in the *P*-*V* plane. The CJ criterion agrees with the experimentally measured propagation veloci-

ties within a few percent when the criterion is applied to detonations that are well removed from detonable-limit conditions.

The modern era of detonation research was marked in the years 1940-1945 when Zel'dovich, von Neumann, and Döring each independently formulated essentially the same 1-D model for the internal structure of detonation waves. The equations, relating heat addition to the flow properties, were first applied to the discussion of 1-D (laminar) detonation structure. In their simplest form, their model (the ZND model) considers a steady detonation (independent of time) to consist of the non-reactive shock discontinuity followed by a region of heat addition which continues until the flow becomes sonic (thermal choking) for a CJ detonation.

The stability of the CJ steady solution is lacking in justification even though it predicts correct velocities. In general, the steady solution is hydrodynamically unstable to perturbations, and an alternate 1-D solution is found to be time-dependent longitudinal oscillations of the shock wave reaction zone interaction by nonsteady numerical simulations (Fickett & Davis, 1979). Moreover, the flow near the shock front is known to be far from the 1-D flow in any self-sustaining detonation. The first evidence of the frontal non-steadiness and three-dimensionality was obtained in 1926 by Campbell and Woodhead. They observed a spinning detonation near the detonation limit in circular tubes. At the time of its discovery, spinning detonation was thought to be a phenomenon peculiar to limit mixtures. The true 3-D structure of all self-sustaining detonations was not suspected until the late 1950's.

1.2 Cellular Structures of Detonations

Many of the frontal features of 3-D detonation structures have been revealed by experimental records, e.g., smoked foils; streak photography; stroboscopic laser shadow, schlieren, or interferometric pictures; and pressure traces. They show that all self-sustaining detonation waves

exhibit significant 3-D structures in the region which extends from the leading shock front through the reaction zone of the detonation due to the presence of transverse waves moving up and down between walls.

The frontal structure is characterized by a non-planar leading shock wave and transverse waves; at every instant, it consists of many curved shock sections which are convex toward the incoming flow. A schematic of an idealized structure of a 2-D detonation (Toong, 1983) is shown in Fig. 1.1. The triple-shock interactions (i.e., the Mach configurations) generally consist of three shocks: M, Mach stem; I, Incident shock; and R, Transverse waves (Reflected shock). The intersection of three shocks is called "triple point," and its trajectory T in Fig. 1.1 propagates up and down and forms the cellular structure. A family of propagating transverse waves exhibit a "preferred" spacing which is primarily related to the "thickness" of the reaction zone length (Fickett & Davis, 1979; Toong, 1983). The "preferred" spacing is characterized by triple-point trajectories and is often called "cell width" which is measured by soot foil experiments. Recent experiments by Hanana *et al*. (2001) revealed that most 3-D frontal structures can be explained with the frontal leading shocks and two orthogonal families of transverse waves normal to the front; hence, there is a family of transverse waves propagating into the depth direction in Fig. 1.1.

Cellular structure is commonly used to evaluate detonation propagation. Lee (1984) reported that when a detonation propagates through a rectangular tube whose width is larger than the critical tube width W_c (= 10b; b, cell width), it will succeed in diffracting and propagating through the detonable mixture. The physical mechanism for determing the relationship between the cell number and the tube width in detonation diffraction has not been clearly understood. Although Arienti (2002) reported that the type of detonation diffraction depends on the competition between the energy release rate and the expansion rate behind the diffracting front, the empirical ideas of Lee (1984) are recognized as a useful guide to evaluate the critical

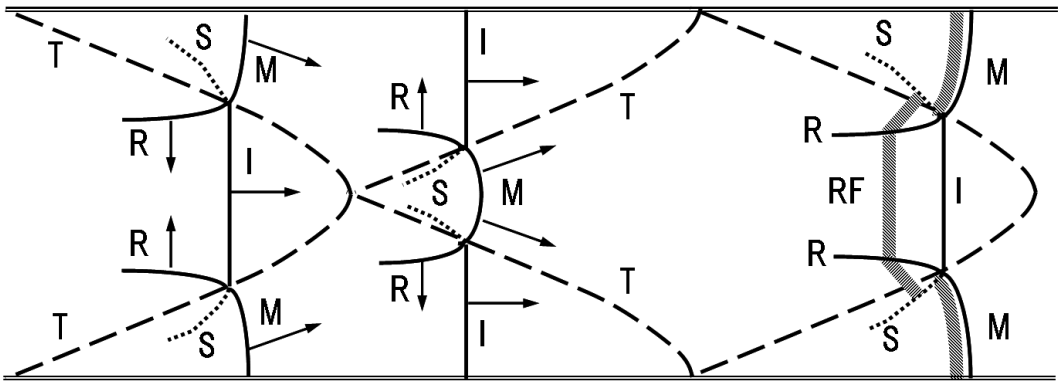

Figure 1.1: Schematic diagram of instantaneous shock configurations and reaction fronts. M: Mach stem; I: Incident shock; R: Transverse wave (Reflected shock); S: Slip line; RF: Reaction Front; T: Triple point track.

conditions. Successful propagation in detonation diffraction is important for the application of PDEs because a detonation is often initiated with the detonation tube that is smaller than the main combustion chamber. When a detonation propagates through the orifice whose rectangular bore width is smaller than W_c, the detonation will fail. It is beneficial for safety reasons to prevent detonation from propagating in an industrial power plant. Therefore, detonation cell width in various mixtures has been extensively examined by experimental, analytical, and numerical approaches.

Assuming that the flow is essentially 1-D, the length of the induction zone or recombination zone between the leading shock and some location in the reaction zone can be computed from the ZND model with an appropriate chemical reaction mechanism. However, exact theory for predicting cell sizes has been proposed so far. Several empirical correlations between the parameters have been developed, along with some phenomenological and approximate theoretical models. Discussions of cell size models and correlations with reaction length are presented by Barthel (1974), Ficket & Davis (1979), Westbrook (1982), and Shepherd (1986). Shepherd (1986) examined the relationship between reaction zone length and

measured cell size as single-parameter correlations, and reported that cell sizes predicted from single-parameter correlations are accurate only to within ±200%, and even though an improved correlation using existing data can predict within ±50%. In the work of Gavrikov *et al.* (2000), the ratio of the detonation cell width to the characteristic reaction zone width is considered to be a function of two stability parameters (dimensionless effective activation energy and a parameter describing the relation between chemical energy and initial thermal energy of the combustible mixture). The mean deviation of calculated values from the experimental data was about 50%. In the prediction of detonation cell widths, the semi-empirical correlation is applied to the latter stability parameter. From a different perspective, Lee (1977) proposed the width of a detonation cell, assuming the propagation to be effected through a series of periodic reinitiations due to the energy derived from the localized chemical explosions (detonation kernel size). Predicted cell size indicates the accuracy within about 200%.

Strehlow (1968) proposed the acoustic coupling theory to predict the cell width based on experimental observation. In his theory, the frontal transverse waves are acoustic waves extending into the hot gas column far from the front in a tube. The present study will expand his theory into quantitative investigations of transverse structures as nonlinear and finite amplitude phenomena. Even though recent computational developments make it possible to simulate very complex problems, it is still difficult to simulate detonation phenomena with sufficient numerical accuracy. One way to reduce the complexity is to use simplified reaction mechanisms, and another way is performing detonation simulations in a narrow channel. Kailasanath *et al.* (1985) stated that the channel width has an influence on the cellular structures. Most of the multi-dimensional simulations are performed within a narrow channel for the restriction of computational resources. This thesis treats the channel width as a parameter, and enables us to obtain results for larger channels than previous studies.

1.3 Soot Track Records in Detonations

When a detonation propagates in a soot-coated tube, diamond-shaped soot tracks are recorded by scrubbing off more soot in some spots than in others (Strehlow, 1968; Fickett & Davis, 1979). These are known as detonation cellular structures. Figure 1.2 shows a typical cellular structure with regular cells obtained in a gaseous detonation. For over 40 years, this soot track method has been widely applied as an indication of detonation propagation (Edwards *et al*., 1979; Knystautas *et al*., 1982) and a semi-quantitative tool for measuring the cell size (Strehlow *et al*., 1969; Strehlow & Engel, 1969; Bull *et al*., 1982; Kumar, 1990; Stamps & Tieszen, 1991; Austin & Shepherd, 2003) . It is readily apparent and demonstrated experimentally that the soot tracks are associated with the transverse waves and triple points that move along the main shock front (Hanana *et al*. 2001). Numerical simulations of detonation have used reaction intensity (Lefebvre & Oran 1995; Oran *et al*. 1998) and peak pressure (Gamezo *et al*. 1999) as soot track surrogates, and contours of these quantities produce reasonable facsimiles of soot tracks. However, the precise physical mechanism that creates the soot tracks has never been clearly demonstrated and it is not known what features of the triple-point structure represent the soot tracks.

The Mach reflection effect was discovered by Antolik in 1875, more than one hundred years ago. Shock wave reflection and interaction experiments conducted were originally interpreted by Mach & Wosyka with soot covered glass plates in 1875. The Mach reflection was started by a V-shaped exploding gliding spark, and formed a funnel-shaped V-formation on the soot (as shown in Fig. 1.3). Mach speculated that the Mach stem was of greater strength than the incident shock by the fact that the soot inside the Mach stem funnel was compressed more than the soot outside and was blown off the plate. Combining this soot method with the schlieren technique, Krehl & Geest (1991) observed shock interactions and soot removal phe-

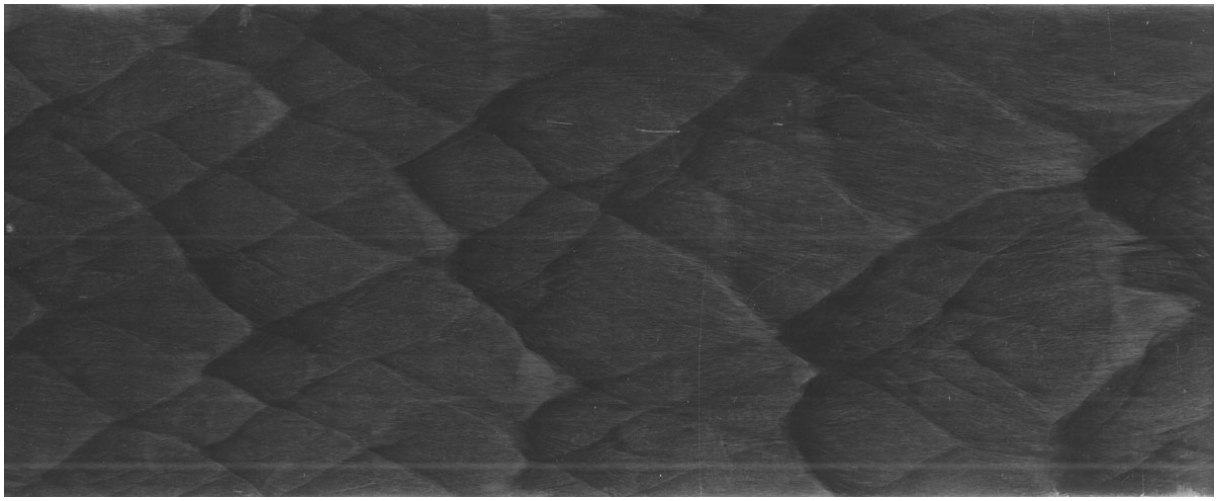

Figure 1.2: Experimental soot foil of a detonation in 45% N_2 diluted stoichiometric CH_4+O_2, initially at 0.01MPa, in GALCIT detonation tube. The detonation-propagation direction is left to right.

nomena simultaneously. They proposed that soot tracks were caused by scrubbing the soot off by vortices generated around slip lines rather than pressure gradients as in Mach's explanation. On the other hand, Terao & Azumatei (1989) suggested that soot tracks in detonation waves are formed by combustion of the soot in hot oxidizing atmospheres behind the shock waves.

Recently, Pintgen & Shepherd (2003) found, in a preliminary experiment, that the triple-point trajectories derived from Planar Laser Induced Fluorescence (PLIF) of the OH radical near the soot foil are close to, but not exactly coinciding with the soot tracks. Since soot tracks is thought to be closely associated with the triple points, the formation mechanisms must be clarified in to have a clear meaning for cell width. Furthermore, the removal of fine soot particles from surfaces is applied to surface cleaning for industry and the conservation of works of art and historic buildings. In the semiconductor industry, surface cleaning methods that do not use cleaning liquids must be exploited for silicon wafers. Cleaning liquids, such as chlorofluorocarbon, are prohibited because of environmental destruction. To establish a cleaning method using shock waves (Smedley *et al.*, 1999) or air jets (Otani *et al.*, 1993), it is useful to

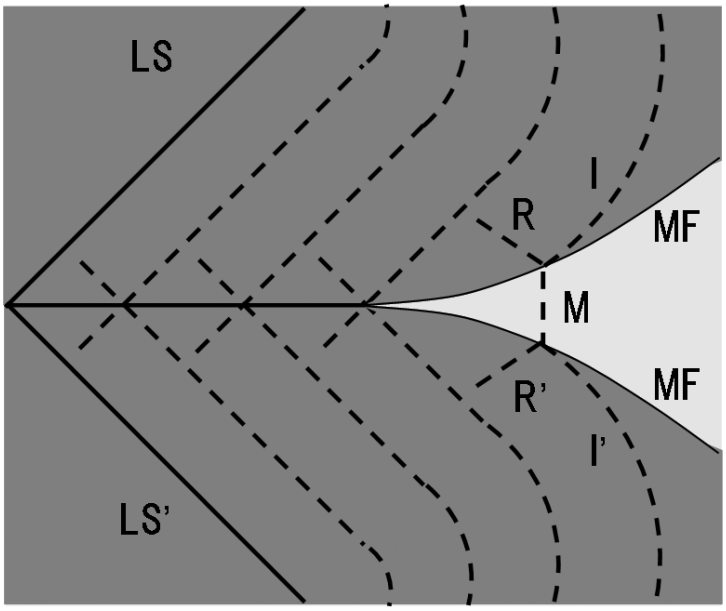

Figure 1.3: Schematic diagram of Mach's historical experiment of soot track formation with soot on a glass plate. (M: Mach stem; I: incident shock; R: reflected shock; MF: Mach funnel; LS: leading shock wave.)

investigate the removal process of fine particles from a surface.

1.4 Present Research

The present research treats two major problems relating to cellular structures of propagating detonations: transverse wave properties and soot track formation. The goals are to evaluate transverse waves for predicting cell widths and to clarify the mechanism of soot track formation.

Chapter 2 examines the problem of the relationship between 1-D longitudinal oscillations and 2-D transverse oscillations. 1-D and 2-D numerical simulations are performed with a simplified chemical reaction model. The discussion starts from comparison between 1-D oscillations and unsteady oscillations in shock-induced combustion around a blunt body projectile propagating at hypersonic velocity through premixed gases. Based on the oscillation

characteristics of 1-D overdriven detonations, centerline profiles of frontal pressures in 2-D CJ detonations are investigated. Very few attempts have been made at such a detailed comparison between 1-D and 2-D simulations. Oran *et al*. (1998) showed by 2-D simulations that a new triple point appears on the Mach stem due to the longitudinal instability. It will be examined whether 1-D instability produces the new triple point in 2-D detonations and what kinds of influences appear in 2-D oscillations by changing channel width, compared with 1-D oscillations.

In Chapter 3, numerical simulations of cellular detonations are performed with a detailed chemical reaction mechanism. The local chemical composition of the flow can be detected and, thus, variation of frozen speed of sound and specific heats can be evaluated more correctly than the results with the simplified reaction mechanism in §2.1. These effects are relevant to discussions of the detonability limit and the acoustic coupling. Finally, transverse wave intensity is proposed as a figure of merit for industrial applications.

As for soot track generation, Chapter 4 presents experiments and numerical simulations. Soot track generation will be examined in air with non-reacting Mach reflection around a wedge and in detonations. Experimental results with air will be compared with 3-D viscous simulations. A 3-D boundary layer induced by the shock front will be discussed with theoretical analysis. Fletcher (1976) examined the interaction between dusty layers of particles and passing shock waves related to coal mine explosions, and revealed that dust was raised as a result of the rapid flow following behind the shock wave, rather than as that of a pressure wave passing through the dust layer. Although the dust rising may not be identical phenomena with the soot track formation, the rapid flow would dominate over the formation mechanism. Hence, focusing on the role of shear stress in transporting soot along the surface, it is investigated whether soot tracks depend on variations in the direction and magnitude of the shear stress created by the boundary layer adjacent to a soot foil. Numerical simulations of soot are performed to verify the soot redistribution process using shear stress in 3-D simulations as tractive forces.

Chapter 2

One- and Two-Dimensional Detonations with Two-Step Reaction Mechanism

2.1 Instability of Oscillations of Shock Wave-Reaction Front Interactions

Ballistic range experiments in 1960s and 1970s revealed that the shock-induced combustion around the spherical projectile flying into the combustible gases has unsteady and periodic shock-reaction system (McVey & Toong, 1971; Alpert & Toong, 1972; Lehr, 1972; Kasahara *et al*., 1997). Those experiments show intrinsic instabilities of mixture. Two oscillation modes are observed in shock wave-reaction front interactions: low amplitude and high frequency oscillations "regular regime" (Fig. 2.1) and high amplitude and low frequency ones "large-disturbance regime" (Fig. 2.2). Figure 2.1(a) is a experimental shadow graph of "regular regime," taken by Lehr (1972), and Fig. 2.2(a) is a schlieren picture of "large disturbance regime." Toong and co-authors first proposed periodic instability mechanisms based on experimental observation and 1-D wave interaction theory. Recently, computational fluid dynamics has been utilized to simulate the flow features of ballistic range experiments, and the mechanisms of the regular regime and the large-disturbance regime have been clarified by the CFD researches as shown in Fig. 2.1(b) and Fig. 2.2(b) (Matsuo & Fujiwawa, 1993; Susman, 1994; Matsuo *et al*., 1995a; Matsuo & Fujii, 1995b, 1996, 1998); Kamiyama & Matsuo, 2000). Matsuo & Fujii (1995b, 1998) have indicated that not the projectile velocity but the intensity of the concentration of the heat release is the essential factor to determine the unsteadiness, and they newly proposed the

wave interaction model for the large-disturbance regime.

One-dimensional piston supported flows have been also investigated employing numerous theoretical and computational analyses to understand the detonation phenomena (Erpenbeck, 1964; Fickett *et al*., 1972; Bourlioux *et al*., 1991; Sussman, 1994; He & Lee, 1995; Clavin & He, 1996; Matsuo & Fujii, 1997; Sharpe & Falle, 2000a; Sánchez *et al*., 2001; Sharpe, 2001a; Ng & Lee, 2003; Daimon & Matsuo, 2003). Most of those works wrestle with 1-D instability of detonation fronts and the direct initiation of detonations, while some works (Sussman, 1994; Matsuo & Fujii, 1997) focus on relation between 1-D instability and unsteadiness of the shock-induced combustion observed in ballistic range experiments. Fickett *et al*. (1972) found the same two oscillation modes in 1-D piston driven flows with a one-step irreversible reaction model as ballistic range experiments. In the work of Sussman (1994), the hydrogen-oxygen full chemistry was used for simulations, and the numerical results showed that the two modes appeared by changing a degree of overdrive. Matsuo & Fujii (1997) indicated that the oscillation type did not depend on the intensity of the concentration of the heat release in contrast to the unsteadiness of the shock-induced combustion. Longitudinal oscillations of 1-D overdriven detonations are not restricted to gaseous detonations and are reported on detonations in nitromethane and liquid TNT by Mader (1998).

In almost all the previous studies of the 1-D piston supported detonation, solutions of steady detonations were used as initial conditions, and various waves reflecting on the piston surface were numerically removed by non-reflection boundaries. The reflected waves, however, play important roles in the periodic mechanism in ballistic range experiments. Although Sharpe (2001) stated importance of piston initiation process of detonations and performed 1-D simulations with a single irreversible reaction with Arrhenius kinetics, the regular regime which appears in the shock-induced combustion can not be seen with the one-step mechanism (Daimon & Matsuo, 2003). The present study is carried out to clarify oscillation characteristics

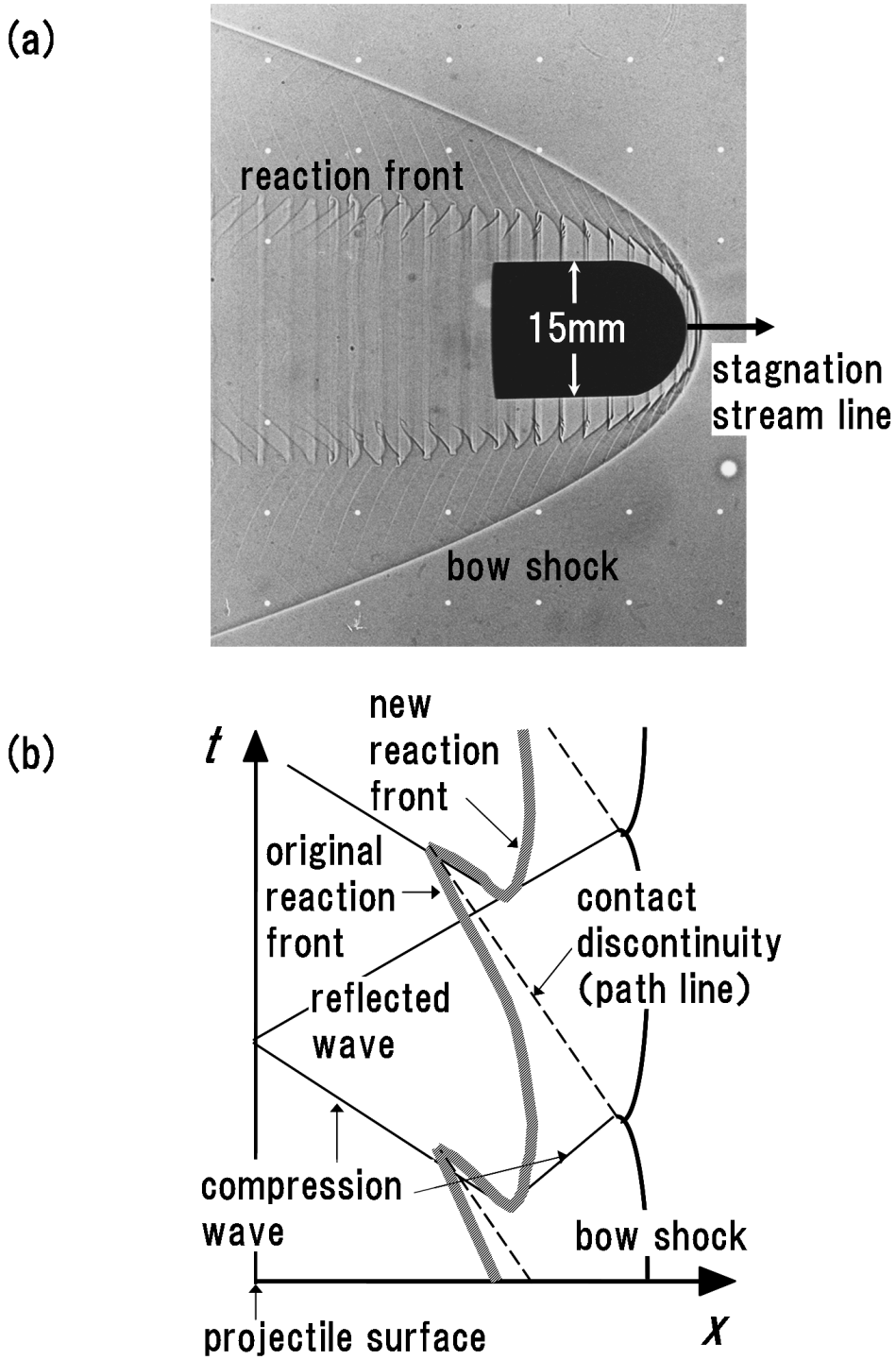

Figure 2.1: High frequency oscillations in shock-induced combustion around blunt body projectile. (a) Shadowgraph of the regular regime in stoichiometric H_2-Air, initially at 42.7kPa (courtesy of Lehr). Projectile propagates at 2029 m/s. (b) Schematic diagram of shock-reaction oscillation in regular regime on the stagnation line.

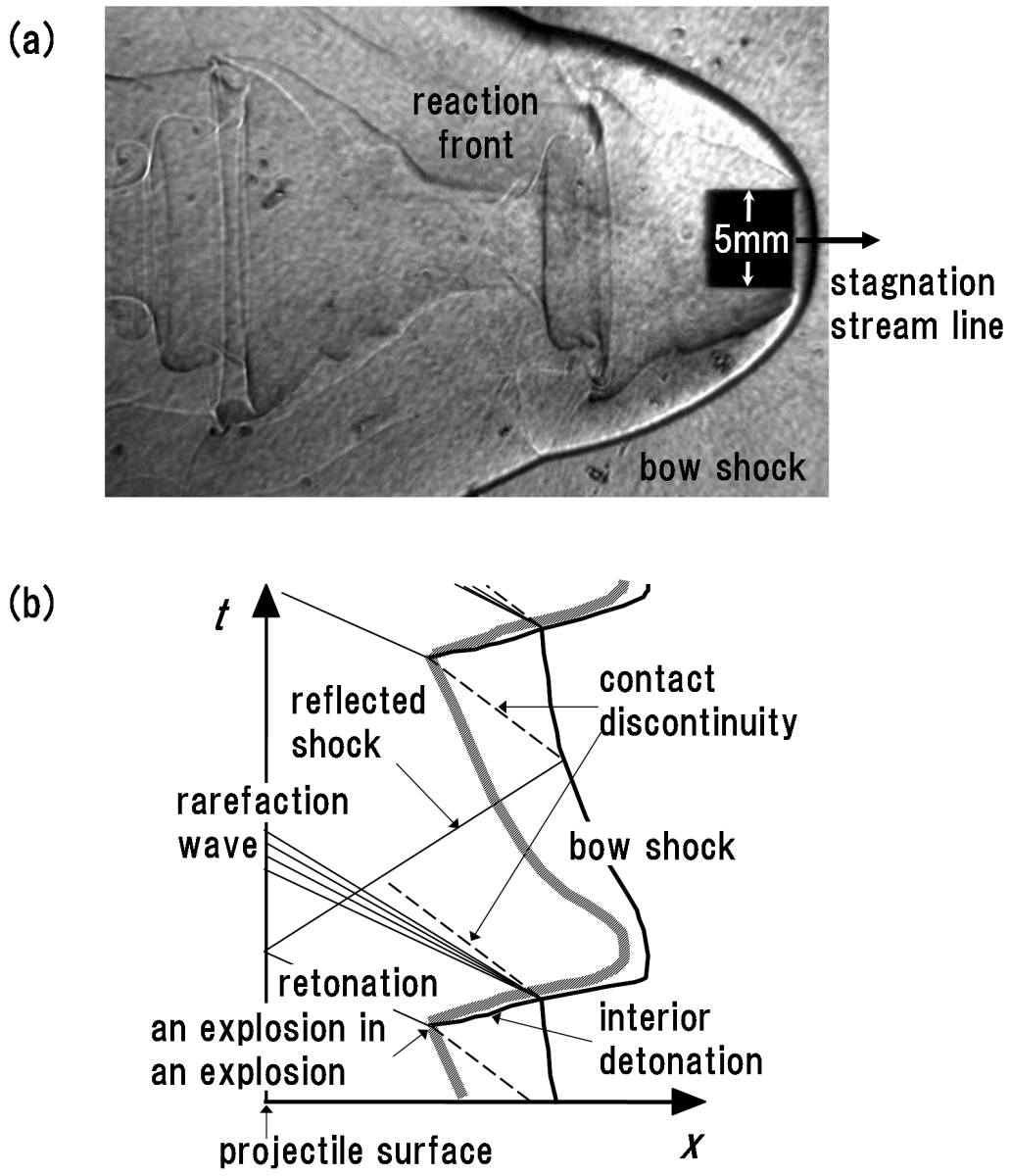

Figure 2.2: Low frequency oscillations in shock-induced combustion around blunt body projectile. (a) Schlieren photograph of the large disturbance regime in stoichiometric H_2-Air, initially at 60.8kPa. Projectile propagates at 1979 m/s. (b) Schematic diagram of shock-reaction oscillation in large disturbance regime on stagnation line.

initiated by a steady solution, and by shock compression with a piston, taking into account of reflected waves at the piston surface. Through those simulations, relations between 1-D piston driven detonations and the shock-induced combustion are also discussed. Under the same conditions as 1-D simulations, 2-D simulations are performed and compared with 1-D longitudinal oscillations. Very few attempts have been made at the comparison of 1-D detonations with 2-D detonations. Bourlioux & Majada (1995) stated both 1-D and 2-D detonations in the same paper, but they compared 2-D detonations with a theory of the frontal instability rather than 1-D oscillations. Williams *et al*. (1996) also compared 1-D detonations with 2-D detonations; however, they discussed about the initiation process. In §2.4.4, oscillation characteristics on the centerline of cellular structures are examined to discuss the oscillation characteristics and the relation between 1-D and 2-D detonations.

2.2 Numerical Setup

2.2.1 Reaction mechanism

One- and two-dimensional simulations are conducted using a two-step chemical reaction mechanism proposed by Korobeinikov *et al*. (1972). An idealized structure of a detonation wave is explained with the ZND structure in which a chemical reaction is initiated and heat is released into the stream behind the shock-wave front after the end of the induction period. Koroveinikov's two-step chemistry well reproduces the detonation structure with reaction progress variables α and β corresponding to an induction process and an exthothermic process, respectively. The equations that describe the evolution of the chemical reactions are taken in the Arrenius form:

$$\omega_\alpha \equiv \frac{d\alpha}{dt} = -\frac{1}{\tau_{ind}} = -k_1 \rho \exp\left(-\frac{E_1}{RT}\right) \tag{2.1}$$

Table 2.1: Two-step reaction parameters of Korobeinikov (1972).

Q (exothermicity)	2.330 MJ/kg
R (gas constant)	397.6 J/kg/K
E_1/R (activation energy)	9850 K
E_2/R (activation energy)	2000 K
k_1 (rate constant)	3.000×10^{8} m^3/kg/s
k_2 (rate constant)	4.185×10^{-5} m^4/N^2/s
γ (specific heat ratio)	1.4

$$\omega_\beta \equiv \frac{d\beta}{dt} = \begin{cases} 0 & \alpha > 0 \\ -k_2 P^2 \left\{\beta^2 \exp\left(-\frac{E_2}{RT}\right) - (1-\beta)^2 \exp\left(-\frac{E_2+Q}{RT}\right)\right\} & \alpha \le 0 \end{cases} \tag{2.2}$$

where $\omega, \tau_{ind}, P, R, T, Q$ are the reaction rate, the induction time, pressure, gas constant, temperature, and exothermicity, respectively. Reaction-progress variables α, β; rate constants k_1, k_2; activation energies E_1, E_2 are parameters for the induction process and the exthothermic process, respectively. It is assumed that $\beta = 1$ prior to the start of reaction while $\alpha = 1$ on the shock-wave front (eq. (2.2)). Vanishing of α means termination of the induction period and start of the heat-releasing reaction. No heat is released in reaction (eq. (2.1)).

The rate constants in eqs. (2.1, 2.2) are so selected to correspond to a diluted stoichiometric hydrogen-oxygen mixture: $2H_2+O_2+3.76N_2$, and are listed in Table 2.1. Those parameters are determined by referring to Korobeinikov *et al*. (1972) and Taki & Fujiwara (1978). In previous works for detonation simulations, simplified reaction mechanisms were often adopted to save CPU times and computational resources such as memories and devices for storing data. Korobeinikov's two-step mechanism is one of the most famous mechanisms and is often utilized to perform detonation simulations.

2.2.2 Governing equations

The physical model of detonation simulations is presented in this section. Detonation simulations are performed with the reactive Euler equations governed for compressible reacting flow, ignoring viscosity, heat transfer, diffusion and body forces. The combustible gas mixture is assumed to be perfect gas. Hence, the governed equations for 2-D detonations with Korobeinikov's chemical reaction become followings:

$$\frac{\partial \mathbf{U}}{\partial t} + \frac{\partial \mathbf{F}}{\partial x} + \frac{\partial \mathbf{G}}{\partial y} = \mathbf{S} \tag{2.3}$$

where **U**, **F**, **G**, and **S** are the conservative solution vector, the inviscid flux vectors in the *x* and *y* directions, and the chemical source vectors, respectively.

$$\mathbf{U} = \begin{bmatrix} \rho \\ \rho u \\ \rho v \\ e \\ \rho\beta \\ \rho\alpha \end{bmatrix}, \quad \mathbf{F} = \begin{bmatrix} \rho u \\ P + \rho u^2 \\ \rho uv \\ (e + P)u \\ \rho\beta u \\ \rho\alpha u \end{bmatrix}, \quad \mathbf{G} = \begin{bmatrix} \rho v \\ \rho uv \\ P + \rho v^2 \\ (e + P)v \\ \rho\beta v \\ \rho\alpha v \end{bmatrix}, \quad \mathbf{S} = \begin{bmatrix} 0 \\ 0 \\ 0 \\ 0 \\ \rho\omega_\beta \\ \rho\omega_\alpha \end{bmatrix} \tag{2.4}$$

$$P = \rho RT \tag{2.5}$$

$$e = \frac{P}{\gamma - 1} + \rho\beta Q + \frac{1}{2}\rho(u^2 + v^2) \tag{2.6}$$

In the case of 1-D simulations, the governing systems of equations are given as followings:

$$\frac{\partial \mathbf{U}}{\partial t} + \frac{\partial \mathbf{F}}{\partial x} = \mathbf{S} \tag{2.7}$$

$$\mathbf{U} = \begin{bmatrix} \rho \\ \rho u \\ e \\ \rho\beta \\ \rho\alpha \end{bmatrix}, \quad \mathbf{F} = \begin{bmatrix} \rho u \\ P + \rho u^2 \\ (e + P)u \\ \rho\beta u \\ \rho\alpha u \end{bmatrix}, \quad \mathbf{S} = \begin{bmatrix} 0 \\ 0 \\ 0 \\ \rho\omega_\beta \\ \rho\omega_\alpha \end{bmatrix}. \tag{2.8}$$

$$e = \frac{P}{\gamma - 1} + \rho\beta Q + \frac{1}{2}\rho u^2 \tag{2.9}$$

Yee's non-MUSCL TVD upwind explicit scheme (1987) is used as a numerical scheme. The detail explanation of point-implicit method for time integration procedure is given in Appendix D.

2.3 One-Dimensional Piston Supported Detonations

2.3.1 Initial conditions

The initial conditions are identical to Lehr's experiment (1972): a stoichiometric gas mixture $2H_2+O_2+3.76N_2$ at initial pressure $P_0 = 42.7$ kPa and initial temperature $T_0 = 293$ K. Two-step reaction parameters in Table 2.1 are adopted for the mixture, and Chapman-Jouguet (C-J) detonation velocity D_{CJ} equals to 1938.3 m/s under the parameter sets. Post-shock conditions, piston speeds, induction lengths, and induction times are presented in Table 2.2, which are calculated from 1-D ZND solutions of steady detonations for a given degree of overdrive f. The degree of overdrive, $f = (D/D_{CJ})^2$, was varied between 1.1 and 2.0 at intervals of 0.1.

As for 1-D simulations, two types of initiation process are attempted: employing steady ZND solutions as initial conditions (SD case); overdriving quiescent combustible gases by a piston (PI case). A coordinate system moves at the same speed as a piston surface, and 32001 points in SD case and 80001 points in PI case are provided in the whole computational

Table 2.2: Post-shock conditions for given degree of overdrives f. D: shock speed; ρ_1: density; P_{ss}: pressure; T_1: temperature; u_1: flow speed; c_1: frozen sound speed; u_p: piston speed; L_{ind}: induction length; τ_{ind}: induction time.

Degree of overdrive f	D (m/s)	ρ_1 (kg/m^3)	P_{ss} (MPa)	T_1 (K)	u_1 (m/s)	c_1 (m/s)	u_p (m/s)	L_{ind} (μm)	τ_{ind} (ns)
1.000	1938	1.805	1.139	1587	393.2	940.0	773.0	359.6	914.5
1.100	2033	1.835	1.254	1719	405.7	978.1	1069	227.1	559.8
1.200	2123	1.861	1.369	1850	417.9	1015	1214	153.6	367.6
1.300	2210	1.883	1.483	1982	429.8	1050	1332	109.7	255.2
1.400	2293	1.902	1.598	2113	441.5	1084	1436	81.88	185.5
1.500	2374	1.919	1.713	2244	452.9	1118	1531	63.37	139.9
1.600	2452	1.934	1.827	2376	464.1	1150	1619	50.54	108.9
1.700	2527	1.948	1.941	2507	475.0	1181	1702	41.34	87.03
1.800	2601	1.961	2.057	2638	485.7	1212	1779	34.54	71.12
1.900	2672	1.972	2.171	2769	496.1	1242	1854	29.40	59.25
2.000	2741	1.982	2.286	2901	506.5	1271	1925	25.41	50.18

domain. One-dimensional steady ZND solutions are calculated by solving the following equation with different degrees of overdrives (piston speed) as rear boundary conditions:

$$\frac{\partial \mathbf{F}}{\partial x} = \mathbf{S}. \tag{2.10}$$

For given degrees of overdrive ($1.1 \leq f \leq 2.0$), the steady solution in Fig. 2.3 is not stable, so an alternate solution that satisfies the same rear boundary condition ($x = 0$) appears in the flow fields. The alternate solution is known to be oscillatory solutions due to the shock wave-reaction front interaction (Fickett & Davis, 1979). Temperature behind the shock front rises by the same amount about 1000 K ($= \Delta T$); hence, energy release behind the front almost the same for different degrees of overdrive. The oscillatory solutions become more sensitive to post-shock conditions, as a degree of overdrive decreases. As shown in Fig. 2.3, post-shock temperature T_1 increases as a function of a degree of overdrive. When post-shock temperature decreases, the induction time increases exponentially (Fig. 2.4). Even though the variation of post-shock conditions is small, the induction time changes exponentially; therefore the flow is more sensitive to the variation of post-shock conditions for a low degree of overdrive.

First, grid convergence studies in SD case are performed with 20, 40, 80, and 160 grid points per induction length L_{ind} for the degree of overdrive $f = (D/D_{CJ})^2 = 2.0$ and 1.2, where D is an overdriven detonation velocity. With adequate grid resolution, oscillation characteristics are investigated for degrees of overdrive between 1.1 and 2.0 at intervals of 0.1 in SD case and a fixed degree of overdrive 1.2 in PI case. The case of $f = 1.0$ is excluded from simulation conditions because the induction time and length are extremely increased and the shock wave-reaction front interaction is not observed in the computational domain. In PI case, a detonation front is initially excited into a highly overdriven condition and is gradually attenuated by rarefaction waves toward an intent degree of overdrive $f = 1.2$. Hence, the unsteady properties of oscillation behaviors are observed in the decay process and are compared

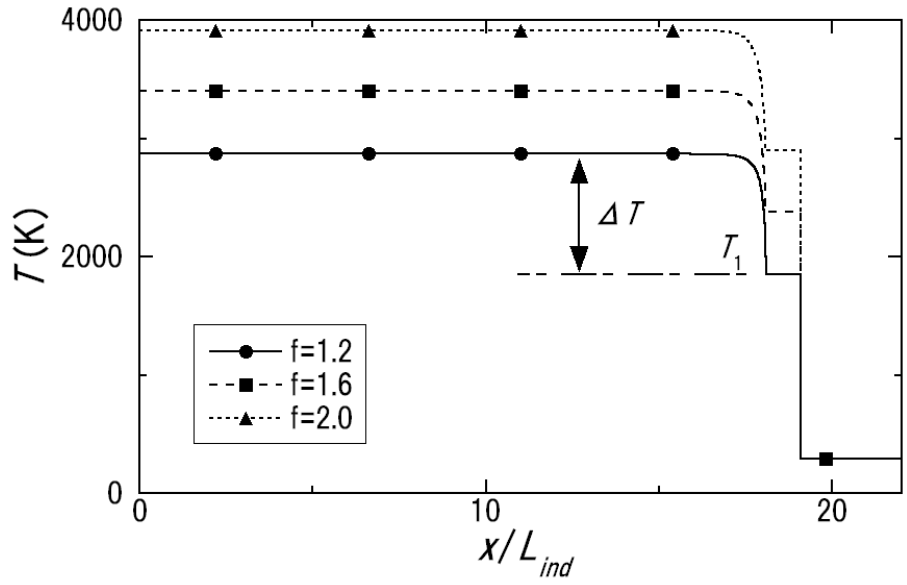

Figure 2.3: Initial temperature profiles for different degrees of overdrive. (T_1, post-shock temperature; ΔT, temperature increase behind shock wave)

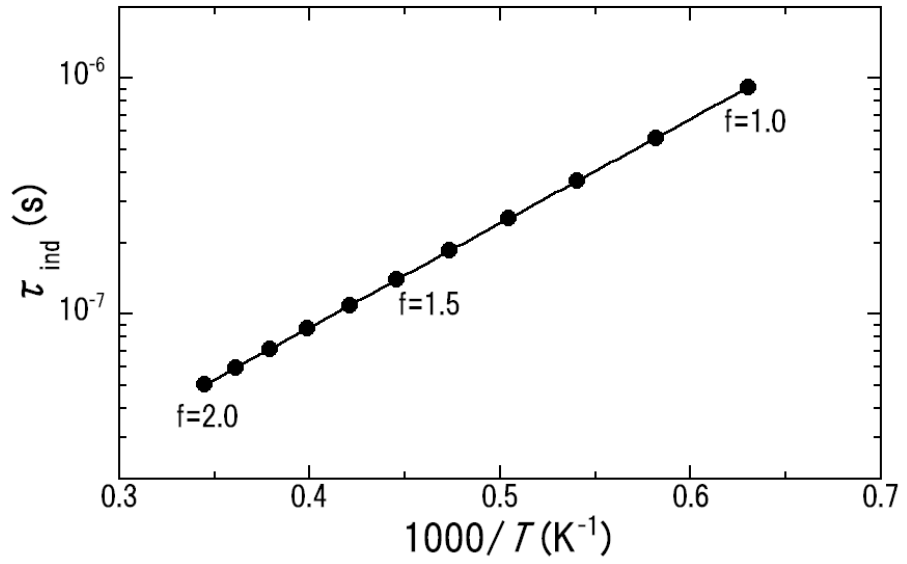

Figure 2.4: Arrhenius plot of induction time τ_{ind} for different degrees of overdrive.

with steady oscillation characteristics in SD cases.

2.3.2 Grid convergence study in one-dimensional detonations

The grid convergence study is performed in SD case on successively decreased grid spacing of 20, 40, 80, and 160 grid points / L_{ind} for a degree of overdrive $f = 2.0$ and 1.2. Especially 64001 grid points are provided for the grid resolution with 160 points / L_{ind}. Figure 2.5 shows shock pressure histories for the same initial conditions of different grid resolution. In those figures, stable low amplitude and high frequency oscillations are observed; the high frequency mode. On the successively finer spacing of 20, 40, 80, and 160 grid points / L_{ind}, final oscillation characteristics are comparatively agree well with each other; however, initial aspects looks different. Steady ZND detonations are immediately perturbed by the numerical truncation error and begin to oscillate. With two finer grids of 80 and 160 grid points / L_{ind}, oscillation gradually develops from less errors than those with grids of 20 and 40 grid points / L_{ind}.

The oscillation period and pressure peak and trough are derived from the shock pressure variations in Fig. 2.5, and are normalized by the characteristic induction period, τ_{ind}, and the post-shock pressure, P_{ss}, in the solution of a steady detonation, respectively. Figure 2.6 summarizes the computed oscillation periods and normalized pressure oscillations. With more than 40 grid points / L_{ind}, those solutions are sufficiently converged into the same oscillations characteristics after initially unstable oscillations; the normalized oscillation period by the induction time $\tau/\tau_{ind} = 1.48$. According to McVey & Toong (1971), the period of high frequency mode is predicted by the sum of the time when the compression wave and the contact discontinuity take to propagate through the induction length behind the leading shock, based on the mechanism in Fig. 2.1(b). The proposed formula is given by

$$\tau = \frac{L_{ind}}{c_1 - u_1} + \frac{L_{ind}}{u_1} = \frac{c_1 L_{ind}}{(c_1 - u_1)u_1} = \frac{\tau_{ind}}{1 - u_1/c_1}, \tag{2.11}$$

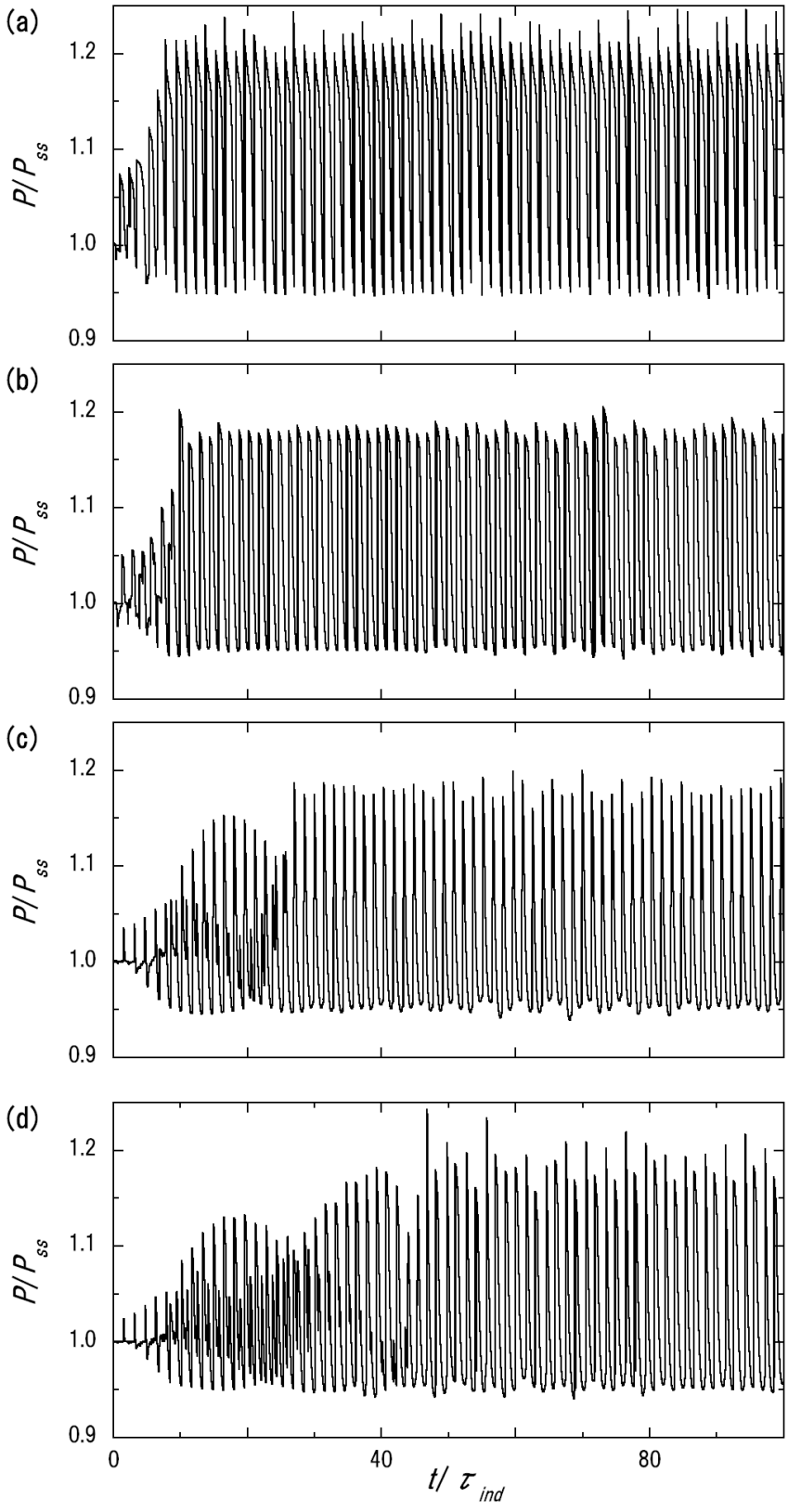

Figure 2.5: Shock pressure histories of one-dimensional piston-supported detonations for SD case with $f = 2.0$. Grid resolution of (a) 20, (b) 40, (c) 80, and (d) 160 points / L_{ind}.

where τ is the period of the high frequency mode. The period derived from eq. (2.11) is about $1.66\tau_{ind}$ and is comparatively close to the simulated result of $1.48\tau_{ind}$; hence, the oscillation observed here is explicable physically rather than numerical oscillations of the scheme. Through the simulations, CFL number is set to 0.5. The extrapolated normalized periods by the induction time and the relative error are derived from simulations at CFLs 0.25, 0.5, and 0.9. The extrapolated period is 1.51, and the relative error is 2.2% at CFL 0.5 (Roache, 1997).

The normalized amplitude (peak-trough variation) by the post-shock pressure $\Delta P/P_{ss} =$ 0.23. The shock pressure presented in Fig. 2.5 is the post-shock pressure, not the maximum pressure. The shock front is always supported by the reaction front, which makes it difficult to distinguish the post-shock pressures from the maximum pressures affected by the reaction front. In this thesis, the post-shock pressure is measured at the point where the pressure becomes larger than initial pressure, $P \geq 1.5P_0$, and the pressure rise between neighboring two grids becomes less than a tenth of initial pressure, $\Delta P = P_j - P_{j-1} \leq 0.1P_0$.

The grid convergence study is also performed on successively decreased grid spacing of 20, 40, 80, and 160 grid points / L_{ind} with $f = 1.2$. For a low degree of overdrive $f = 1.2$, the nonlinear instability is known to be more unstable than that for a high degree of overdrive $f = 2.0$. The entirety of shock pressure histories are presented in Figs. 2.7(a–d). In the histories, shock pressures indicate very unstable behaviors, and the flow is chaotic. The chaotic behaviors of 1-D detonations was widely observed and examined by Clavin & He (1996), Williams *et al*. (1996), Sharpe & Falle (2000), Ng & Lee (2003), and Daimon & Matsuo (2003). It is very difficult to define the convergence of the solution. The oscillation characteristics are determined by the largest oscillations which seem to be dominant in the oscillations.

The computed oscillation period and shock pressures are presented in Fig. 2.8. Period of oscillation becomes almost constant with more than 80 points / L_{ind} in Fig. 2.8(a). Pressure trough (dashed line) in Fig. 2.8(b) is almost constant throughout the simulations while

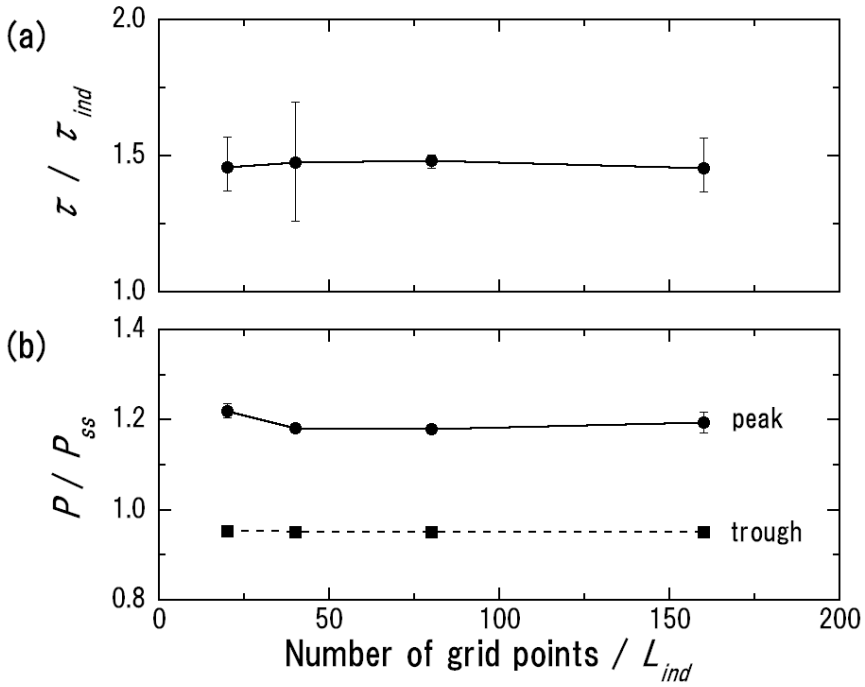

Figure 2.6: One-dimensional piston-supported detonations for SD case with $f = 2.0$. (a) Period of oscillations. (b) Pressure peak (solid line) and trough (dashed line).

pressure peak slightly increases as the number of grid points / L_{ind} is increasing. Oscillation characteristics, however, are so unstable that average pressure peaks have large error bars. The tendency of Fig. 2.7(c) coincide with that of Fig. 2.7(d). It is concluded that the results with 80 points / L_{ind} is almost converging into the same properties of the results with 160 points / L_{ind}. In PI case, the flow transiently becomes very unsteady, and thus the following 1-D results are simulated with the grid with 80 points per L_{ind} in SD case and 160 points per L_{ind} in PI case.

2.3.3 Oscillation characteristics of detonations developed from steady detonation (SD)

Figure 2.9 shows the histories of the shock pressures for $f = 2.0, 1.4$, and 1.2. Figure 2.9(a) shows the typical oscillation characteristics of the high frequency mode. In the high frequency

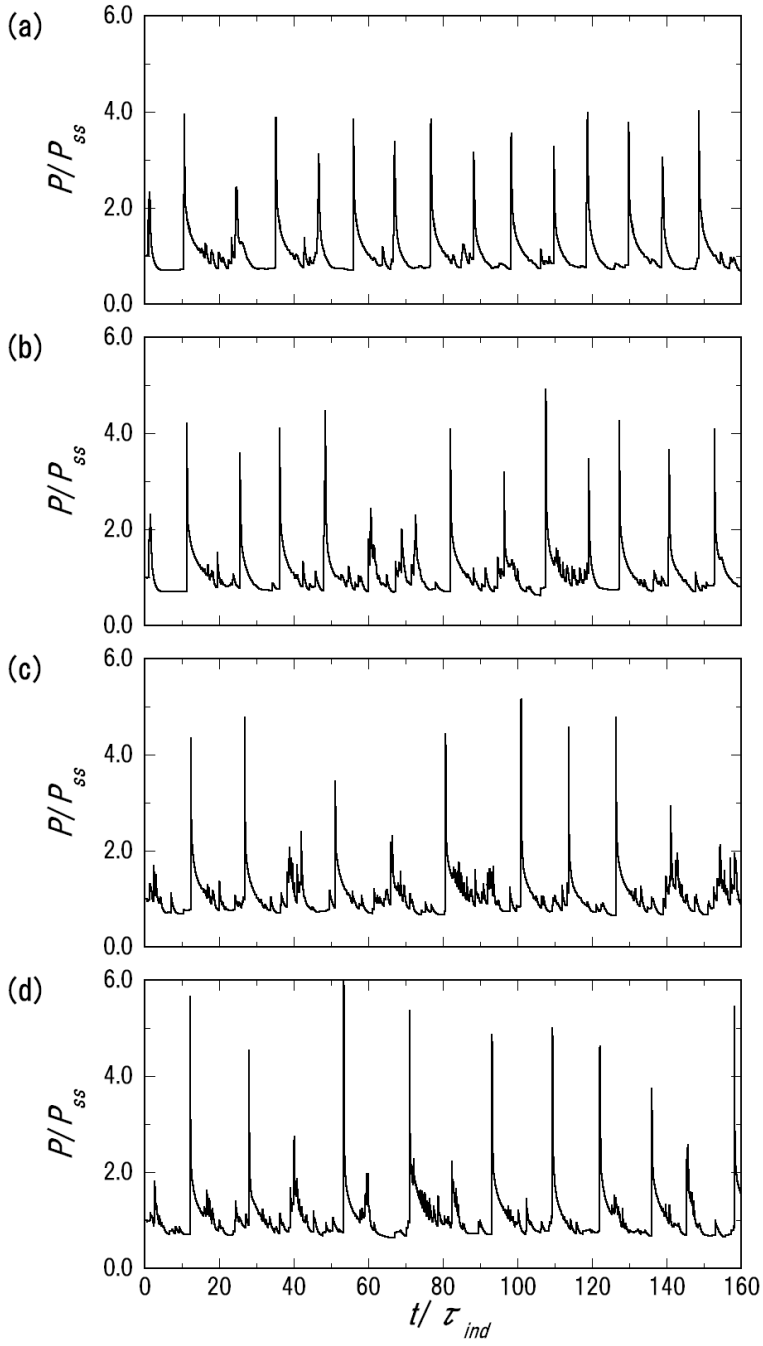

Figure 2.7: Shock pressure histories of a 1-D piston-supported detonation for SD case with $f = 1.2$. Grid resolution of (a) 20, (b) 40, (c) 80, and (d) 160 points / L_{ind}.

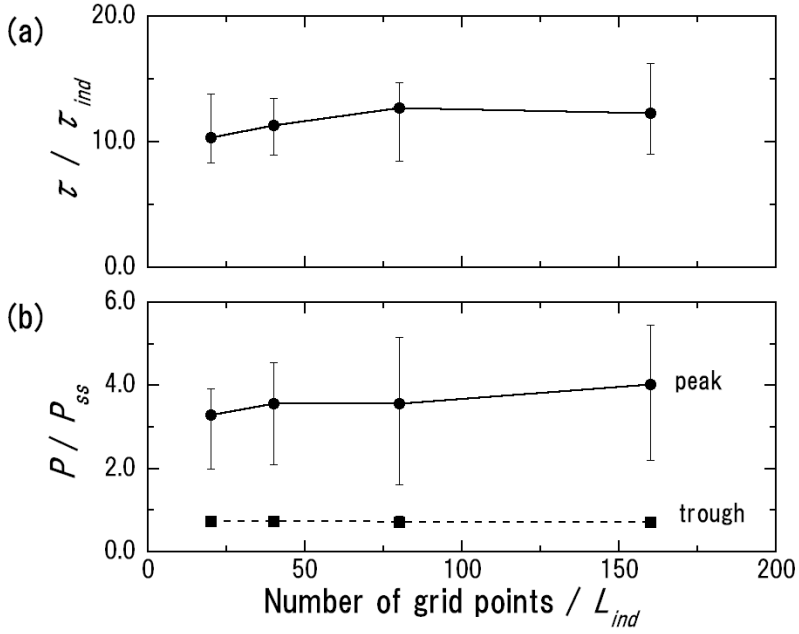

Figure 2.8: One-dimensional piston-supported detonations for SD case with $f = 1.2$. (a) Period of oscillations. (b) Pressure peak (solid line) and trough (dashed line).

oscillations, amplitude ΔP normalized by the shock pressure P_{ss} of steady solutions is about 0.25, and period τ normalized by the induction time τ_{ind} is approximately 1.5 for $1.6 \leq f \leq 2.0$. For $1.3 \leq f \leq 1.5$, the oscillations have high amplitude and low frequency as shown in Fig. 2.9(b); the low frequency mode. The normalized amplitude $\Delta P/P_{ss}$ is 1.0 ~ 4.0, and period τ / τ_{ind} ranges from 7.0 to 8.0. These numerical results show that the oscillation mode depends on the degree of overdrive as well as the previous works. For $1.1 \leq f \leq 1.2$, extremely unstable oscillations appear as shown in Fig. 2.9(c). This chaotic mode is also observed in the previous works as mentioned in §2.3.2. This is well-known as the oscillation characteristics in extremely low-overdrive detonations ($f \sim 1.0$).

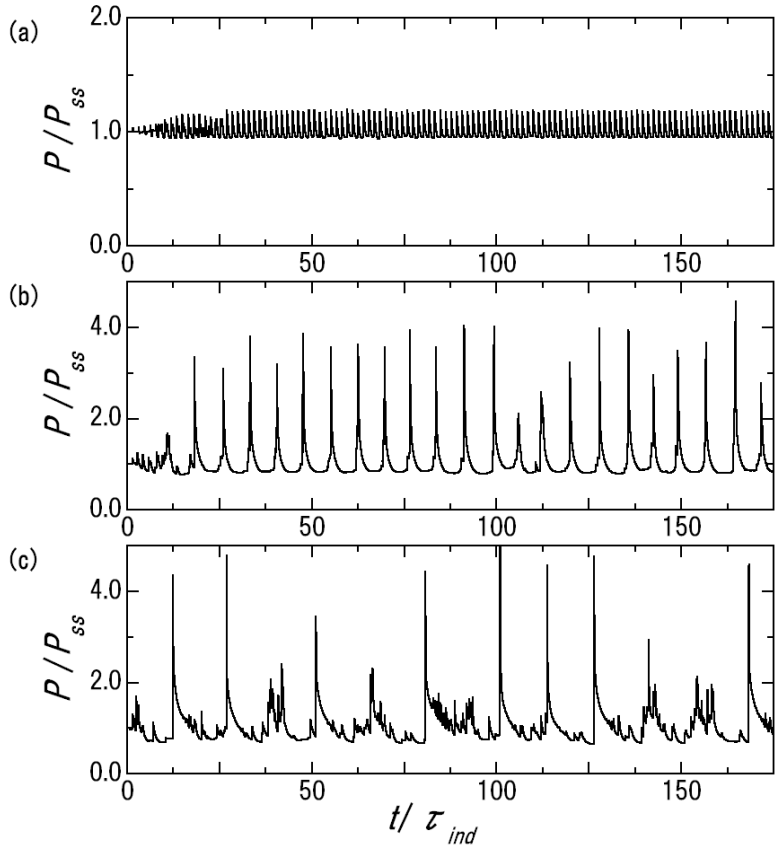

Figure 2.9: Post-shock pressure histories of one-dimensional piston-supported detonations for SD case. (a) f = 2.0. (b) f = 1.4. (c) f = 1.2. (P_{ss}, post-shock pressures of steady ZND detonations; τ_{ind}, induction times)

2.3.4 Oscillation transition in a decay process of a overdriven detonation developing from piston initiation (PI)

Figure 2.10(a) is the $x - t$ diagram of the density gradient in a piston surface stationary frame, and clearly shows the wave patterns in the whole computational domain for degree of overdrive $f = 1.2$. In Fig. 2.10(a), the shock is initiated by the piston at time 0.0 s, and the strong reaction front that is an interior detonation occurs at time 9.1 μs. The reaction front penetrates the shock front at time 11.3 μs, and simultaneously the strong rarefaction wave occurs and travels to the piston surface. After the penetration, oscillations of the shock front gradually appear, and period of the oscillations becomes longer and longer. A series of compression waves and contact discontinuities, which are released from the shock front, can be also seen in Fig. 2.10(a). Between time 14.0 and 27.5 μs, high and low frequency oscillations are observed. Figures 2.11(a) and (b) are the close-up view of Fig. 2.10 and exhibit the density contour distributions around the shock front. According to previous numerical studies of unsteady combustions around a blunt body projectile by Matsuo and co-workers, Figs. 2.11(a) and (b) are classified into the interaction mechanisms of the high frequency mode and the low frequency mode, respectively. The transition from the high frequency mode to the low frequency mode occurs under the fixed degree of overdrive 1.2, while the unique oscillation mode is observed for a given degree of overdrive in SD case.

The history of the shock pressure is presented in Fig. 2.10(b) to discuss the reason of the mode-transition from the high frequency mode to the low frequency mode. First, the pressure level is constant, and it is supported by the piston. Then, the shock pressure suddenly shows the peak due to the penetration of the reaction front on 11.1 μs. Since the detonation instantaneously propagates at higher velocity than $f = 1.2$, the leading shock is not self-sustained and its strength gradually weakens in a domain (i) [11.1 ~ 21.6 μs]. The flow feature in the do-

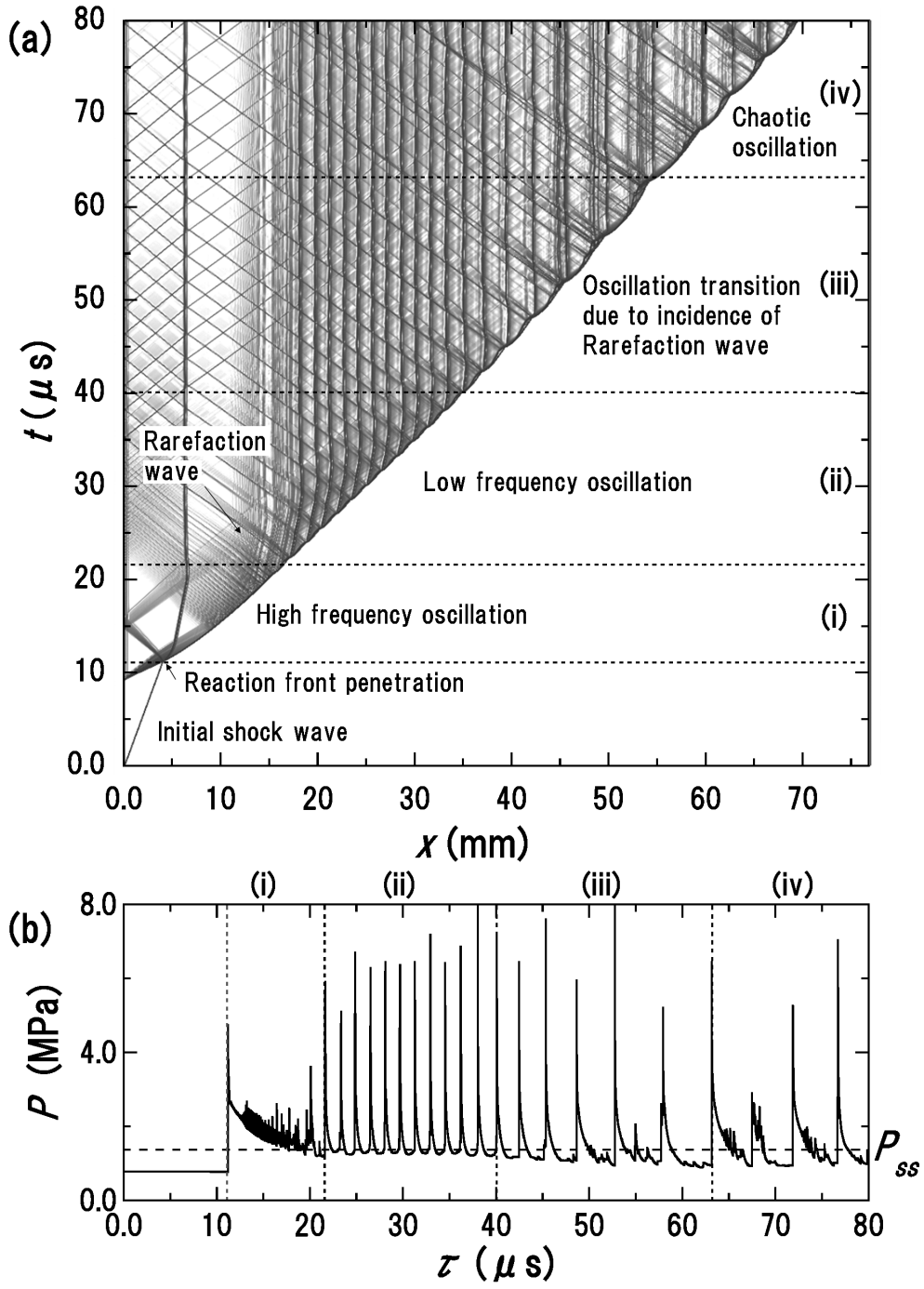

Figure 2.10: One-dimensional piston-supported detonations for PI case with $f = 1.2$. (a) $x - -t$ diagram of density gradient. (b) Post-shock pressure history.

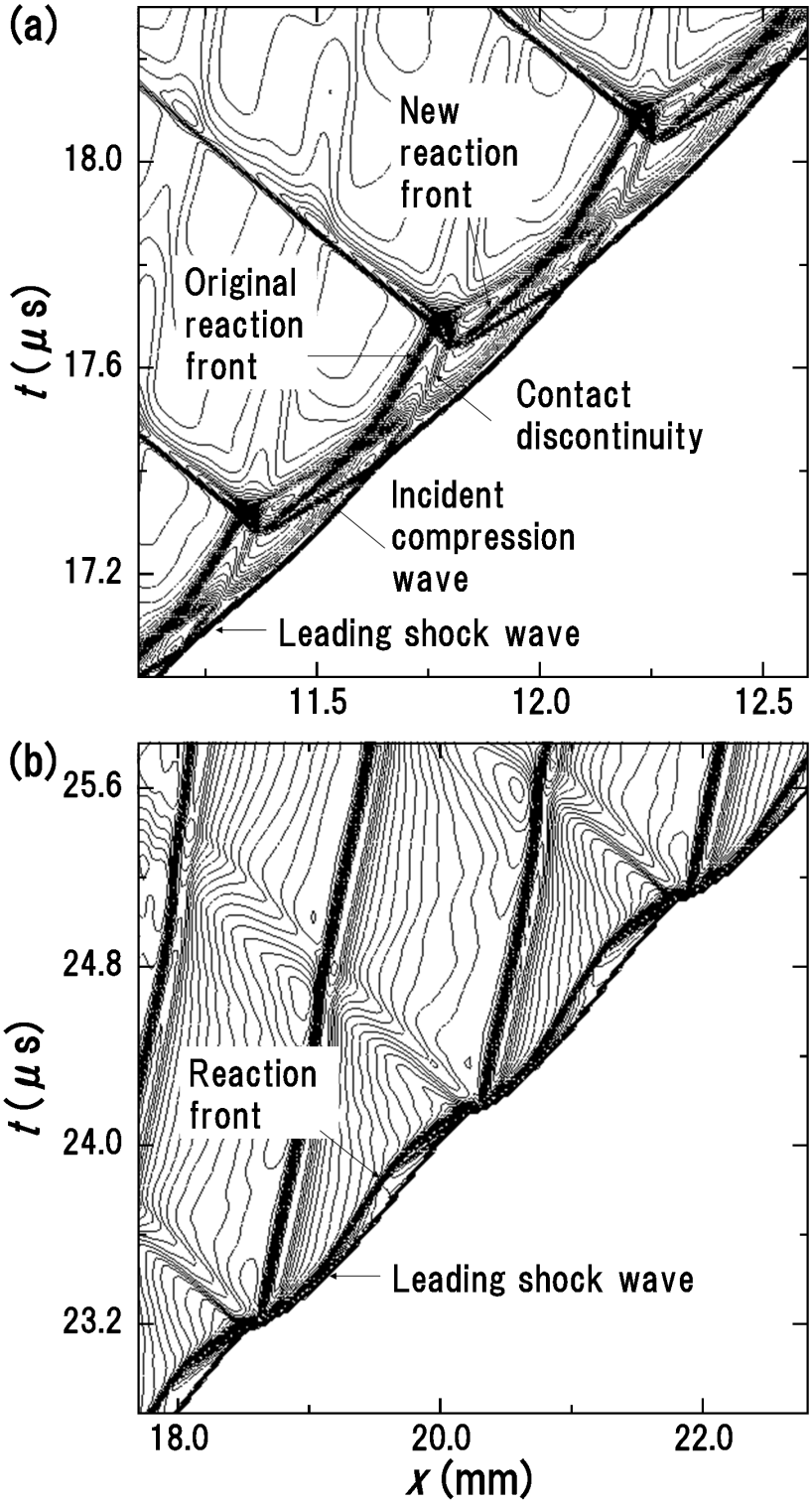

Figure 2.11: Enlargement of Fig. 2.10 in the form of density contour distributions. (a) High frequency mode. (b) Low frequency mode.

main (i) indicates the high frequency mode as shown in Fig. 2.11(a). After the first incidence of the rarefaction wave in a domain (ii) [21.6 ~ 40.1 μs], shock pressure becomes constant about 1.70 MPa, and the flow feature indicates the low frequency mode in Fig. 2.11(b). In a domain (iii) [40.1 ~ 63.2 μs], average shock pressure is attenuated by the second rarefaction wave that is originated in the penetration of reaction waves and is reflected off the piston surface. Average pressure in a domain (iv) [63.2 μs ~] becomes constant 1.39 MPa and the irregular oscillations occur, which is also observed in the previous numerical results of unsteady combustions around a cylindrical projectile (Kamiyama & Matsuo, 2000). Average pressure and the flow feature of PI case in the domain (iv) agree well with those of SD case (1.37 MPa, P_{ss}) with $f = 1.2$. Although the average pressure in SD case is constant for each degree of overdrive, the local average pressure in PI case decreases as a function of time. This suggests that the mode-transition in PI is due to decreasing the local average pressure. Accordingly, the period and the pressure peak (≧ 2.5 MPa, for the low and chaotic oscillations) and trough of oscillations are derived from the shock pressure history in Fig. 2.10(b). Each of the plots in PI case are arranged according to the post-shock pressure that is obtained from the average of pressures during a series of peaks in Fig. 2.12. Since the period of oscillation and the pressure peak and trough are instantaneous characteristics, PI plots with $f = 1.2$ are distributed widely throughout the graph. The plots of SD case are computed values with $f = 1.1 \sim 2.0$, and are roughly divided into three oscillation modes: the high frequency mode ($f \geq 1.5$); the low frequency mode ($1.4 \leq f \leq 1.3$); the chaotic mode ($f \leq 1.2$). The oscillation characteristics against shock pressures in PI case are mostly distributed in the error bars of SD plots. It is confirmed that longitudinal oscillation characteristics of the 1-D overdriven detonations have the strong dependence on the post-shock pressure.

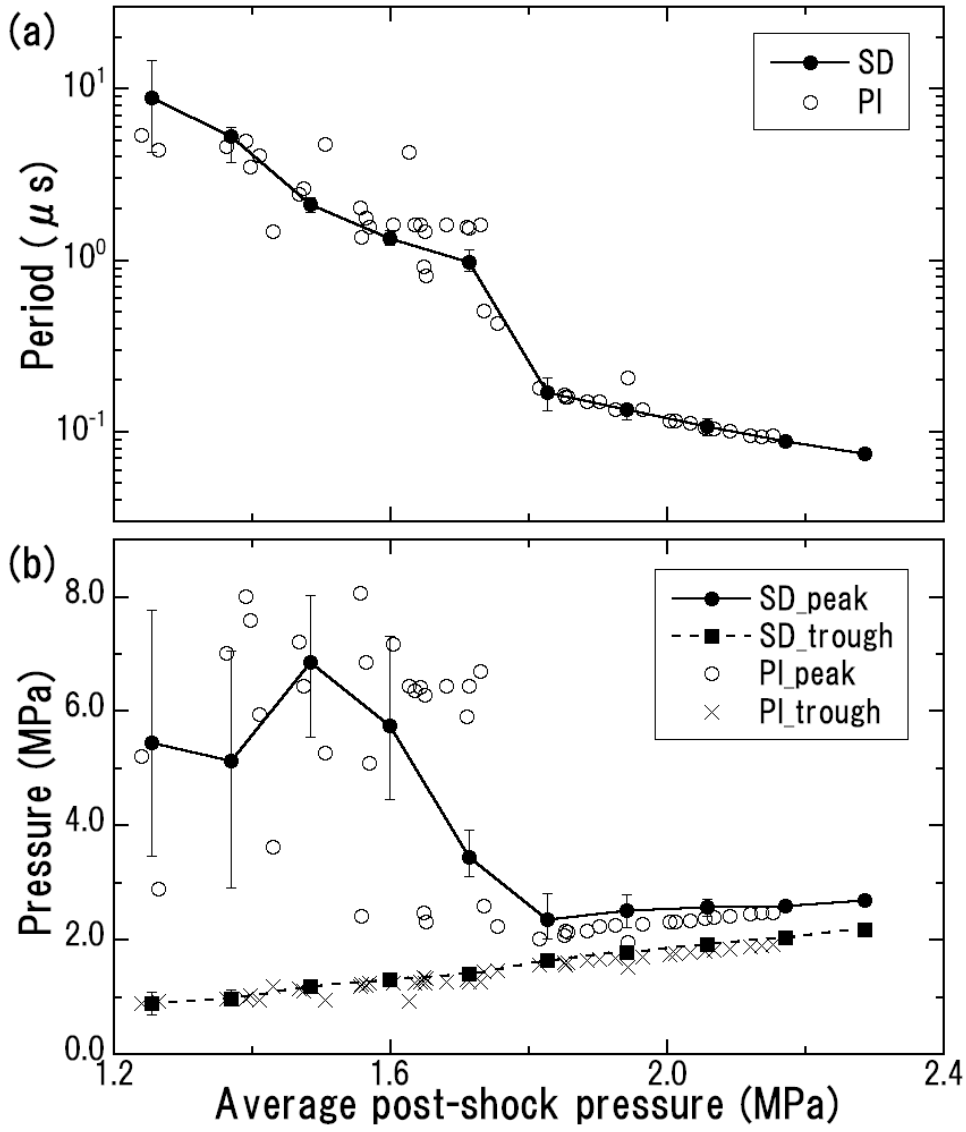

Figure 2.12: Relation between shock pressure *P* and oscillation characteristics; (a) Period τ. (b) Pressure peak and trough.

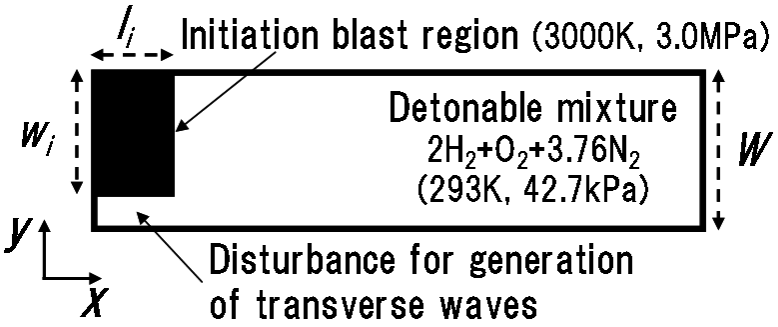

Figure 2.13: Schematic diagram of initial conditions, for two-dimensional detonation simulations with a two-step chemical reaction mechanism.

2.4 Two-Dimensional Detonation Simulations

2.4.1 Initial conditions and computational domains

Two-dimensional detonations with the two-step reaction mechanism are studied at the same initial conditions as Lehr's experiments in §2.3.1, varying a detonation tube width (channel width). The computational domains are listed in Table 2.3. Grid resolution along the x axis is provided with 10 points / L_{ind} (Table 2.2, $f = 1.0$): mesh size $\Delta x = 36.0$ μm; $\Delta y/\Delta x = 1.5$. Two-dimensional detonations are directly initiated by initial blast wave at 3000K and 3.0 MPa bounded on the left boundary ($x = 0.0$ mm) (see Fig. 2.13). Decay process from a highly overdriven detonation is reproduced in a laboratory coordinate system. The decay process is a similar situation to PI case in a sense that the strength of the leading shock gradually weakens due to the incident rarefaction wave.

When a detonation succeed in propagation with $W = 11.3 \sim 18.8 L_{ind}$, the initiation energy E_i in Table 2.3 is optimized to be minimum. If E_i is increased over the optimized one, a detonation temporally propagates with higher degree of overdrive than that with optimized energy, but finally converges into the same propagation behavior. According to Lee (1977), the

critical energy E_c for the initiation of a planar detonation is expressed as:

$$E_c = 3.636\rho_0 D^2 b, \tag{2.12}$$

where b is a detonation cell width. In the work of Stamps & Tieszen (1991), the cell width is 15.2 mm in the stoichiometric hydrogen-air mixture, initially at 50 kPa. Substituting b (= 15.2 mm) into eq. 2.12, the critical energy of the planar detonation E_c is expected at 76.04 kJ/m^2. In the present simulations, the cell width b, however, has a close relation to the channel width W (e.g. $E_c = 10W$ MJ/m^2 with $b = 2W$, assuming that a half cell appears in the channel). The initiation energy E_{init} is derived from the product of the length of the initiation region multiplied by the differential between the specific internal energy of initiation region e_{init} and its surroundings e_0: $E_{init} = l_i(e_{init} - e_0)w_i/W$, where l_i and w_i are length and width of the initiation region, respectively (refer to Fig. 2.13). To disturb the detonation front, W_i does not spread out on the whole channel width W; this is taken into account the initiation energy E_{init}. As shown in Table 2.3, even though insufficient initiation energy E_{init} is provided against the critical energy E_c, detonations succeed in propagating through the computational domain (216 mm) due to transverse waves with $W = 11.3 \sim 18.8L_{ind}$. The final oscillation in Table 2.3 is merely judged at x = 216 mm, and might not be the final properties.

2.4.2 Grid convergence study in two-dimensional simulations

For a grid convergence study, benchmark results of the channel width $W = 11.3L_{ind}$ (= 4.05 mm) and $W = 7.5L_{ind}$ (= 2.70 mm) are compared against results with finer grid resolution of 15 and 20 grid points / L_{ind}. For the reason of restricted computational resources, the number of grid points along the x axis is fixed on 6001 points. Figure 2.14 shows final oscillation characteristics of centerline pressure for a 2-D C-J detonation with $W = 11.3L_{ind}$. Although period of oscillation and pressure peak gradually change as the number of grid points / L_{ind} increases,

Table 2.3: Computational domain and initiation region of two-dimensional detonations. (1-D, one-dimensional oscillation; HF, High Frequency; LF, Low Frequency; cell, Cellular structure is observed at right computational boundary.)

Channel width	Computational	Detonation initiation		Final	
(W/L_{ind})	domain (mm)	region (mm)	E_{init} (kJ/m^2)	Oscillation	
2.25	216×0.81	7.20×0.54	37.2	1-D	Fig. 2.17(a)
3.00	216×1.08	6.50×0.81	50.4	1-D	Fig. 2.17(b)
3.75	216×1.35	1.80×0.81	13.9	HF	
	↓	3.60×0.81	27.9	HF	
	↓	5.40×0.81	41.8	HF	
5.63	216×2.03	1.44×1.50	13.5	LF	
	↓	1.80×1.50	16.9	LF	
	↓	3.60×1.50	33.7	LF	Fig. 2.17(c)
7.50	216×2.70	1.08×2.16	10.9	LF	Fig. 2.20
	↓	1.80×2.16	18.2	HF	
	↓	3.60×2.16	36.4	HF	
11.3	216×4.05	1.15×3.51	12.6	LF, cell	Fig. 2.20
15.0	216×5.40	1.08×4.32	10.9	LF, cell	Fig. 2.17(d), 2.20
18.8	216×6.75	1.08×5.67	11.4	LF, cell	

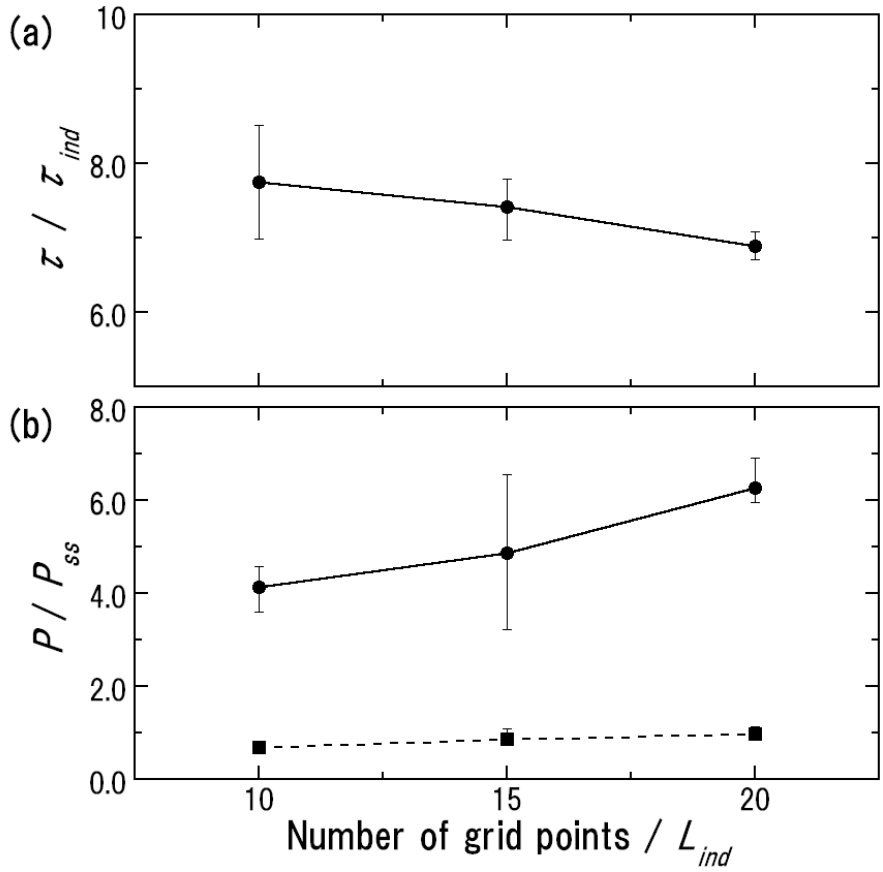

Figure 2.14: Oscillation characteristics on the centerline pressure, for a two-dimensional C-J detonation, initially at 293 K and 42.7 kPa with channel width $W = 11.3L_{ind}$. (a) Period of oscillations. (b) Pressure peak (solid line) and trough (dashed line).

the number of triple points appearing in the channel remains unity. With $W = 7.5L_{ind}$, all transverse waves finally disappear in the channel. The flow may be far from being properly resolved, but transverse-wave characteristics comparatively agree with each other. As a consequence, the following 2-D simulations are performed with 10 grid points / L_{ind} to grasp an overview of 2-D transverse oscillations.

2.4.3 Oscillation characteristics of two-dimensional detonations

Figure 2.15(a) shows the maximum pressure history of a detonation in the form of the gray scale distribution with $W = 11.3L_{ind}$. The history is recorded as the maximum pressure experienced at each point in the channel. Darker color indicates higher pressure. Most of high pressure regions consist of triple point tracks. The history, however, includes all the maximum pressures behind the shock front, and thus explosions behind the shock front also appear. The detailed shock structures and the formation of high pressure regions will be discussed in the following §3. In this section, oscillation characteristics of the leading shock wave are examined to compare with 1-D characteristics of oscillation. Figure 2.15(b) shows the leading shock velocity of a detonation in the same channel width of Fig. 2.15(a). In this case, only the frontal information of a detonation is depicted, and the outlines of cellular structures clearly emerge. The number of the lines across the channel corresponds to the number of frontal triple points. In Fig. 2.15(b), the traces of triple points once disappear and reappear on the top and the bottom boundaries. Those jumps for the last two cells are drawn as arrows in Fig. 2.15(b). When the triple point collides with the boundary, post-shock temperature instantaneously increases. Therefore, the induction time rapidly decreases, and the reaction front overtakes and intensifies the leading shock. This is the mechanism why the leading shock velocity suddenly jumps forward on those boundaries.

The tone before 40 mm in Fig. 2.15(b) is generally darker than those of the rest of the domain. This implies that the detonation initiated by a blast wave at high pressure and temperature leads temporally overdriven state in the domain during $x = 0.0 \sim 40$ mm. The tone becomes lighter as the detonation propagates, and thus the overdriven detonation is gradually attenuated by a rarefaction wave. In the decay process, cellular structures in a domain ($x = 40 \sim 80$ mm) have well-defined two triple points, and after $x = 80$ mm, only single triple

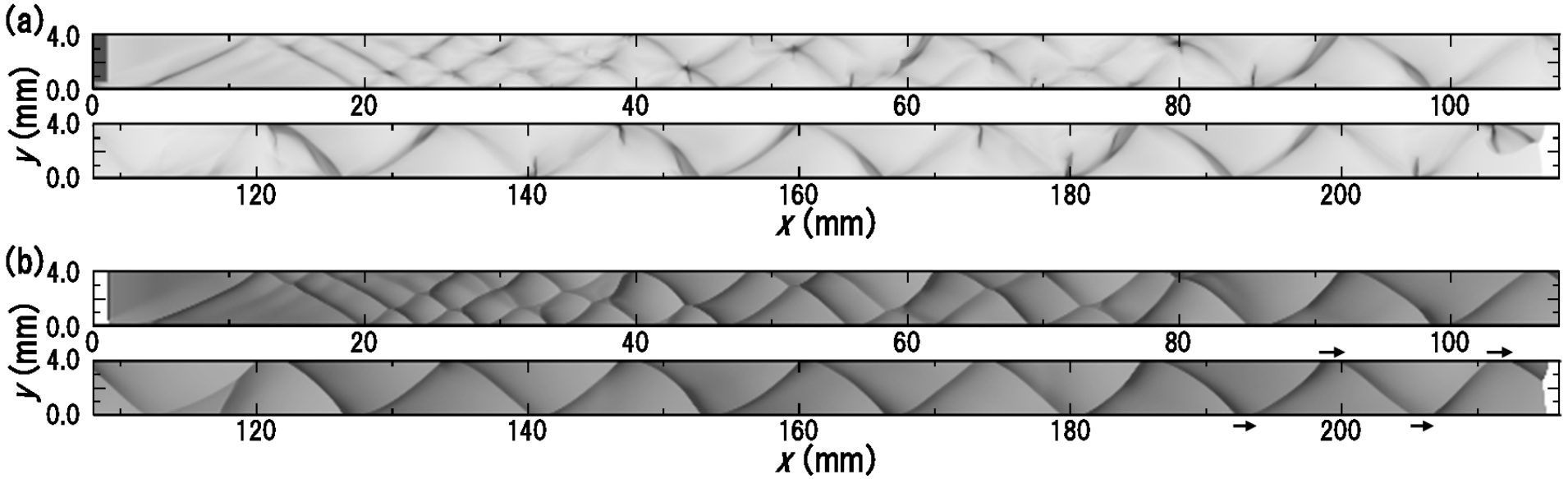

Figure 2.15: Two-dimensional cellular structures in the form of gray scale distribution with $W = 11.3L_{ind}$. (a) Maximum pressure history. (b) Leading shock velocity. The darker color indicates (a) higher pressure and (b) faster velocity. Velocity jumps are presented as arrows on the top and the bottom boundaries of the last two cells in (b).

point propagates through the channel. Although the initiation process of the 2-D detonation is different from the 1-D PI case, the similar transition on oscillation characteristics appears in both simulations.

Figure 2.16 shows histories of post-shock pressure and the instantaneous degree of overdrive f in the direction of x axis on the bottom boundary (y = 0.0 mm) in Fig. 2.15. Since the post-shock pressure P is given as a linear function of degree of overdrive f, histories of P and f are on the same profile in the graph with double axes. Histories of the post-shock pressure P and the degree of overdrive are transformed from the distribution of the leading shock velocity in Fig. 2.15(b). According to Fig. 2.16, the shock pressure P (solid line) oscillates from 0.41 MPa to 4.2 MPa, and the average pressure P_{Ave} (dotted line) gradually decreases to the post-shock pressure P_{ss} (= 1.14 MPa) of steady C-J detonations. Instantaneous degree of overdrive f in the direction of the x axis (solid line) varies from 3.7 to 0.36, and the average degree of overdrive f_{Ave} (dotted line) asymptotically decreases from 1.6 to almost 1.0. Here, average values are merely approximated by logarithmic functions, and exact averages during one periodic cycle will be discussed later.

Figure 2.17 shows histories of a post-shock pressure of representative cases with various channel widths in Table 2.3. Oscillation period and amplitude gradually change as detonations propagate. In Fig. 2.17(a), the post-shock pressure oscillates as if 1-D longitudinal oscillations (low frequency) and 2-D transverse oscillations (high frequency) appears simultaneously. Figure 2.17(b) shows initially high frequency oscillations, but lately 1-D oscillations. Since there must be enough time between transverse wave collisions and reflections for the Mach stems to have sufficiently weakened when the wave reverse direction, one expects a minimum possible transverse wave spacing (Fickett & Davis, 1979). The decline of transverse waves is observed in numerical simulations by Sharpe & Falle (2000), and reported in experiments with a very narrow rectangular tube by Strhelow (1968). In Fig. 2.17(c), (d), oscillations

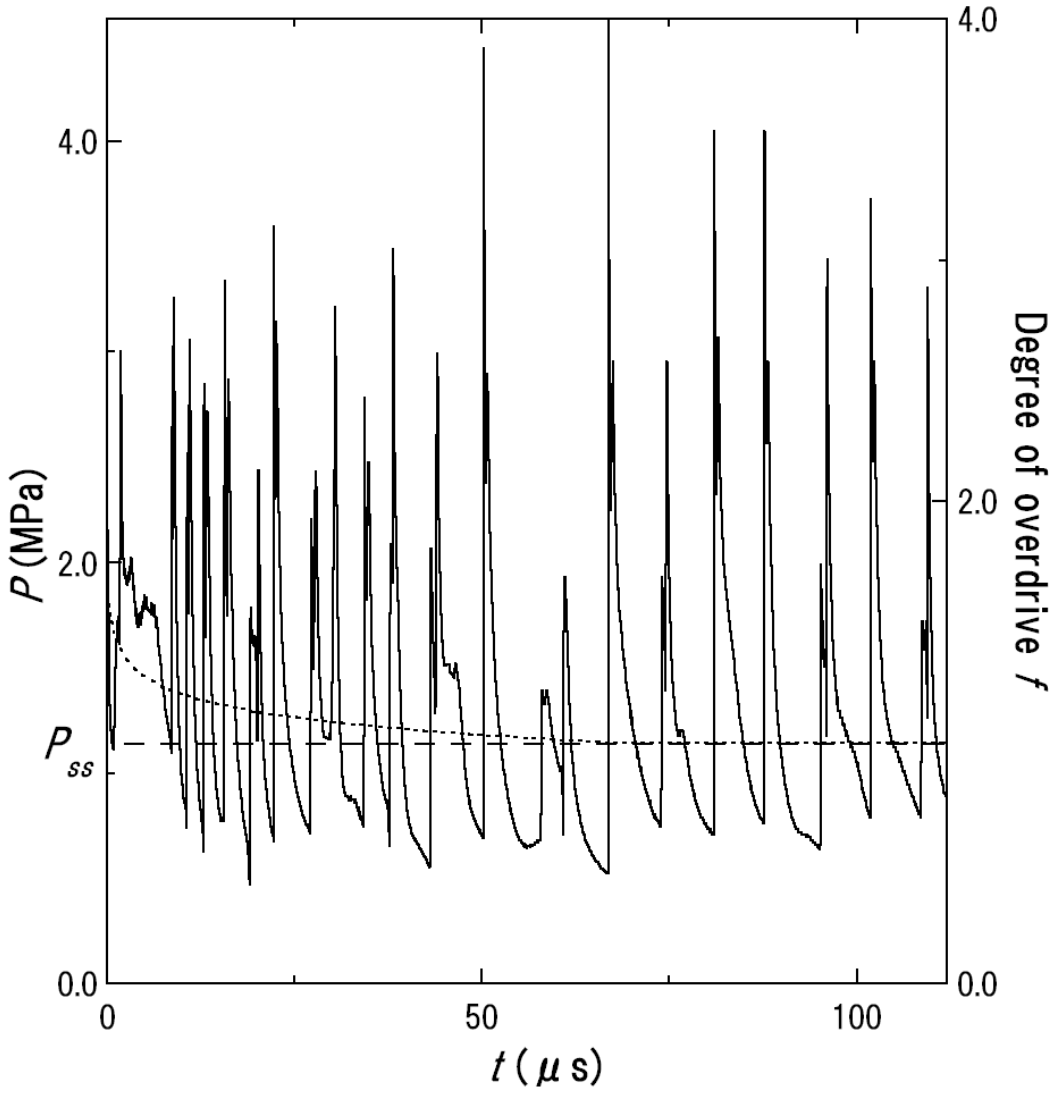

Figure 2.16: Centerline pressure and velocity of the leading shock (solid line) in the channel width $W = 11.3L_{ind}$; P_{Ave}, average pressure & f_{Ave}, degree of overdrive (dotted line); P_{ss}, post-shock pressure of a steady C-J solution (broken line).

Table 2.4: Characteristics of cellular structure, for two-dimensional C-J detonations in various channel width; a/b, cell aspect ratio; $\bar{U}_T$, transverse wave velocity.

W/L_{ind}	a (mm)	b (mm)	a/b	$\bar{U}_T$ (m/s)	τ (μs)
3.75	5.80	2.70	2.15	917.	2.94
5.63	8.08	4.06	1.99	966.	4.20
7.50	10.1	5.40	1.87	1030.	5.27
11.3	13.5	8.10	1.67	1160.	6.96
15.0	16.3	10.8	1.51	1280.	8.41

initially indicates high frequency and progresses to low frequency. The final oscillation periods most likely depends on the channel width. To discuss this further, final oscillation properties due to transverse waves are examined. Summary of oscillation characteristics are drawn in Fig. 2.18. Through the last several oscillations which have larger pressure peaks, it is confirmed that average degree of overdrive is close to unity, whether transverse waves finally appears or not. Periods of oscillation increase as the channel width increases. Pressure peaks also increase with the channel width, while pressure trough remains almost constant.

Several cells that finally appear in a channel are examined to obtain velocities of transverse waves with $W = 3.75 \sim 15.0 L_{ind}$ where a single transverse wave appears in a channel. Aspect ratios a/b of cellular structures are derived from pressure histories (Fig. 2.17); a, cell length; b, cell width. The average velocity of a transverse wave $\bar{U}_T$ is represented as $\bar{U}_T = \sqrt{f} D_{CJ} b/a$. For the final degree of overdrive ($f_{Ave} \simeq 1.0$), average velocities of transverse waves are calculated and listed in Table 2.4. As increasing the channel width, the aspect ratio of a cell reduces, and the average velocity of a transverse wave increases. Hence, periods of oscillation do not linealy increase with the channel width.

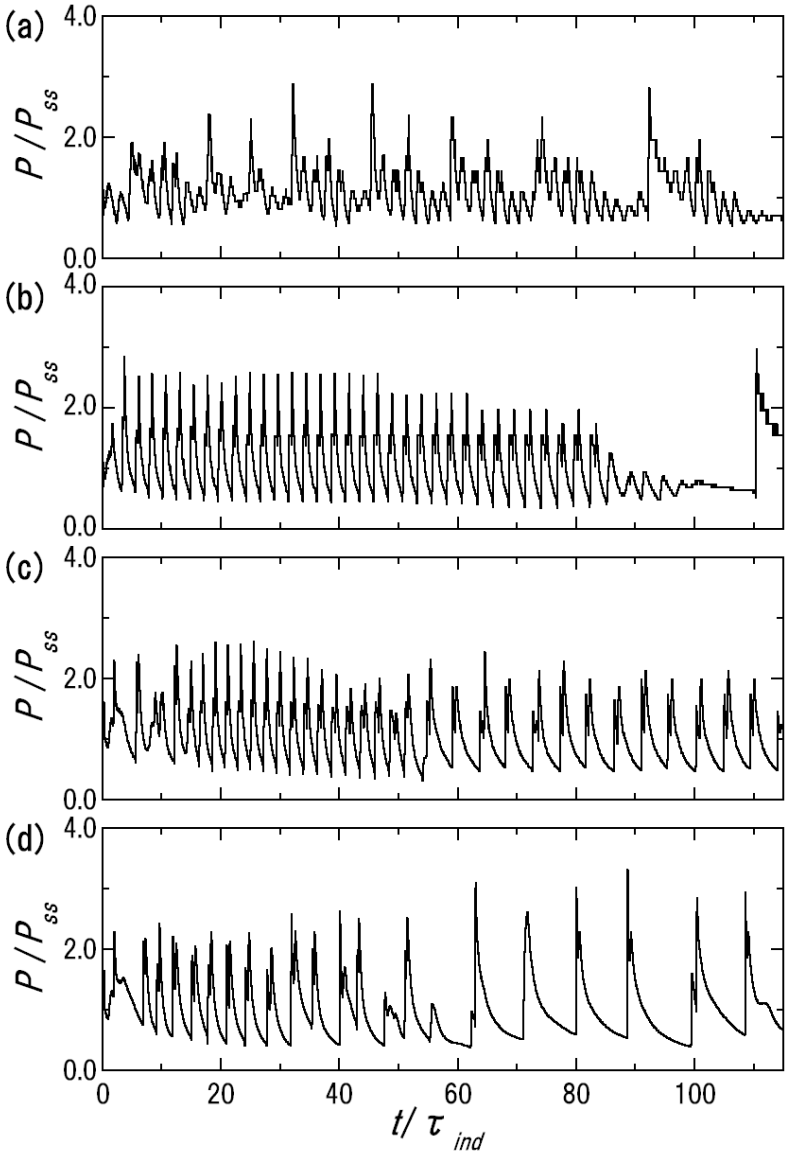

Figure 2.17: Centerline pressure of the leading shock (y = 0.0 mm), for a two-dimensional C-J detonation in the channel width of (a) 2.3, (b) 3.0, (c) 5.6, (d) 15. L_{ind}.

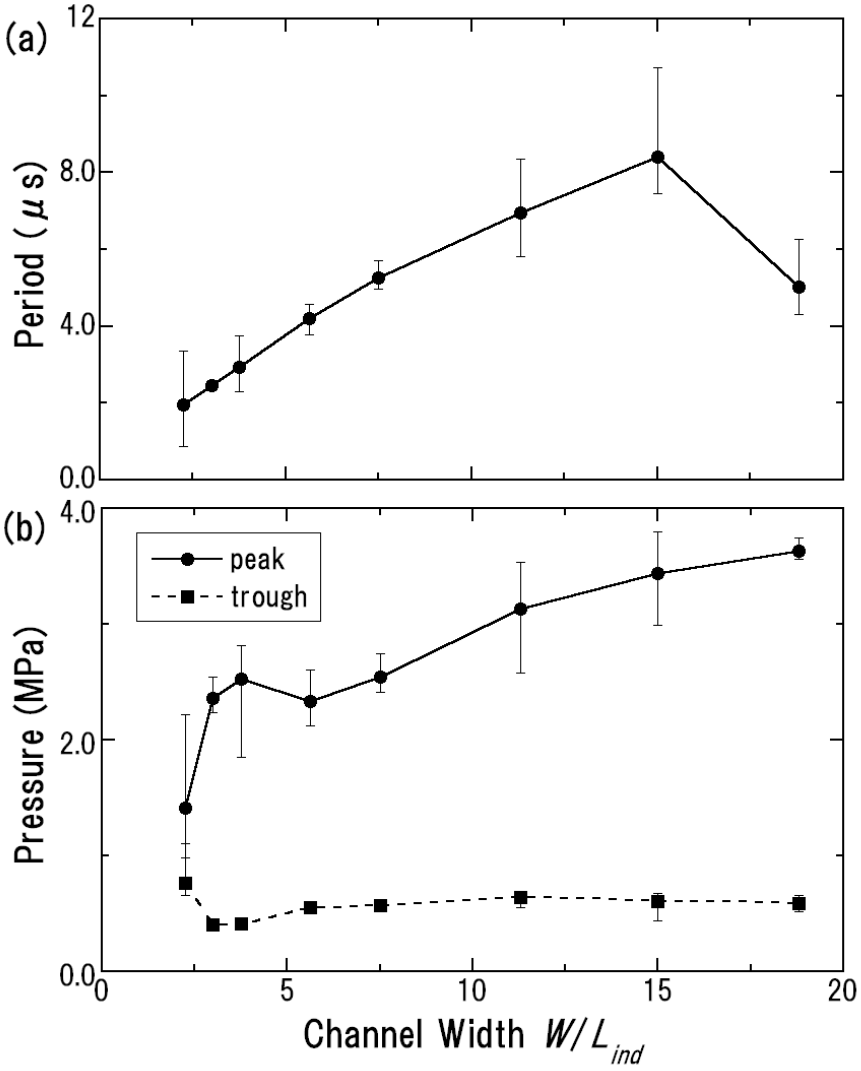

Figure 2.18: Relation between oscillation characteristics on the centerline pressure and channel width, for a two-dimensional C-J detonation. (a) Period of oscillations. (b) Pressure peak (solid line) and trough (dashed line).

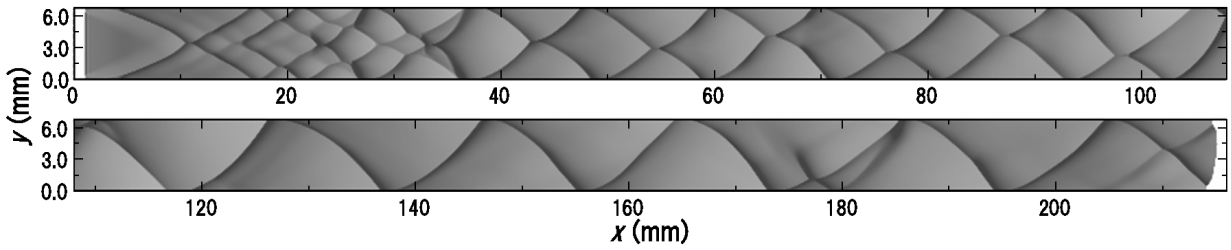

Figure 2.19: Two-dimensional cellular structures of the leading shock velocity in the form of gray scale distribution with $W = 18.8L_{ind}$.

In the channel $W = 18.8L_{ind}$, a triple point newly appears at $x = 170 \sim 180$ mm as shown in Fig. 2.19. The marginal channel width in which a single triple point exists is $W = 15.0L_{ind}$. The second triple point gradually develops into a dominant at the end of the computational domain. The oscillation period decreases because of the occurrences of the new triple points. Oran *et al*. (1998) reported that new triple points are formed from the Mach stem inflection points. The Mach stem usually propagates at a faster speed than the C-J speed. Hence, the 1-D instability might affect the Mach stem inflection. This will be discussed in the next section.

2.4.4 Comparison of one- and two-dimensional characteristics

In this section, one- and two-dimensional oscillations are attempted to be directly compared. One-dimensional characteristics of oscillations have been already obtained in 1-D overdriven detonations of SD cases (Fig. 2.20). Average post-shock pressures (P_{ss}) are larger than 1.2 MPa. On the other hand, 2-D oscillations are obtained on the center line of final several cells with $W = 7.5 \sim 15L_{ind}$. These plots are derived by averaging post-shock pressure per a cycle for final several cells. Although averaged post-shock pressure per a cycle ranges from 0.8 to 1.25 MPa, all periods obtained in the same channel width are close to the averaged period. It is difficult to

obtain 1-D oscillations near the C-J conditions, because much more grid points (grid resolution) must be prepared for the chaotic behaviors and the longer and sensitive induction times to the post-shock conditions. The orders of 2-D periods are comparatively close to the order of 1-D periods for the low degree of overdrives. It is readily apparent that the 2-D transverse oscillations are associated with the 1-D longitudinal instabilities. As has been mentioned, 2-D periods of oscillation increase with the channel width. The period with more than $W = 15L_{ind}$ decreases due to the occurrence of a new triple point. A new triple point conveniently appears as if the original 2-D periods became larger than the 1-D periods by increasing the channel width. The difference of pressure peaks between 1-D and 2-D in Fig. 2.20(b) would be caused by the effects of double peaks in the pressure histories, or might be caused by insufficient grid resolutions of 2-D simulations.

2.5 Summary

One-dimensional overdriven detonations were successfully simulated with Korobeinikov's two-step reaction mechanism for stoichiometric hydrogen-air mixture, initially at 42.7 kPa and 293 K. Two kinds of unsteady oscillations that have been observed in unsteady combustions around blunt body projectile were also observed in 1-D overdriven detonations. The simulation started from steady ZND solutions of propagating detonations indicated the high frequency and the low amplitude oscillations for degree of overdrive from 1.6 to 2.0, the low frequency and high amplitude oscillations for degree of overdrive from 1.3 to 1.5, and the chaotic oscillations for degree of overdrive 1.1 and 1.2. The simulation started from overdriving a quiescent combustible gas by a piston for a constant degree of overdrive 1.2 exhibited above three oscillation modes, depending on the locally-averaged post-shock pressure. The relation between the average pressure and the oscillation characteristics such as period and amplitude in the piston initiation case was

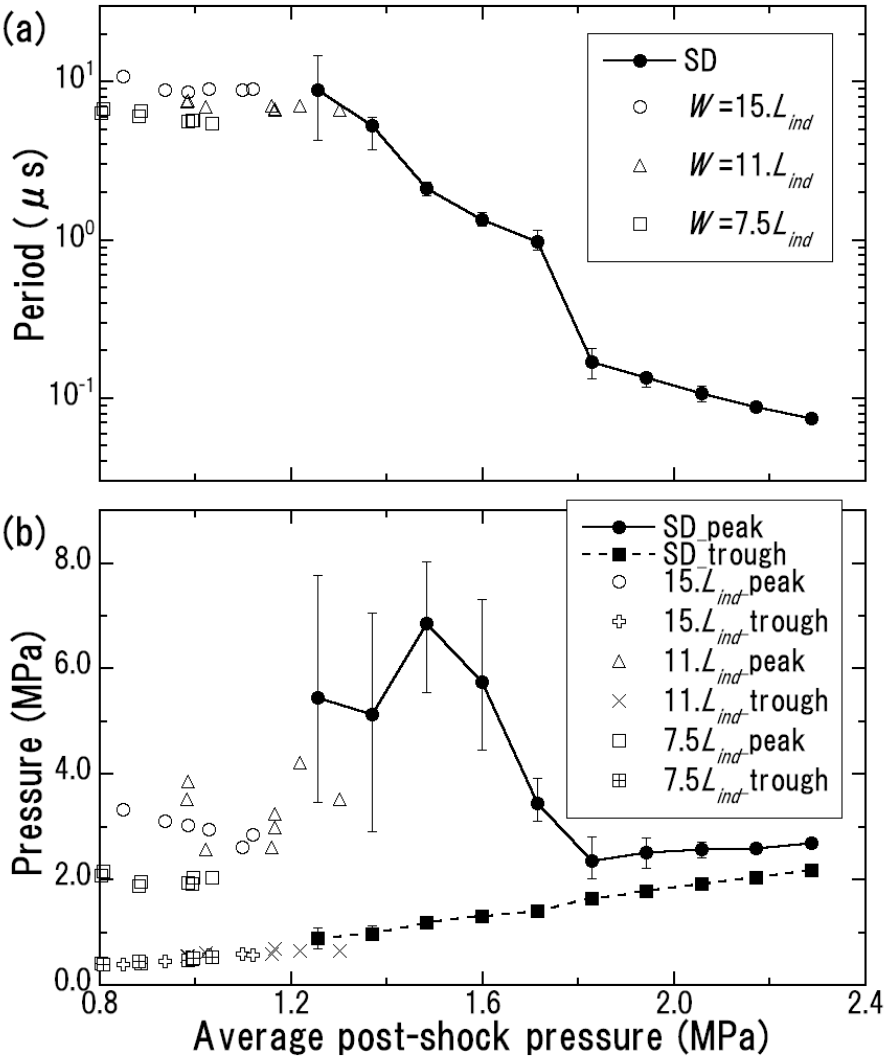

Figure 2.20: Relation between shock pressure P and oscillation characteristics; (a) Period τ. (b) Pressure peak and trough.

in good agreement with those of the oscillations developed from steady detonations.

With the same initial mixture conditions, 2-D detonations were simulated to reveal the relation between 1-D and 2-D oscillations. The 2-D detonations were initiated by initial energy release in blast waves. Oscillation periods on the centerline of the cell in 2-D detonations increased as a nonlinear function of the channel width because the average transverse waves also increase with the channel width. The order of 2-D periods were supposed to depend on the post-shock pressure averaged during one cycle, and comparatively well agreed with the order of 1-D periods extrapolated from larger post-shock pressures. A new triple point was observed on the Mach stem as if the original 2-D periods became larger than the 1-D periods by increasing the channel width. It was suggested that 2-D transverse oscillations are associated with the 1-D longitudinal instabilities.

Chapter 3

Detonations in Two-Dimensional Channels

3.1 Cellular Structures in Detonations

Kailasanath (2000) reported that a number of studies have been conducted on pulse detonation engines (PDEs) over the past decade. These devices use detonation waves that propagate through a premixed fuel-air mixture, which results in constant-volume combustion with high operating frequencies and high combustor chamber pressures. Use of detonation waves has advantages of a simplification of mechanical devices, such as turbo pumps. To achieve high PDE performance and stability in operating PDEs, their characteristics and the detailed mechanisms of propagating detonation must be clarified. Applied fuels to PDEs are assumed to be hydrogen and hydrocarbon mixtures. In §3, hydrogen-oxygen detonations are investigated with diluent of nitrogen or argon. Hydrocarbon pulse detonation rocket engines (PDREs) are simulated in Appendix G.

Cellular structures of gaseous detonations have been investigated experimentally with smoke foil records (Strehlow & co-workers, 1967, 1968, 1969, 1970, 1974; Urtiew, 1970; Bull *et al*., 1982; Shepherd, 1986; Stamps & Tieszen, 1990; Hannana *et al*., 2001), schlieren techniques (Soloukhin, 1966; Edwards *et al*., 1970; Takai *et al*., 1974; Radulescu *et al*., 2004), and PLIF for reaction zone structures (Pintgen *et al*., 2003). As for numerical simulations of cellular detonations, the first attempt to simulate 2-D detonations was performed by Taki & Fujiwara (1978). Kailasanath (1985) attempted to understand the effect of channel width on cellular structures. Shock configurations and distribution of energy release of detonation

have been investigated by Bourlioux & Majda (1992), Lefebvre & Oran (1995), and Oran *et al*. (1998). Lefebvre *et al*. (1993) also revealed the influence of the heat capacity on the irregularity of cellular structures with a simplified reaction mechanism. The detonation that had more than three or four cellular structures across a channel were successfully simulated and visualized in the form of maximum pressure histories by Gamezo *et al*. (1999a, 1999b). One of the biggest problems of detonation simulations is resolution around a detonation front. An adaptive mesh refinement (AMR) algorithm solves this difficulty by increasing the resolution locally, as required by the changing physical conditions. With the AMR technique, Gamezo *et al*. (2000) investigated the detail shock structure of a marginal detonation. Sharpe & Falle (2000b) discussed the stability of 2-D detonations with high-resolution simulations achieved by the AMR, and Sharpe (2001) also revealed that the cellular structures depend on the grid resolution.

A main feature of gaseous detonation is the complex interaction of incident shocks, Mach stems, and transverse waves (Fig. 1.1). Triple points are formed at the intersection of the transverse wave with the Mach stem and the incident shock, and diamond-shaped patterns called cellular structures are left on smoked foils. Detonations are classified into marginal and ordinary. An ordinary detonation is usually observed in a rectangular tube. On the other hand, marginal detonation denotes detonation in a system near the detonation limit, and would fail if the pressure were a little lower or the tube depth a little smaller. Frontal structure has been examined and three types of interaction geometries clarified by Lefebvre & Oran (1995) (Fig. 3.1). In a single Mach reflection (Fig. 3.1(a), the whole transverse wave is organized by a relatively weak reflected shock connected by the frontal triple point A. In a complex Mach reflection (Fig. 3.1(c)), the small front piece of the transverse wave is the reflected shock, although most of segment BC is a detonation. A double Mach reflection (Fig. 3.1(b)) is placed in the intermediate structure between the single Mach reflection and the complex Mach reflection.

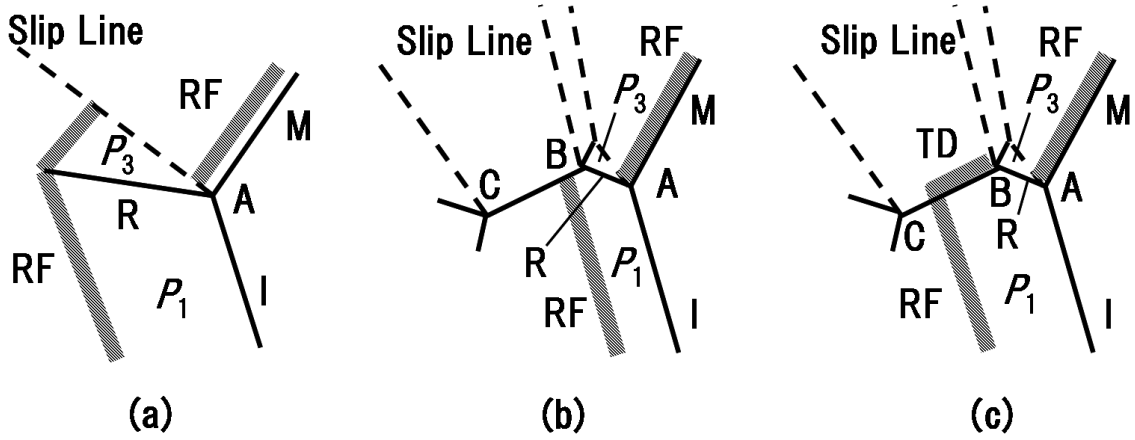

Figure 3.1: Three shock configurations of frontal detonation structures. (a) Single Mach reflection. (b) Double Mach reflection. (c) Complex Mach reflection. (M, Mach stem; I, Incident shock; R, Reflected shock; RF, Reaction Front; TD, Transverse Detonation).

Strehlow & Biller (1969) defined the instantaneous transverse wave strength S to evaluate the transverse wave that plays an important role in detonation propagation. For pressures of P_1 and P_3 shown in Fig. 3.1, the transverse wave strength S is defined by the following equation $S = P_1/P_3 - 1$. The transverse wave strengths are characterized experimentally by using inert gas dynamic computations with the information of entrance angles left on smoked foil records. Fickett & Davis (1974) summarized the works of Strehlow & Biller (1969) and Edwards *et al.* (1970), and suggested that if the cell width of the ordinary detonation is controlled by an acoustic mechanism, the transverse wave strength S becomes approximately constant at $0.3 \sim 0.7$ with an average value of about 0.5. The difference in the transverse wave strength between the ordinary detonation and the marginal detonations is continuous and the transverse wave strength S of the marginal detonation increases up to 1.5.

Cell widths in Chapman-Jouguet (C-J) detonations have been experimentally measured in hydrogen-oxygen-diluent mixtures. For an explosive mixture, the cell width is a function of initial temperature, initial pressure, equivalence ratio, and inert diluent. These results

indicate that both an acoustic mechanism and a characteristic chemical length are the major controlling factors in determining cell widths. Several 1-D calculations have been made on the characteristic length for the energy release by Strehlow *et al.* (1969), Strehlow & Engel (1969), Barthel (1974), Westbrook (1984), and Shepherd (1986), and this length is correlated empirically with the experimental cell width through a proportionality factor. As a function of initial pressure, the cell width for hydrogen-oxygen mixtures shows a straight-line relationship in marked contrast to a curve for stoichiometric hydrogen-air mixtures (Bull *et al*., 1982; Stamps & Tieszen, 1991). The nonlinear behavior of hydrogen-air has been explained by the differences in reaction rates between various competing chemical reactions that make up the overall reaction scheme at the lower temperatures, associated with reducing initial pressure.

In a hydrogen-oxygen system, a distinctive cellular pattern has been seen to become extremely regular if the mixture contains over 40 % of monatomic gas as a diluent (Strehlow *et al*., 1969). Previous experiments of Takai *et al*. (1974) showed that when monatomic argon is replaced by molecular nitrogen, the structure becomes irregular. A mixture diluted with argon has the larger specific heat ratio, producing the higher temperature behind the shock front for a given shock. When the post-shock temperature is relatively low at about 1000 K, the induction distance is larger and more sensitive to fluctuations that can lead to hot or cold spots in the flow (Lefebvre *et al*., 1993). Takai *et al*. (1974) studied the irregularity of hydrogen-air mixtures. These authors examined post-shock conditions and discussed the change in system properties when hydrogen-oxygen mixture is diluted with nitrogen, which interferes with the chain-branching reaction and destroys the regular structure. Their results suggest that irregular patterns may be associated with systems near the detonation limit. In general, regular structure appears to be favored by low initial pressure and dilution with inert gases.

Acoustic coupling criterion is constructed on acoustic vibrations in detonation products driven by disturbances on the detonation front (Strehlow, 1968). The criterion assumes that

there is a finite-amplitude transverse wave attached to an acoustic wave propagating in the detonation products at the C-J condition. In the detailed chemical reaction mechanism, the chain-branching reactions corresponding to the detonation limit and the local speed of sound corresponding to the acoustic coupling are treated properly. First, in §3.3, a grid resolution study is performed for reliance on the computations. Second, in §3.4.1, channel width, initial pressure, and inert diluent are treated as parameters, and the transverse wave strength is examined. The maximum channel widths W_{max} where a single transverse wave appears are detected for different initial conditions. In the maximum channel width W_{max}, unsteady behaviors and propagation velocities of transverse waves are examined in §3.4.2. Second explosion limit for hydrogen fuel mixtures is discussed in §3.4.3, and the mechanism causing the irregularity of cellular structures in the mixture diluted with nitrogen is investigated in §3.4.4 based on the acoustic coupling criterion. The transverse wave intensity is newly proposed to estimate transverse waves that play important role in detonation propagation.

3.2 Numerical Setup

3.2.1 Governing Equations

The computations are modeled for a detonation propagating in a stoichiometric hydrogen-oxygen mixture diluted with nitrogen or argon ($2H_2+O_2+3.76N_2/3.76Ar$) at the initial pressures and temperatures listed in Table 3.1. The C-J detonation velocity, D_{CJ}, derived using STANJAN v.3.95 (Reynolds, 1986), and the half reaction length, $L_{1/2}$, are calculated by 1-D steady ZND simulations and are also listed in Table 3.1. The half reaction length, $L_{1/2}$, is defined as the distance behind the shock where the mass fraction of hydrogen is equal to the average of the free stream value and the equilibrium steady state value in 1-D steady C-J detonations.

The governing equations are the 2-D Euler equations for a chemically reacting gas

Table 3.1: Initial mixture conditions, for 2-D simulations with a detailed chemistry.

Case	P_0 (MPa)	T_0 (K)	Diluent	D_{CJ} (m/s)	$L_{1/2}$, μm
a	0.1013	293	N_2	1979.5	167.3
b	0.0133	293	N_2	1931.7	1177
c	0.1013	293	Ar	1862.1	41.47
d	0.0133	293	Ar	1790.6	394.5

mixture and the thermo-chemical data used for the 9 species are obtained from NASA thermo-chemical polynomials (Gardiner, 1984, Appendix C) as:

$$\frac{\partial \mathbf{U}}{\partial t} + \frac{\partial \mathbf{F}}{\partial x} + \frac{\partial \mathbf{G}}{\partial y} = \mathbf{S} \tag{3.1}$$

$$\mathbf{U} = \begin{bmatrix} \rho \\ \rho u \\ \rho v \\ E \\ \rho_i \end{bmatrix}, \mathbf{F} = \begin{bmatrix} \rho u \\ \rho u^2 + P \\ \rho uv \\ (E + P)\, u \\ \rho_i u \end{bmatrix}, \mathbf{G} = \begin{bmatrix} \rho v \\ \rho uv \\ \rho v^2 + P \\ (E + P)\, v \\ \rho_i v \end{bmatrix}, \mathbf{S} = \begin{bmatrix} 0 \\ 0 \\ 0 \\ 0 \\ \omega_i \end{bmatrix} \tag{3.2}$$

$$\rho = \sum_{i=1}^{9} \rho_i \tag{3.3}$$

$$P = \sum_{i=1}^{9} \rho_i R_i T \tag{3.4}$$

$$E = \sum_{i=1}^{9} \rho_i h_i - P + \frac{\rho}{2}\left(u^2 + v^2\right) \tag{3.5}$$

$$h_i(T) = \int_{T_0}^{T} C_{pi}(T)\, dT + h_i^{\circ} \tag{3.6}$$

The speed of sound is evaluated by the following equation:

$$c^2 = \frac{\partial P}{\partial \rho} + \sum_{i=1}^{9} \frac{\rho_i}{\rho} \frac{\partial P}{\partial \rho_i} + \frac{\partial P}{\partial E}\left(H - u^2 - v^2\right), \tag{3.7}$$

where $H = (E + P)/\rho$, and partial differential terms become

$$\frac{\partial P}{\partial \rho} = \frac{1}{1 - \sum_{i=1}^{9} \rho_i C_{p,i} \Big/ \sum_{i=1}^{9} \rho_i R_i} \left\{ -\frac{1}{2}\left(u^2 + v^2\right) \right\}, \tag{3.8}$$

$$\frac{\partial P}{\partial \rho_i} = \frac{1}{1 - \sum_{i=1}^{9} \rho_i C_{p,i} \Big/ \sum_{i=1}^{9} \rho_i R_i} \left\{ h_i - \frac{\sum_{i=1}^{9} \rho_i C_{p,i}}{\sum_{i=1}^{9} \rho_i R_i} R_i T \right\}, \tag{3.9}$$

$$\frac{\partial P}{\partial E} = \frac{-1}{1 - \sum_{i=1}^{9} \rho_i C_{p,i} \Big/ \sum_{i=1}^{9} \rho_i R_i}. \tag{3.10}$$

The current study uses the 9-species, 19-reaction mechanism for hydrogen-air combustion listed in Table A.1 (Jachimowski, 1986; Wilson & MacCormack, 1992). The nitrogen reactions are not important at around Mach number 5 so molecular nitrogen is included as an inert species. The third-body efficiencies relative to argon are fixed to the same value as nitrogen. The molecular weight and the thermo-chemical data are replaced for the dependence on the inert gas (refer to Appendix B), and the chemical source terms are explained in Appendix C. The equation of state of ideal gas is adopted in the present study. For the solid and liquid detonations, the revised Kihara-Hikita equation of state (KHT) is often used because of high pressure of the order of GPa (Tanaka, 1985). The C-J velocity and temperature obtained with the KHT equation are 3 % larger than those with the equation for the ideal gas, and the difference of C-J pressure is about 0.05 %. It is confirmed that the differences in C-J properties due to the equation of state are comparatively small. As preliminary simulations of cellular detonations, numerical simulations are performed at previous experimental and numerical conditions and compared with each other in Appendix F.

3.2.2 Initial mixture conditions and computational domains

The algorithm used to solve the equations for compressible fluid dynamics is Yee's non-MUSCL-type TVD upwind explicit scheme (Yee, 1987). The equations are integrated explicitly and the

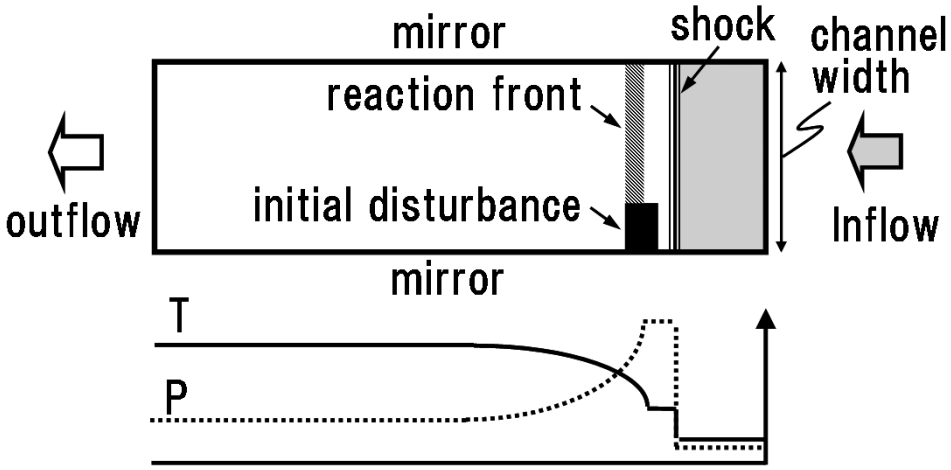

Figure 3.2: Schematic diagram of initial conditions and boundary conditions, for simulations with a detailed chemical reaction mechanism.

chemical reaction source term is treated in a linearly point-implicit manner (Appendix D). The computations are performed with a constant grid resolution of 20.0 and 12.8 computational points/$L_{1/2}$ along the x- and y-axes, respectively. The horizontal x length of the computational domain is adjusted to 40 $L_{1/2}$. First, a 1-D steady C-J solution is calculated with a much finer grid than a 2-D grid, and its solution is put in a 2-D grid (Fig. 3.2). An unburned gas pocket is placed behind the frontal shock to cause the disturbance generating the transverse wave structure. After several thousand time-steps, a series of at least two similar cells is seen and the characteristic cell properties are measured.

The upper and lower boundaries of the computational domain are mirror boundaries, and the detonation stationary coordinate system is utilized. At the inflow boundary, the detonable mixture flows into the computational domain at C-J velocities. At the outflow boundary, the initial values of the 1-D C-J detonation at that position are fixed as the boundary values. The amount of resources at the outflow boundary condition is conserved like those at the inflow boundary condition, so this boundary does not represent a physical rarefaction wave, following the detonation front. The effect of rarefaction waves originating from the outflow boundary is

investigated with the rarefaction wave imposed artificially by extrapolated boundary conditions in the same way as Gamezo *et al*. (1999a). Compared to the solutions without the rarefaction wave, the effect of the rarefaction wave is restricted near the outflow boundary, because the detonation products are compressed twice or three times by transverse waves, and the local Mach number reaches unity before the mixture arrives at the outflow boundary.

3.3 Grid convergence study in two-dimensional detonations

On grid convergence study of numerical simulations, a comparison between 20 points and 40 points in the half-reaction length is performed in the most stiff mixture condition, Case a. Cases b–d do not show remarkable differences, but in the stiffest mixture condition, Case a shows alteration. The results of Case a are summarized in Table 3.2, where n, a, and b are the mode number (the number of transverse waves across the channel), the cell length, and the cell width, respectively. The simulation results with resolution of 20 points/$L_{1/2}$ show good cellular structure, except for the specific channel width ($W = 15.0L_{1/2}$), where the number of transverse waves increases transiently. Although the numbers of transverse waves with a high resolution increased at narrower channels than those at low resolution, the differences in aspect ratios of the cell, a/b, are less than 10 %. The mode numbers of the high resolution increased with narrower channel than those of the low resolution. The differences in aspect ratios of the cell, a/b, are less than 10% or less. Irregularity of cellular structure occurred more firmly in the high-resolution study and often resulted in detonation substructures. The detonation substructures are often observed as a fine structure in the cell marked on soot-foiled records (Gamezo *et al*., 2000). On the other hand, the other mixture conditions, such as a mixture diluted by argon or a mixture diluted by nitrogen mixture at low initial pressure of 0.013 MPa, indicate that there are little difference in cell sizes. A finer grid resolution than 20 points/$L_{1/2}$ seems

Table 3.2: Cellular structures obtained with different grid resolutions of 20 and 40 point / $L_{1/2}$.

$W/L_{1/2}$	n_{20}	n_{40}	a_{20} (mm)	a_{40} (mm)	b_{20} (mm)	b_{40} (mm)	a_{20}/b_{20}	a_{40}/b_{40}	Difference (%)
2.5	1	1	1.52	1.65	0.84	0.84	1.82	1.98	8.08
5.0	1	1	2.70	2.64	1.67	1.67	1.61	1.62	0.62
10.0	1	2	4.96	2.68	3.35	1.67	1.48	1.59	6.92
15.0	2	3	3.75	2.76	2.51	1.67	1.49	1.65	9.70
20.0	1	2	9.30	4.55	6.69	3.35	1.39	1.36	2.21

to be required to resolve the detonation substructure, but the present resolution of 20 points is useful for understanding the general detonation characteristics.

For the correct prediction of the detonation structure, sufficient points are prepared for the half-reaction length. In spite of the recent incredible improvements of CPU speed, it is still time-consuming calculation to simulate the detonation structure with a detailed chemical reaction mechanism. The present simulations with resolution of 20 points/$L_{1/2}$ and compared those to the results with resolution of 40 points/$L_{1/2}$. The previous works by Sharpe & Falle (2000b) and Sharpe (2001b) said that resolution of less than about 20 points/$L_{1/2}$ is too coarse to capture the detonation details in their 2-D simulations. Although resolution of 64 points/$L_{1/2}$ constituted at least a qualitatively very good solution, the results were obtained by a simplified chemical reaction mechanism and their criterion would be applied for their parameter sets. As the results with the detailed chemical reaction mechanism, the work of Oran *et al.* (1998) is well known. In the hydrogen-oxygen-argon mixture, the computations are performed with resolution of 12 points/$L_{1/2}$, so the present simulations are performed with higher resolution.

3.4 Transverse Wave Contribution to Detonation Propagation

3.4.1 Transverse wave strength and flow features

By using total computations in Cases a–d, the relationship between the channel widths normalized by half-reaction lengths and the transverse wave strengths are shown in Fig. 3.3. The transverse wave strengths $S(= P_3/P_1 - 1)$ are derived from pressure distributions immediately before transverse wave collisions, specifying post-shock pressures P_1 and P_3. As the normalized channel width increases, the transverse wave strength increases. The maximum channel width W_{max} where a single transverse wave appears is detected with increasing the channel width. When another transverse wave appears, the transverse wave strength decreases. Hence, the transverse wave strength becomes maximum in the maximum channel width W_{max}.

Flow features immediately before the transverse wave collisions are categorized into two evolutionary stages of transverse wave structures: (b) double Mach reflection, and (c) complex Mach reflection (Fig. 3.1). The observed flow features and numbers of transverse waves across the channel n are listed in Table 3.3. In Case a, the transverse wave strength increases continuously with channel width, while the flow features change suddenly across the transverse wave strength of 0.85. When the transverse wave strength is greater than 0.85, the complex Mach reflection appears at the final stage of the cell (marginal behavior). When the transverse wave strength is less than 0.85, the transverse wave structure develops until the double Mach reflection (ordinary behavior). Cases b and c show the same trend in transverse wave strength with channel width and the flow feature shows good agreement. Although the complex Mach reflection is observed in Cases b and c, the transverse wave strengths cannot reach the marginal value of 1.5 but increase up to 0.85. In Case d, the transverse wave strength

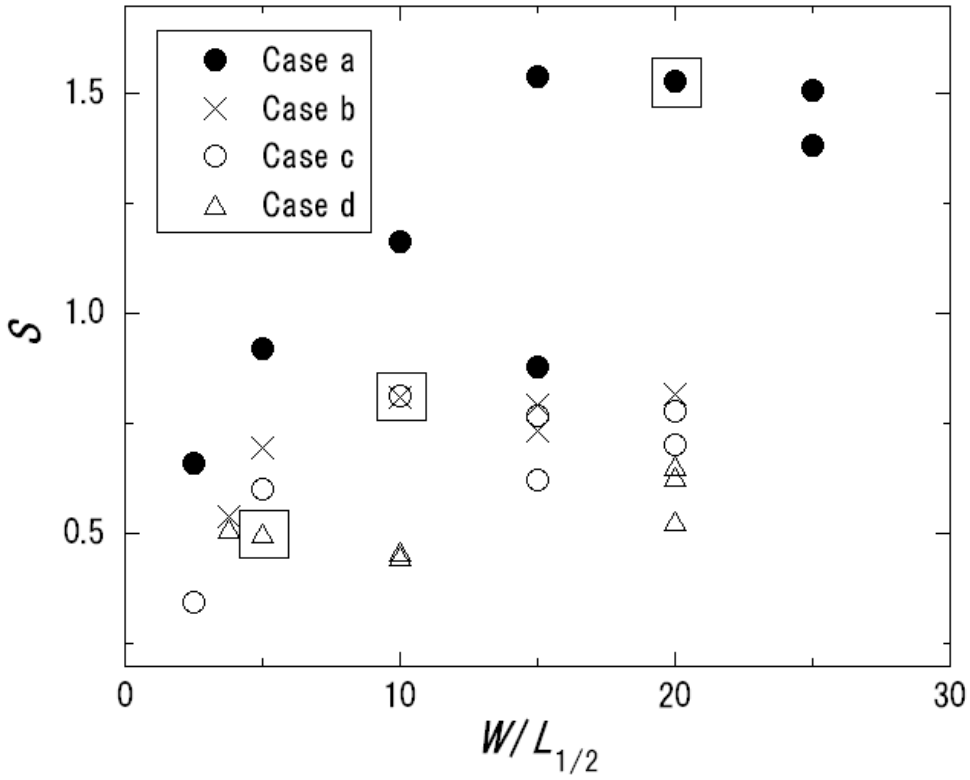

Figure 3.3: Channel width $W/L_{1/2}$ vs transverse wave strength S (□: W_{max}, the maximum channel width in which a single transverse wave appears).

Table 3.3: The numbers of transverse waves across the channel n and the transverse structures at the final stage of the cell. (b), Double Mach reflection; (c), Complex Mach reflection; _, W_{max}; n, the number of transverse waves across a channel (mode number).

Case	$W/L_{1/2}$	2.5	3.75	5.0	10.0	15.0	20.0	25.0
a	n	1	-	1	1	2	1	2
	structure	(b)	-	(c)	(c)	(c)	(c)	(c)
b	n	1	-	1	1	2	2	-
	structure	(b)	-	(b)	(c)	(c)	(c)	-
c	n	-	1	1	1	2	2	-
	structure	-	(b)	(b)	(c)	(c)	(c)	-
d	n	-	1	1	2	2	3	-
	structure	-	(b)	(b)	(b)	(b)	(b)	-

is constant at about 0.5, corresponding to the ordinary detonation, and the the flow feature reproduces the ordinary behavior for all channel widths.

It is known that the number of transverse waves across the channel indicates the dependence as a function of initial pressure (Fickett & Davis, 1979). There is the pressure range over which the particular number of transverse waves is observed in a fixed channel width. Over a few narrow pressure ranges, different numbers of transverse waves may be obtained in a given system. In the present simulations, the same tendency is observed in the dependence of the channel width. For simplicity, most of the explanations are restricted within the channel where a single transverse wave appears. Previous experiments (Strehlow & Biller, 1969) indicate that the transverse wave strength is relatively independent of initial pressure and the chemical system. Compared to the experimental results (ordinary detonation: $S = 0.5$; marginal detonation:

$S = 1.5$), either the marginal or the ordinary detonation seems to appear, depending on the channel width. All the lowest incident shock speeds immediately before the transverse wave collisions of Cases a–d in the maximum channel W_{max} are delayed by approximately 300 m/s from the C-J velocity. These conditions are thought to be in the most marginal conditions, while the lowest incident shock velocity is equal to 0.83 D_{CJ}. According to previous experiments, Fickett & Davis (1979) stated that the variation of the instantaneous shock speed through the detonation cell is $1.2 \sim 0.85 D_{CJ}$ for ordinary detonation, and $1.4 \sim 0.7 D_{CJ}$ for marginal detonation. Viewed in this light, all detonations observed here are classified as ordinary detonations, and Case a has notably marginal behavior as the mixture characteristics.

In a narrow channel of $2.5 \sim 3.75 L_{1/2}$, flow features of all cases demonstrate the ordinary behavior; the transverse wave structure evolves from the single Mach reflection to the double Mach reflection. Figure 3.4 shows the typical ordinary behavior of Case a for a channel width of 2.5 $L_{1/2}$ ($W = 0.42$ mm). Figure 3.4 is drawn as the detonation history in the form of the gray-scale distribution of the maximum pressure P_{max}, reaching at each point in space. Darker colors indicate higher pressure regions. All the maximum pressure histories in this paper are reproduced twice in the y direction by taking advantage of the mirror boundary conditions. In such a reproduced form, it is easy to understand the cell structures in our restricted channel width, where only one transverse wave appears. The cell aspect ratio is 2.0 and the maximum pressure trajectories of the triple points are straight and pale. There are two kinds of tracks at high pressures. On the centerline of a cell, there is the horizontal track 1 caused by a collision with two transverse waves. The vertical tracks 2 appear due to explosions of the mixture ignited by the compressions of transverse waves.

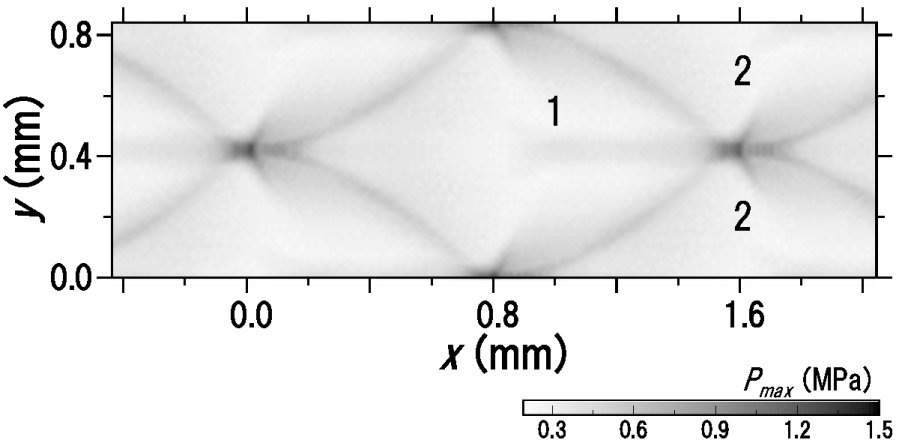

Figure 3.4: Detonation history presented by maximum pressure distribution P_{max}: Case a - N_2, 0.101 MPa; $W = 2.5L_{1/2}$, $b = 0.84$ mm, $a/b = 1.8$. (1: Horizontal track, 2: Vertical track).

3.4.2 Comparison of cellular structures and transverse waves in the characteristic channel width

In the maximum channel width W_{max}, numerical cell properties, such as cell widths in Table 3.4, are compared to previous experimental results (Strehlow & Engel, 1969; Bull *et al.*, 1982; Stamps & Tieszen, 1991). The cell widths $b(= 2W_{max})$ are derived from duplication of W_{max}. According to the agreement between numerical and experimental cell properties, it is reasonable to consider that the cell properties in W_{max} represent the mixture characteristics.

Figures 3.5 show the detonation histories presented the maximum pressure distributions for W_{max}. Figure 3.5(a) is the maximum pressure distributions of Case a for the normalized channel width $W_{max} = 20L_{1/2}$. In Case a, the strong transverse detonation ($S = 1.5$) causes the high-pressure regions and the aspect ratio becomes 1.4. The transverse detonation in Cases b and c is not so strong that the transverse wave strength indicates the intermediate value of 0.8. Figures 3.5(b) and (c) show the maximum pressure distributions for Cases b and c for $W_{max} = 10L_{1/2}$. Although the high-pressure region created by the transverse detonation in Case b is clearer and the curvature of the frontal triple point trace is slightly larger than that of Case

Table 3.4: Numerical cell width and aspect ratio in the maximum channel width W_{max} and previous experimental results ([†]Strehlow & Engel, 1969; [‡]Bull *et al*., 1982).

Case	Numerical Simulation			Experiments	
	$Wmax/L_{1/2}$	b (mm)	a/b	b (mm)	a/b
a	20.	6.7	1.39	8.0[‡]	1.4[‡]
b	10.	24	1.67	25[‡]	1.8[‡]
c	10.	0.83	1.83	1.0, extrapolated[†]	–
d	5.0	4.0	2.01	6.0[†]	–

c, both outlines of the cells show relatively a good similarity. The aspect ratios of Cases b and c are 1.7 and 1.8, respectively. The similarity in Cases b and c implies that cellular structures in these different initial conditions are well balanced and comparable in shape. The transverse wave strength in Case d is almost constant at around 0.5, corresponding to the ordinary detonation. Figure 3.5(d) shows the maximum pressure history for $W_{max} = 5.0L_{1/2}$. The cellular structure after the transverse wave collision is vague and the aspect ratio of the cell equals 2.0. The aspect ratios of the cell are bound up with the velocity of transverse waves, so the transverse wave velocity relative to detonation front changes with aspect ratio.

Figures 3.6 shows the instantaneous pressure contours close to the shock front just before the transverse wave collisions. Figures 3.6(a-c) show the complex Mach reflections, and Fig. 3.6(d) shows the double Mach reflection. In Case a, the transverse detonation TD precedes the transverse shock TS extending from the end of the transverse detonation. This prior detonation strongly overdrives the whole transverse wave and clearly makes the transverse shock. However, the transverse detonation TD in Cases b and c follows the transverse shock TS. In Case d, the pressure jump across the triple point TP does not have a difference in strength

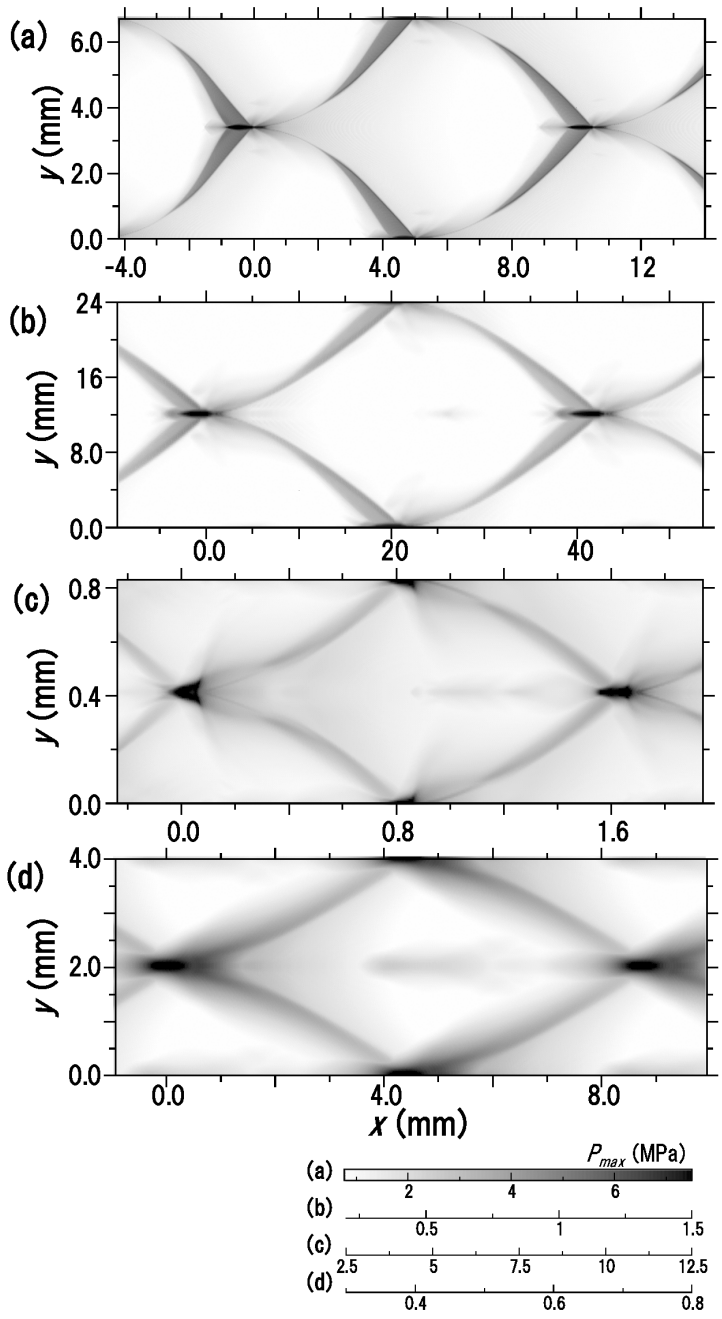

Figure 3.5: Detonation histories presented by maximum pressure distribution P_{max}: (a) Case a – N_2, 0.101 MPa, $W = 20.0L_{1/2}, b = 6.7$ mm, $a/b = 1.4$. (b) Case b – N_2, 0.0131 MPa, $W = 10L_{1/2}, b = 24$ mm, $a/b = 1.7$. (c) Case c – Ar, 0.101 MPa, $W = 20L_{1/2}, b = 0.83$ mm, $a/b = 1.8$. (d) Case d – Ar, 0.013 MPa, $W = 5.0L_{1/2}, b = 4.0$ mm, $a/b = 2.0$.

across the transverse shock TS. Owing to the occurrence of the strong transverse detonation in Case a, the transverse wave is strongly overdriven and the aspect ratio decreases up to 1.4. The potential existence of a cell with large normalized channel width $W_{max}/L_{1/2}$ permits flexibility in changing cell sizes.

3.4.3 Second limit criterion

In §3.4.3, one of the factors in the occurrence of the strong transverse detonation in Case a (§3.4.2) would be discussed. Post-shock pressure and temperature profiles of Cases a–d on the centerline of the cell are presented in Figs. 3.7. Post-shock conditions regularly oscillate because of the fluctuation of the frontal shock. In these figures, the lowest pressure and temperature are the conditions behind the incident shock just before the transverse wave collisions. According to the experiment of Voevodsky & Soloukhin (1965), the second limit at high temperature (> 700 K) and high pressure far from the third limit signifies not the extinction but the mild ignition. In the present study, the second explosion limit is expressed by the relation $2k_2 = [M]k_9$; the rate of constants are listed in Table A.1, and the line of the explosion limit determined by the constants well agrees with Voevodsky's limit. The lowest post-shock pressure and temperature are searched from Fig. 3.7 and are plotted on Fig. 3.8 as a $P - T$ diagram. In the figure, calculated second explosion limit and the C-J conditions for each case are also presented. The post-shock condition of Case a goes over the second explosion limit, but the post-shock conditions of the other three cases do not intersect the second limit. In the work of Takai *et al*. (1974), the lowest post-shock in the mixtures diluted with argon and nitrogen decrease across the second limit, because their lowest conditions are not experimentally measured but determined just to be the post-shock conditions behind the shock propagating at $0.8D_{CJ}$. Figure 3.8 clearly shows the difference between nitrogen and argon diluents, and confirms that the strong transverse detonation in Case will have a close relation to the second limit. Further-

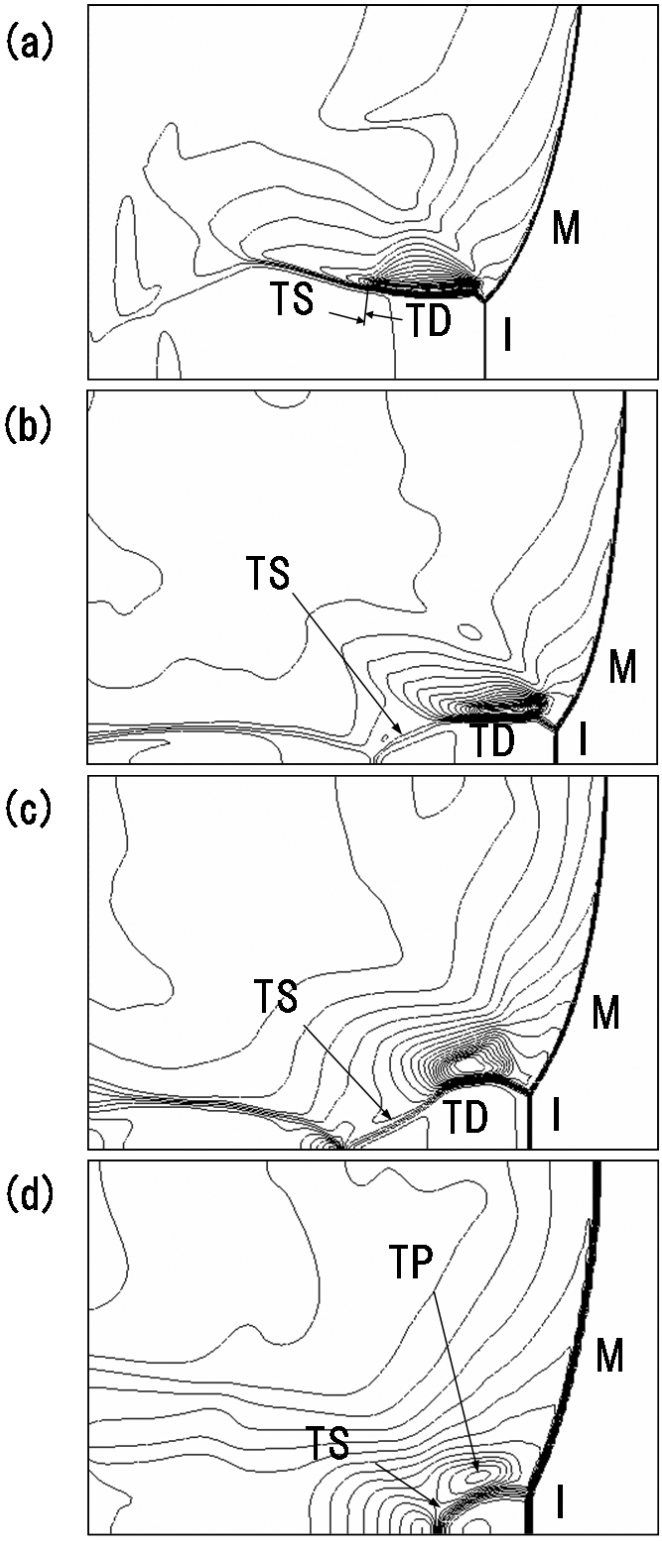

Figure 3.6: Instantaneous pressure contours before transverse wave collisions: (a) Case a – N_2, 0.101 MPa, $W = 20.0L_{1/2}$. (b) Case b – N_2, 0.013 MPa, $W = 10.0L_{1/2}$. (c) Case c - Ar, 0.101 MPa, $W = 10.0L_{1/2}$. (d) Case d – Ar, 0.013 MPa, $W = 5.0L_{1/2}$. (M: Mach stem, I: Incident shock, TD: Transverse Detonation, TP: Triple Point, TS: Transverse Shock)

more, the transverse wave strength of Case a indicates 1.5 that is experimentally measured in the marginal detonation. A new type of marginal detonations that is found to be different from spin detonations by Strhelow & Crooker (1974) are observed in almost hydrogen fuel mixture. The second explosion limit is inherent in hydrogen fuel, so it might have a deep connection with the occurrence of the marginal detonation.

The weakest incident shock speeds, D_{min}, just before the transverse wave collisions of Cases a–d are measured and listed in Table 3.5. The lowest propagation velocity D_{min} is approximately 300 m/s slower than D_{CJ} in all cases, and thus $D_{min} \approx 0.83 D_{CJ}$. It is experimentally known that the variation of the instantaneous shock speed through the detonation cell is $1.2 \sim 0.85 D_{CJ}$ for an ordinary detonation, and $1.4 \sim 0.7 D_{CJ}$ for a marginal detonation. The marginal detonation usually appears near the detonation limit, and four cases are far from the limit. Viewed in this light, all detonations discussed here are classified into ordinary detonations, and the difference in propagation properties is due to the nature of various mixture conditions. When the post-shock condition decreases across the second limit, the induction length rapidly increases. In Case a, The half-reaction length $L_{1/2}$ behind the shock propagating at D_{min} is 81.3 mm and is approximately 500-times longer than $L_{1/2}$(=0.167 mm) at D_{CJ}. Without contribution of transverse waves, the detonation could not propagate, especially in Case a. In the following section, transverse wave properties are fully examined to discuss the contribution of transverse waves to detonation propagation.

3.4.4 Acoustic coupling criterion

In Case a, a transverse wave well develops into the strong transverse detonation. In §3.4.4, a detailed behavior of transverse waves would be discuss, because it plays an important role in the detonation propagation, especially in Case a. The loci of triple points are depicted on $x - y$ diagram, Fig. 3.9, by searching frontal triple points from the maximum pressure histories (Fig.

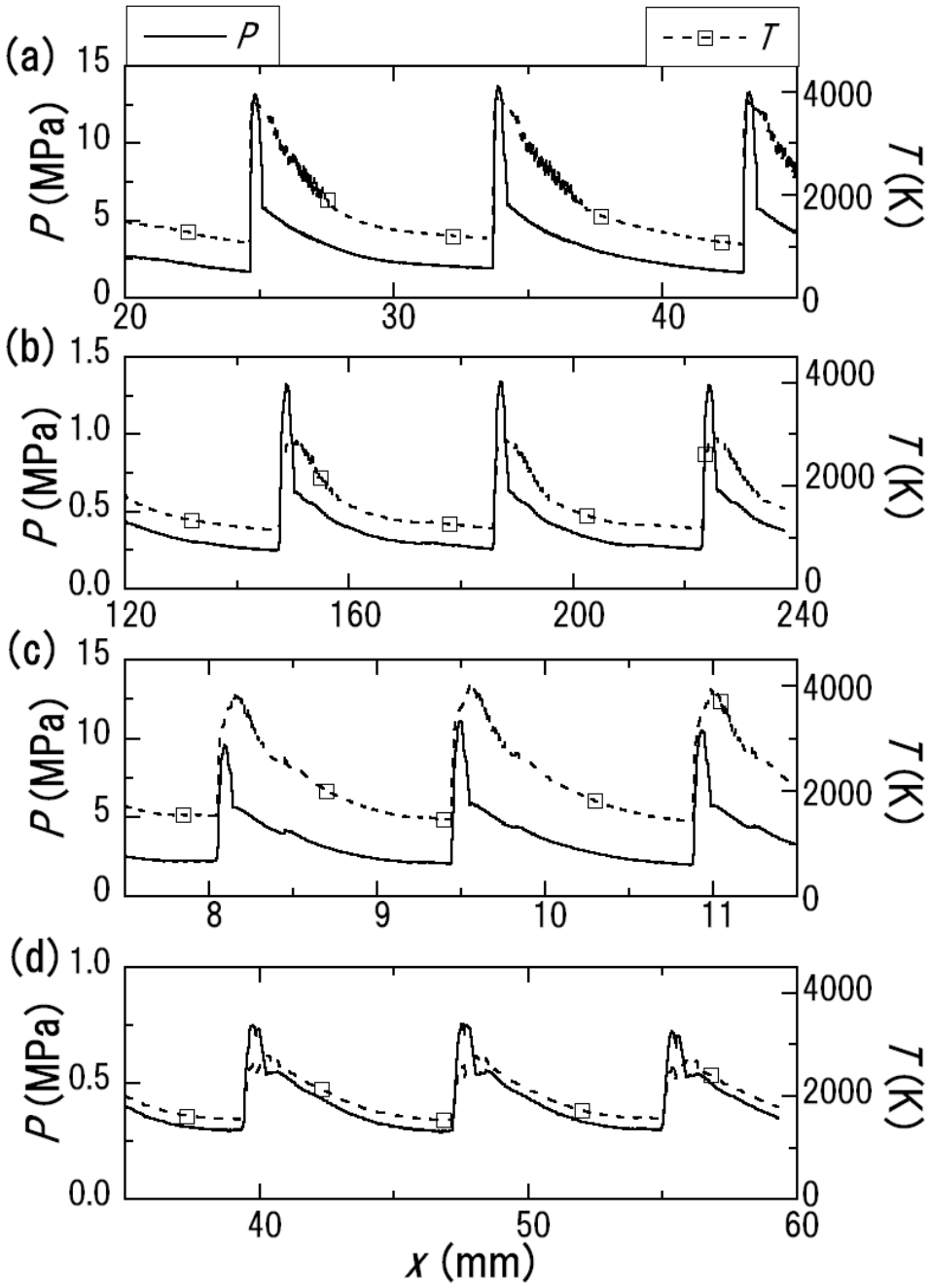

Figure 3.7: Centerline pressure and temperature profiles, for 2-D detonations in W_{max}: (a) Case a – N_2, 0.101 MPa, $W = 20.0L_{1/2}$. (b) Case b – N_2, 0.013 MPa, $W = 10.0L_{1/2}$. (c) Case c - Ar, 0.101 MPa, $W = 10.0L_{1/2}$. (d) Case d – Ar, 0.013 MPa, $W = 5.0L_{1/2}$.

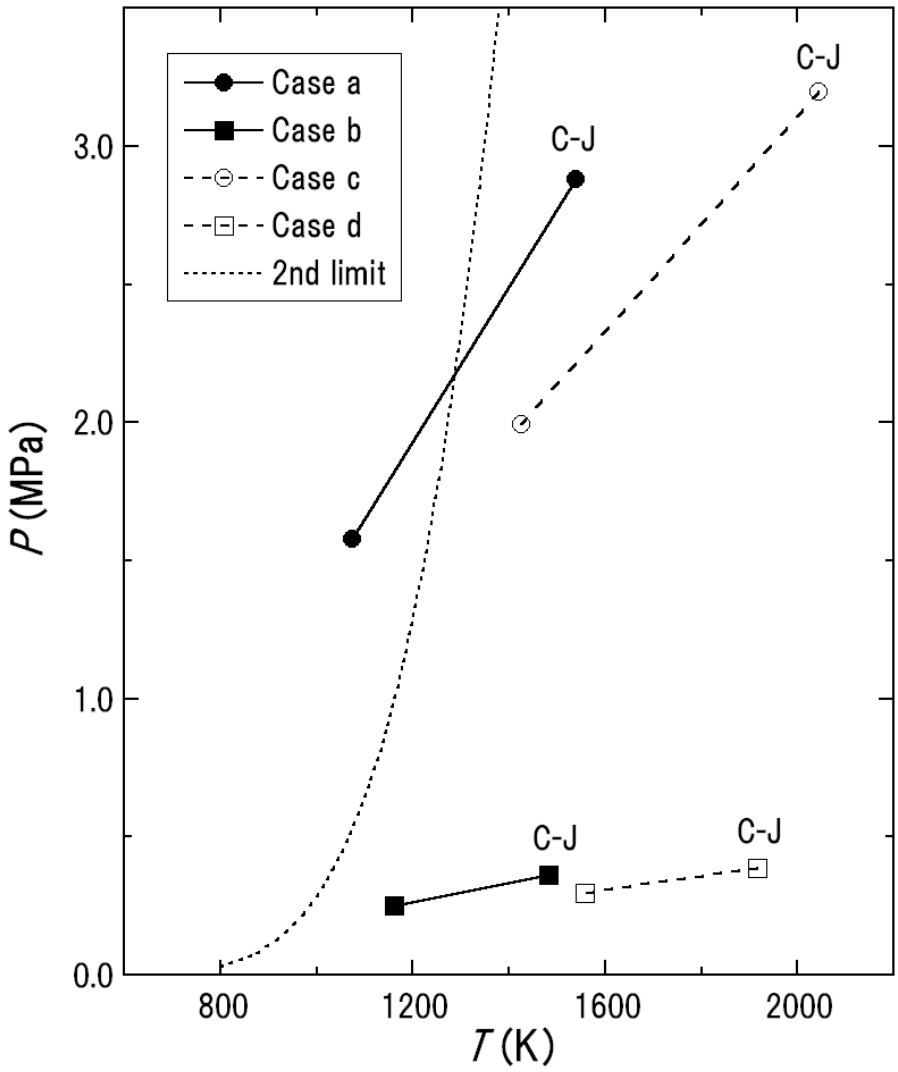

Figure 3.8: $P - T$ diagram of post-shock conditions with the second explosion limit line; the lowest conditions & C-J conditions.

Table 3.5: The C-J velocity D_{CJ} & the lowest frontal velocity $D_{min}$of the incident shock velocity just before the transverse wave collision.

Case	a	b	c	d
D_{CJ} (m/s)	1979.5	1931.7	1862.1	1790.6
D_{min} (m/s)	1649.5	1609.7	1551.7	1492.1

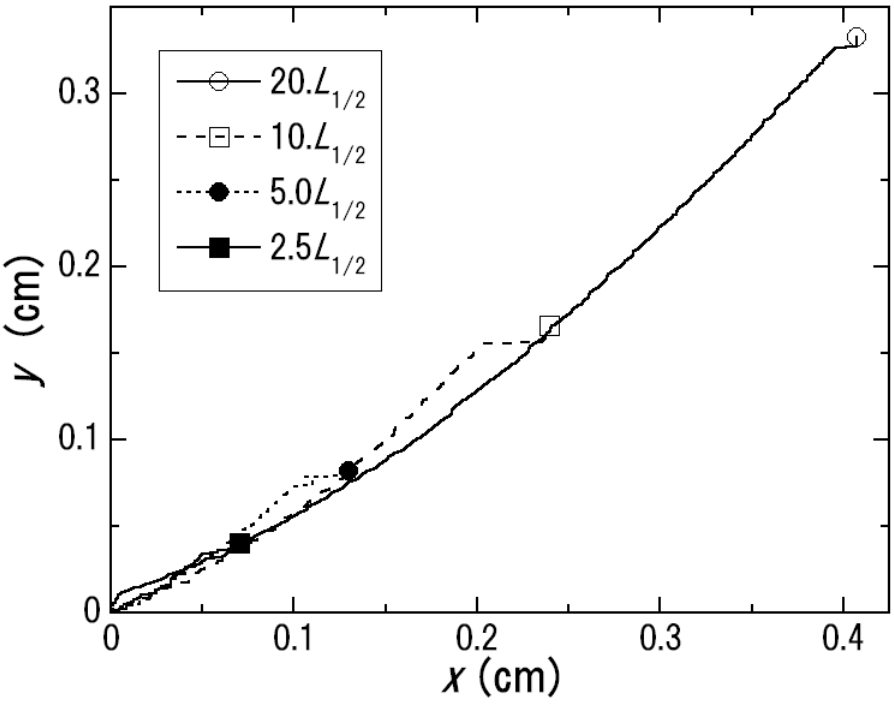

Figure 3.9: $x - y$ diagram of loci of frontal triple points in Case a – N_2, 0.101MPa, with various channel widths. Each of the plots indicates the end point of locus.

3.5). The loci start at the point distinguished as the separating point of two transverse waves, and end at the next starting point. Although the slopes of the traces become gentle as the channel width increases, the end points of all traces exist on the trace of the channel width 20.0 $L_{1/2}$. This is because the traces for narrow channels, 2.5, 5.0, and 10.0 $L_{1/2}$, suddenly move forward at the transverse wave collisions; the mechanism on the jump of the traces is discussed in §2.4.3. Since all end of traces finally exist on the trace with $W = 20.0L_{1/2}$, it is possible to derive the average velocity of a transverse wave as a function of the channel width, just examining the traces with $W = 20.0L_{1/2}$ as a representation of all different channels. As a function of x in Fig. 3.9, all of the transverse wave properties in narrower channel such as 2.5, 5.0, 10.0 $L_{1/2}$ can be evaluated: $y = f(x)$, where $f(x)$ is the triple point locus as drawn in Fig. 3.9.

Figure 3.10 shows instantaneous shock velocities as a function of the distance from the starting point of the cell to the half-cell length along the direction x in Case a with W_{max} =

$20.0L_{1/2}$. The Mach stem velocity (dashed line) and the incident shock velocity (dotted line) are determined directly from the simulation. The transverse wave velocity U_T along the direction y is illustrated by the solid line, and is derived from the following equation:

$$U_T = \frac{\mathrm{d}y}{\mathrm{d}t} = \frac{\mathrm{d}y}{\mathrm{d}x} \cdot \frac{\mathrm{d}x}{\mathrm{d}t} = f'(x) \cdot \frac{U_M + U_I}{2}, \tag{3.11}$$

where $f(x)$ is determined by searching the trajectory of the frontal triple points in Fig. 3.5(a). Note that the transverse wave velocity along the direction x is an approximate speed, and it is close to the Mach stem speed in the begining, and becomes getting closer to the incident shock wave speed. The instantaneous transverse wave velocity increases up to near the C-J velocity (1979.5 m/s; dashed and single-dotted line) as the transverse wave propagates in this evaluation method. Since the instantaneous velocity of the transverse wave U_T rises as it propagates, the average transverse velocity $\bar{U}_T$ increases with channel width. In a narrow channel width of $2.5L_{1/2}$ (Fig. 3.4), the flow feature shows the ordinary behavior. Judging from the velocity profile, the marginal behavior occurs preferentially in the wide channel where the transverse wave propagates at high average velocity.

To inspect the validity of acoustic coupling, the mean transverse wave velocities $\bar{U}_T$ for different channel widths in Case a and for W_{max} in Cases b-d are detected from the aspect ratio of the cell a/b and the C-J velocity D_{CJ} ($\bar{U}_T = D_{CJ}b/a$). Table 3.6 summarizes the ratio of $\bar{U}_T$ to the speed of sound in the detonation products at C-J state c_{CJ}. In Case a, the normalized transverse wave velocity $\bar{U}_T/c_{CJ}$ increases from 0.9 to 1.3 with increasing channel width and shows the largest value of 1.3 for W_{max}. In Cases b–d, the normalized transverse wave velocity is about unity. It is clear that the marginal behavior occurs preferentially at larger values of $\bar{U}_T/c_{CJ}$ than unity and does not satisfy the acoustic coupling criterion ($\bar{U}_T/c_{CJ} = 1.0$). These results lead us to conclude that the irregularity of the mixture diluted with nitrogen at high initial pressure has two causes: the flexibility of the cell width due to the occurrence of the

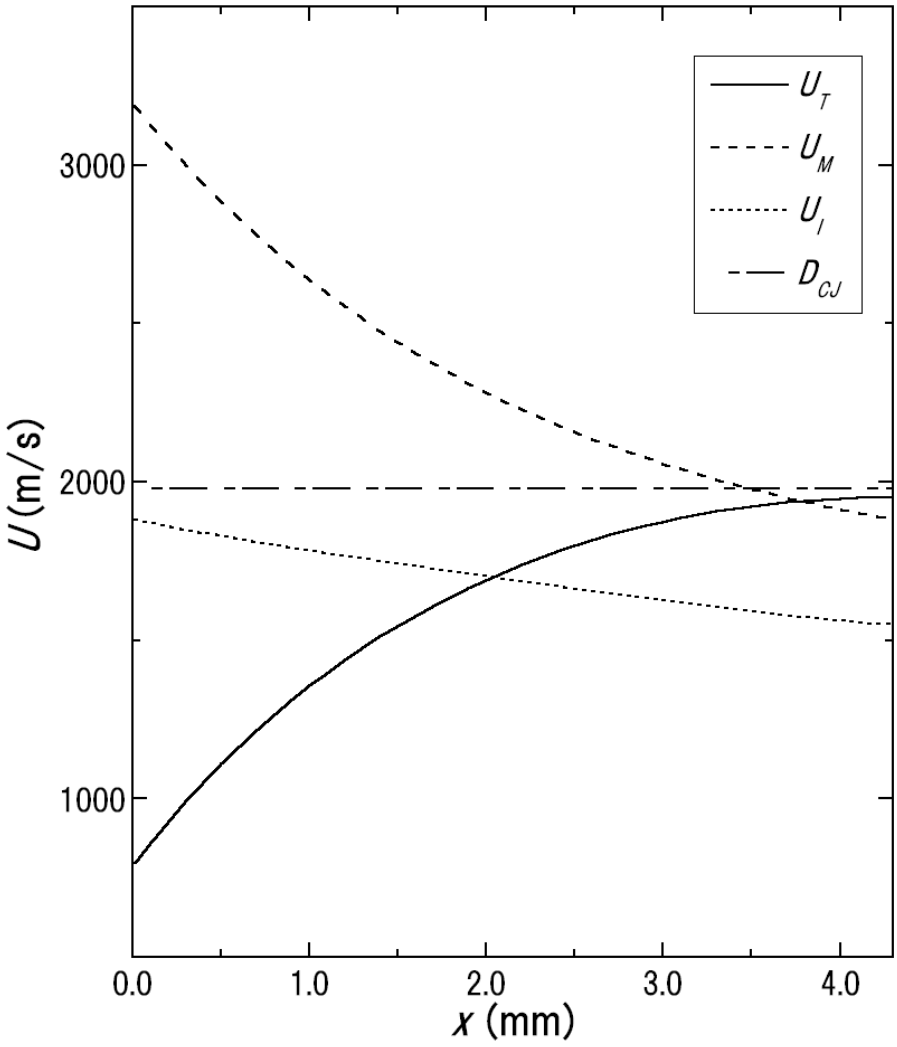

Figure 3.10: Velocity variations through a cell in Case a – N_2, 0.101MPa. (U_M, Mach stem velocity, dashed line; U_I, Incident shock velocity, dotted line; U_T, Transverse wave velocity, solid line; D_{CJ}, C-J velocity, dashed and single-dotted line.)

strong detonation, and instability due to out-of-phase acoustic coupling.

Table 3.6: Average transverse wave properties. (a/b, aspect ratio of a cell; $\bar{U}_T$, average velocity of a transverse wave; c_{CJ}, sound speed at the C-J condition; c_1, post-shock sound speed; M_T, post-shock Mach number of a transverse wave; I_{tw}, transverse wave intensity.)

	Case	a/b	$\bar{U}_T$ (m/s)	c_{CJ} (m/s)	c_1 (m/s)	$\bar{U}_T/c_{CJ}$	$\bar{M}_T(=\bar{U}_T/c_1)$	S	I_{tw}
a	$W = 2.5L_{1/2}$	1.89	1047	1098	897.9	0.95	1.17	0.66	7.62
	$W = 5.0L_{1/2}$	1.78	1112	↓	↓	1.01	1.24	0.92	15.2
	$W = 10.0L_{1/2}$	1.48	1337	↓	↓	1.22	1.49	1.12	30.5
	$W = 20.0L_{1/2}$	1.39	1434	↓	↓	1.31	1.59	1.53	60.9
b	$W = 10.0L_{1/2}$	1.67	1154	1065	882.2	1.08	1.31	0.81	9.43
c	$W = 10.0L_{1/2}$	1.83	1015	1033	941.5	0.98	1.08	0.81	11.4
d	$W = 5.0L_{1/2}$	2.01	891	986	912.9	0.90	0.98	0.50	4.70

3.4.5 Transverse wave intensity

The question arises what makes these transverse wave structures different. It must be notice that characteristic inclinations of a temperature profile of 1-D steady C-J detonation are fairly close to each other and show the same transverse behaviors. As the inclination of the temperature profile rises, the marginal behavior tends to become stronger, and effective activation energy in the overall reaction also increases. The propagation of the unstable detonation is caused by high activation energy, and the marginal behavior has a connection with the unstable propagation. To evaluate transverse waves, the transverse wave intensity I_{tw} is proposed, following previous unsteady flows around the blunt body projectile propagating through combustible mixtures (Matsuo & Fujii, 1998):

$$I_{tw} = t_f / t_c = (W/c_1)/[T_1/|dT/dt|_{max}], \tag{3.12}$$

where t_f, t_c, W, c_1, T_1, and $|dT/dt|_{max}$ are a characteristic fluid time, a characteristic chemical time, a channel width, a post-shock sound speed, a post-shock temperature, the maximum value of the temperature increase per unit time, respectively. The $|dT/dt|_{max}$ is easily derived from the time integration of the species equations under the constant-volume reactions. In this definition, the transverse wave intensity is estimated by the strength of a compression wave originating from the reaction front. The intensity rises as the channel width become wider, which accompanied by the transition of the transverse wave behavior from ordinary to marginal. In Fig. 3.11, the relation between the cell aspect ratios and the transverse wave intensities are shown. Since the reaction is promoted by an exponential function of temperature, the horizontal axis is given in the logarithmic form. With the transverse wave intensity, it is possible to expect the approximate cell-aspect ratios in a certain channel width. It is inferred that the transverse wave structure in Case c (10 $L_{1/2}$) corresponds to that in Case a (3.75 $L_{1/2}$).

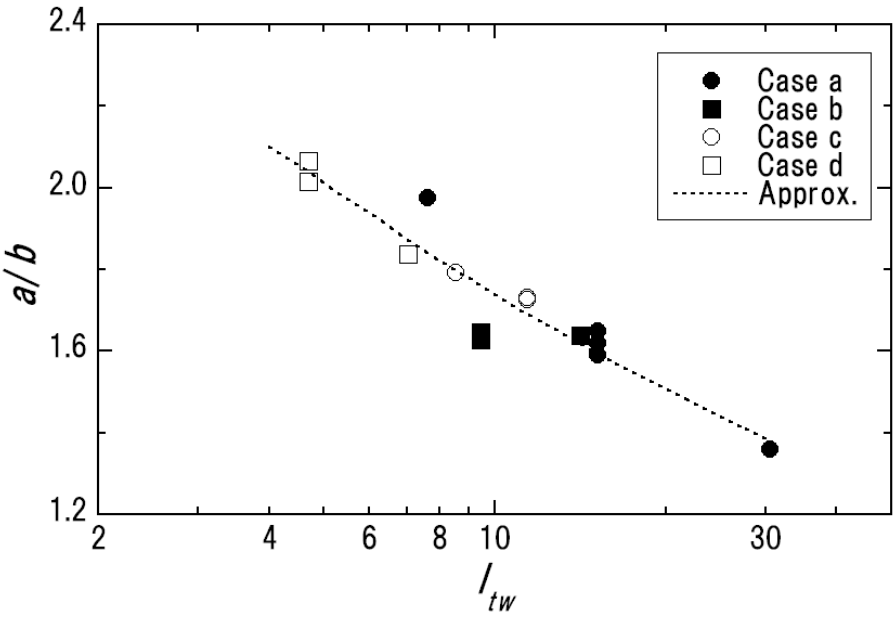

Figure 3.11: Relation between cell aspect ratios a/b and transverse wave intensity I_{tw}. The data with grids of 40 points / $L_{1/2}$ are plotted.

3.5 Summary

Two-dimensional computations of a stoichiometric hydrogen-oxygen detonation diluted with nitrogen or argon mixture were performed using a detailed chemical reaction mechanism. The transverse wave strength was defined as the dimensionless pressure increase across the reflected shock at the triple point; the maximum channel width where a single transverse wave appeared was examined for different channel widths. The transverse wave strength increased as a function of the channel width until the maximum channel width. When a detonation propagated through a narrow channel (2.5–3.75 times larger than the half-reaction length), the shock structure showed the ordinary behavior—the single and double Mach reflections. In a mixture diluted with nitrogen at an initial pressure of 0.101 MPa, the transverse wave strength increased up to 1.5 with increasing channel width, and the flow feature showed the marginal behavior—the single, double, and complex Mach reflections. In both the hydrogen-air mixture at 0.013 MPa, and

the hydrogen-oxygen mixture diluted with argon at 0.101 MPa, although the transverse wave strength did not increase beyond 0.85, the flow features showed the complex Mach reflection. In a hydrogen-oxygen-argon mixture at 0.013 MPa, the transverse wave evolved up to the double Mach reflection, and the flow feature showed the ordinary behavior with transverse wave strength of 0.5.

At the maximum channel width, the cell widths and aspect ratios showed comparatively good agreement with previous experimental data. The cell width normalized by the half-reaction length for the mixture diluted with nitrogen at 0.101 MPa was more than twice the size for the other mixture conditions. Based on the acoustic coupling, the mean transverse wave velocities were specified from the aspect ratio of the cell and the C-J velocity. The ratio of the mean transverse wave velocity to the sound speed at C-J state varied from unity to 1.3 (mixture diluted with nitrogen at 0.101 MPa) at the maximum channel width. The strong transverse detonation occurred preferentially in the wide channel where the transverse wave propagated at high mean velocity. Moreover, when the post-shock conditions varied across the second explosion limit, strong transverse detonations appear in the flow fields. These results lead us to conclude that the empirical irregularity of the cell for the mixture diluted by nitrogen at 0.101 MPa was caused by the flexibility of the cell width due to the occurrence of the strong detonation, and the instability due to out-of-phase acoustic coupling. To evaluate transverse wave properties, the transverse wave intensity was proposed, and suggested the possibility how to predict transverse wave behavior in a certain channel width.

Chapter 4

Soot Track Generation in Mach Reflection and Detonation

4.1 Previous Speculations on Soot Track Formations

For over 40 years, the soot track method has been widely applied to observe detonations, and it is readily apparent that the soot tracks are associated with the transverse waves and triple points that move along the main shock front. Mach speculated that the Mach stem was of greater strength than the incident shock by the fact that the soot inside the Mach stem funnel was compressed more than outside and blown off the plate. Krehl & Geest (1991) proposed that soot tracks were caused by scrubbing the soot off by vortices generating around slip lines. On the other hand, Terao & Azumatei (1989) suggested that soot tracks in detonation waves are formed by combustion of the soot in hot oxidizing atmospheres behind the shock waves. However, the precise physical mechanism that creates the soot tracks has never been clearly demonstrated, and it is not known what features of the triple point structure represent the soot tracks.

The removal of fine soot particles from a surface has not been well clarified, but it has wide applications for industry, the conservation of works of art and historic buildings, contaminant detection, and so on. Many studies of particle entrainment by fluid flows have appeared in the literature (Smedley *et al*., 1999; Otani *et al*., 1993; Suzuki *et al*., 1995). These can be classified as steady flow methods or unsteady flow methods. Steady methods include fully developed turbulent flow in a boundary layer, a pipe, or a jet. Unsteady methods include

pulsed jets, vibrating jets, and shock waves. The most extreme unsteady flow is the shock wave. As a shock wave travels at supersonic speed across a surface, it impulsively accelerates the gas as it passes, creating a high-speed flow behind the shock wave. When the shock wave is advancing into a quiescent gas, a boundary layer forms on the surface and grows with distance behind the shock. Thus, surface-bound particles are exposed to the highest shear forces immediately behind the shock where the boundary layer is thinnest. In this way, a shock wave of sufficient strength is able to remove even tightly bound particles from the surface. Studies of drag on a spherical particle subject to an impulsively started flow behind a shock wave (Igra & Takayama, 1993), and detachment of a single 400 μm diameter particle from the wall of a shock tube (Suzuki *et al*., 1995) revealed that the drag coefficient was nearly twice that in an equivalent steady flow.

The purpose of this chapter is to explore the explanation that is based on the classical fluid mechanics of near-wall flow in viscous gas. We focus on the role of shear stress in transporting soot along the surface, and propose that soot tracks depend largely on variations in the direction and magnitude of the shear stress created by the boundary layer adjacent to a soot foil. Our proposal is motivated by the fact that pattern formation in oil flow visualization is explained in terms of surface shear stress variations by Tanner & Blows (1976). For validation of our hypothesis, we first perform experiments to determine whether soot tracks can be formed in Mach reflection of a non-reactive shock wave. The process of Mach reflection in air contains all the essential features of the interactions between transverse waves and main shocks in detonation fronts. Numerical simulations of shock wave reflections over a wedge are also performed with 3-D compressible Navier-Stokes equations in order to predict the shear stress that will be produced on a soot foil. The motions of soot layers are simulated by treating soot as fluid parcel (Eulerian approach) and discrete families of soot particles (Lagrangian approach), assuming that shear stress due to viscous gas drives soot, but soot thickness does not affect

gas phase. Soot tracks obtained in numerical simulations are compared with Mach reflection experiments, and numerical results are used to interpret the effect of shear stress spatial and temporal variations on soot redistributions. Soot tracks obtained in detonation experiments are also compared with numerical results and explained with the same mechanism for soot tracks in Mach reflection experiments.

4.2 Soot Track Formations in Mach Reflection Experiments

4.2.1 Experimental apparatus and conditions

The shock tube consists of a driver section and a driven section. The driven section is 152 mm diameter and 11.3 m long, while the driver section is 165 mm diameter and 6.2 m long. The driver section is filled with nitrogen, and the driven section is filled with air. To achieve the desired test Mach numbers M_S, the initial test section pressure P_T, the initial driven section pressure P_D, and the diaphragm were varied according to Table 4.1. Figure 4.1 displays a schematic diagram of the test section where an incident shock interacts with a wedge. For soot foils, exchangeable flat sheets of 3003 aluminum alloy, $241 \times 114 \times 1.0$ mm were prepared. The soot foils are held by two "cookie cutters," $279 \times 114 \times 13$ mm, with very sharp leading edges, to record the shock interaction phenomena. The cookie cutters are attached to a wedge such that the soot foils are directly in contact with either side of the wedge. In the present study, right angle wedges 89 mm wide and 51 mm high with apex angles θ_w of 15° and 25° were used.

To cover the aluminum foil sheets with soot, they are hung at the top of a chimney and covered with a lid. At the bottom of the chimney a piece of cotton rag soaked in waste liquid fuel is burned. For Mach 1.9 shots, some low viscosity fluid (Dow Corning 200 fluid – 20×10^{-3} Pa s) is slightly rubbed onto the exposed side of the foil prior to adding the soot. The added viscosity helps the soot to adhere to the surface and prevents the soot from being

Table 4.1: Experimental conditions, for soot track formations in Mach reflections.

case	M_S	θ_w (°)	P_T (kPa)	P_D (kPa)	Diaphragm (mm)	Viscosity fluid
1	1.9	15	10	280	0.300	on
2	1.9	25	10	280	0.300	on
3	1.2	15	98.6	170	0.076	off
4	1.2	25	98.6	170	0.076	off

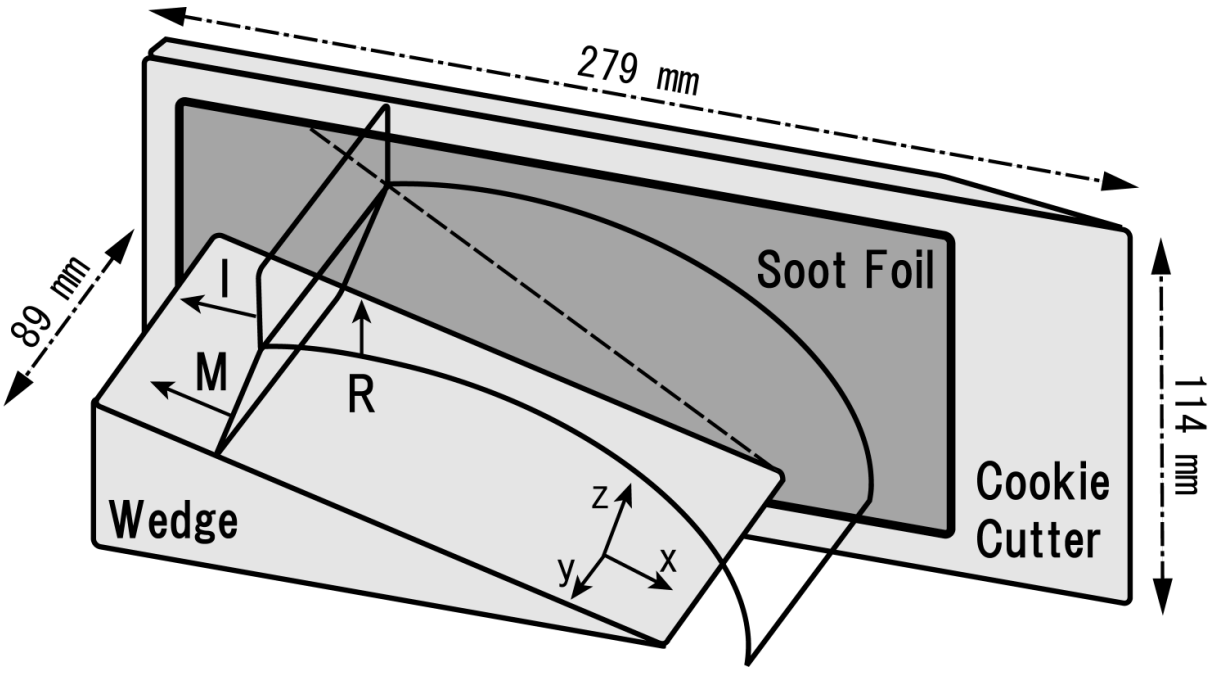

Figure 4.1: Schematic diagram of the test section and wedge placed inside the 15.2 cm diameter shock tube.

wiped off the foil completely. After the soot track has been formed, the soot foil is fixed with a spray-on acrylic paint.

4.2.2 Soot foil records in experiments

Soot foil records obtained in experiments are categorized into two groups; cases 1 and 2, cases 3 and 4 as in Table 4.1. In cases 1 and 2, two tracks are observed, as shown in Fig. 4.2(a). The first track is a straight line (dashed line F) at an angle to the wedge. Another line (dashed and single-dotted line S) exists between the first track F and the wedge. The line S is not straight and unclear near the leading edge of the wedge and around the edge of the soot foils. The soot between the first track F and the second track S is darker than its surroundings, and the soot between the second track S and the wedge is removed the most. Hence, the region between track F and track S is left as a dark belt of the soot.

In cases 3 and 4, a single track clearly appears in Fig. 4.2(b). Most of the soot between track F and the wedge is removed and looks lighter than the surrounding region. Soot foil records show two swirls near the leading edge and the top-end corner of the wedge. The reason swirls do not appear in cases 1 and 2 is related to the viscosity of the soot; low viscosity fluid on the foil slightly increases viscosity of the soot in cases 1 and 2. The effect of swirl formation seems to be not strong enough to leave tracks in cases 1 and 2. Soot track angles obtained in experiments will be examined further in the next chapter with numerical and theoretical consideration.

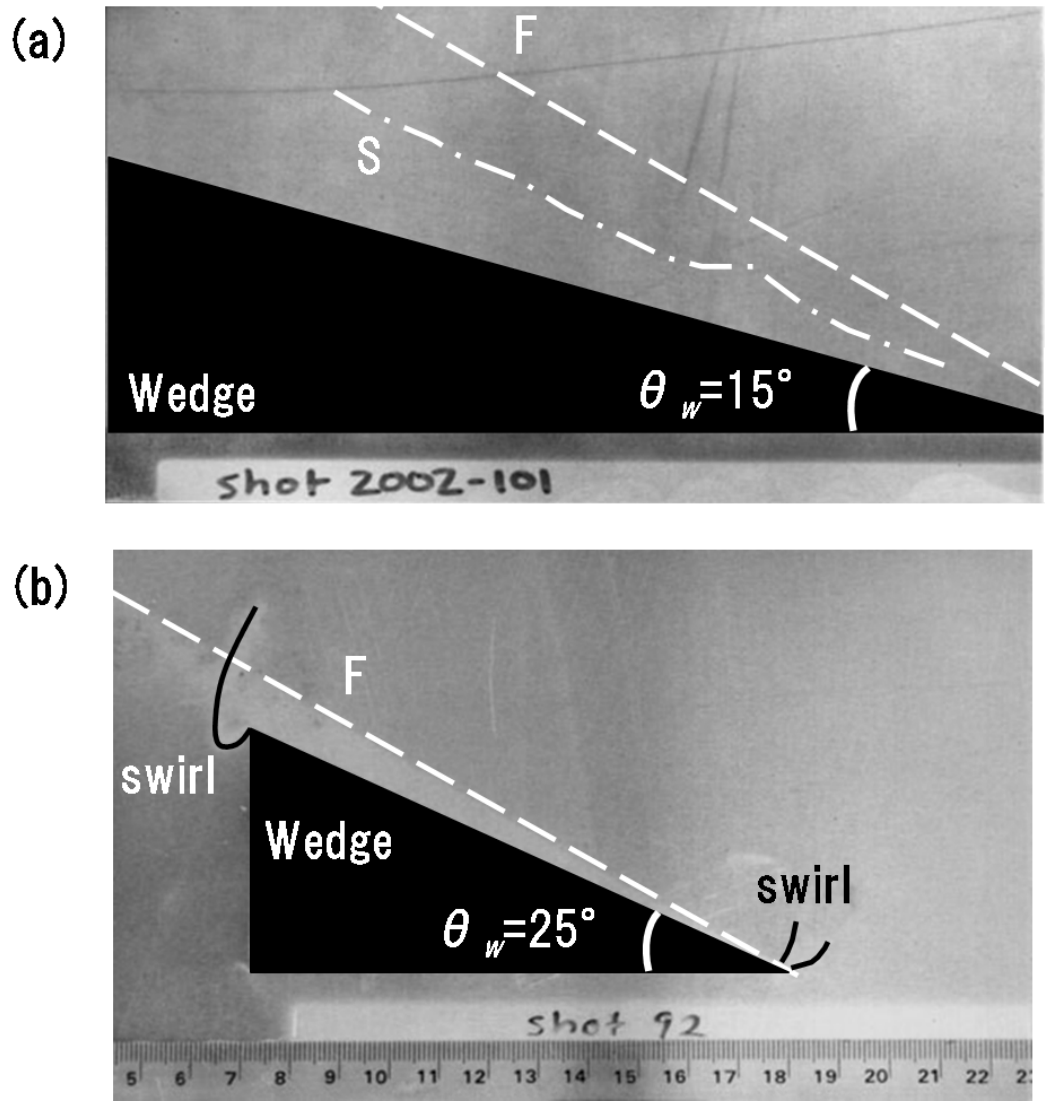

Figure 4.2: Soot foil records in Mach reflections. (a) case 1. (b) case 4. F, first track (dashed line); S, second track (dashed and single-dotted line).

Table 4.2: Numerical mixture conditions of air for gas-phase Mach reflection.

P_0 (initial pressure)	0.101 MPa
ρ_0 (initial density)	1.184 kg/m^3
T_0 (initial temperature)	298.15 K
γ (specific heat ratio)	1.4
c_0 (speed of sound)	346.2 m/s
ν_0 (kinematic viscosity)	15.4×10^{-6} m^2/s
Pr (Prandtl number)	0.72

4.3 Numerical Simulations of Mach Reflections in Gas-phase

4.3.1 Computational setup

Numerical simulations are conducted for Mach reflection over a wedge with 3-D compressible Navier-Stokes equations. As a numerical scheme, Yee's non-MUSCL type TVD upwind explicit scheme (1987) is utilized. The governing equations are integrated explicitly with the Courant number 0.5. Mixture conditions of air are listed in Table 4.2. Four cases are performed for parameters of Mach numbers M_S and apex angles of the wedge θ_w in Table 4.3. The numerical Reynolds number Re (= $M_S c_0/\nu_0$) and the post-shock conditions, P_1, ρ_1, and T_1 are calculated by the Rankine-Hugoniot relations for a given Mach number. The incident shock waves are stationary in the coordinate system, which moves along the wedge surface. Practical velocity components adopted in simulations are also presented in Table 4.3.

As shown in Fig. 4.3, a stretched grid system, especially in the *y* direction (depth), is utilized for a shock stationary coordinate system in a $151 \times 101 \times 51$ grid space. The computational domain is $185 \times 5.6 \times 114$ mm (*x*-, *y*-, and *z*-axes, respectively). The incident shock

Table 4.3: Practical velocity components adopted in simulations for four cases.

case	M_S	θ_w (°)	P_1/P_0	ρ_1/ρ_0	T_1/T_0	Re $\times 10^7$ (1/m)	u_0/c_0	w_0/c_0	u_1/c_0	w_1/c_0
A	1.9	15	4.045	2.516	1.608	4.271	1.967	0.0	0.861	-0.296
B	1.9	25	4.045	2.516	1.608	4.271	2.096	0.0	1.059	-0.484
C	1.2	15	1.513	1.342	1.128	2.697	1.242	0.0	0.946	-0.097
D	1.2	25	1.513	1.342	1.128	2.697	1.324	0.0	1.047	-0.129

wave is placed at a distance of 20 mm from the inflow boundary. A laminar boundary layer is assumed to develop on the soot foil, and the boundary layer on the wedge surface is neglected. The non-slip and isothermal boundary conditions are applied to the bottom $x - z$ plane corresponding to a soot foil. Minimum grid spacing in the y direction Δy_{min} is derived from Re in case A and set to 1.53 μm (= $0.01/\sqrt{\mathrm{Re}}$). Grid spacing exponentially increases by the constant stretching function with increasing distance y from the wall.

In the shock stationary coordinate system (Fig. 4.4), the wall velocity u_w is equal to the velocity of the wave relative to the upstream flow u_s in the laboratory system. In this study, the coordinate system moves not only with the incident shock wave, but along the wedge surface. Hence, the frontal incident shock wave becomes an oblique shock wave, and the post-shock flow is turned by the oblique shock. Since the velocity components of the wall differ from those outside the boundary layer, behind the incident shock, a skewed boundary layer develops on the wall. The main target of this simulation is to evaluate the shear stress reacting on the soot foil, and therefore the initial profiles are preliminarily calculated as the steady solutions, where the skewed boundary layer develops well. The boundary condition on the wedge is treated as a slip boundary, and thus a boundary layer on the wedge surface does not develop. Figure 4.5

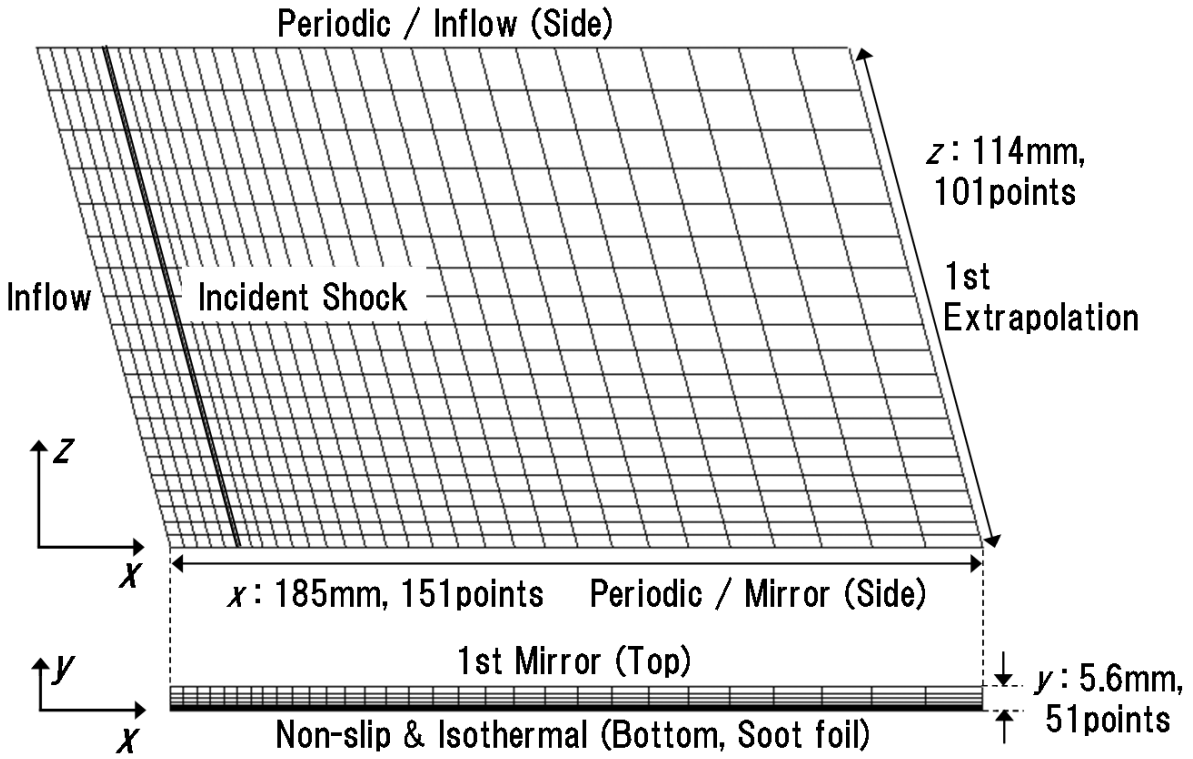

Figure 4.3: Grid system and boundary condition, for gas-phase Mach reflections.

shows the vectors of velocity components at x = 0.153 m from the shock front under the well-developed skewed boundary layer. In Fig. 4.5, the velocity components are abruptly turned from the outer velocity u_e toward the wall velocity u_w in the thin boundary layer. Computations for the Mach reflection are initiated by switching the boundary conditions of the side walls from periodic boundaries to mirror and inflow boundaries (see Fig. 4.3). In a real Mach reflection, waves reflected by the wedge have some curvature. In the present simulation, it is approximated that the incident shock is suddenly reflected by the long wedge surface and the reflected wave is straight.

4.3.2 Three-dimensional shock-induced boundary layer

For the sake of shortening calculation periods and saving resources, we adopt a shock stationary coordinate system rather than a laboratory coordinate system. In the shock stationary system,

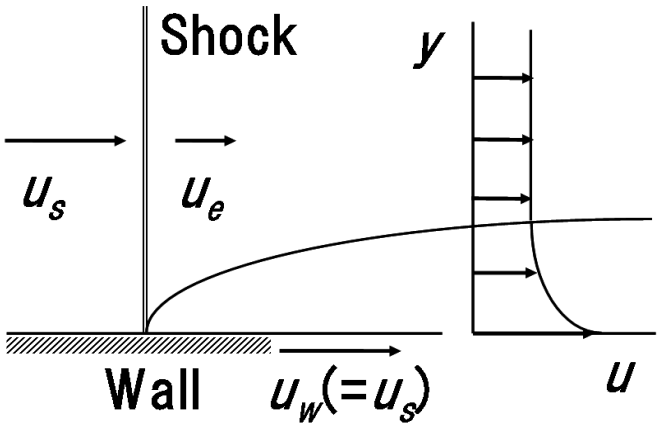

Figure 4.4: Schematic diagram of the shock-tube boundary layer in shock stationary coordinates.

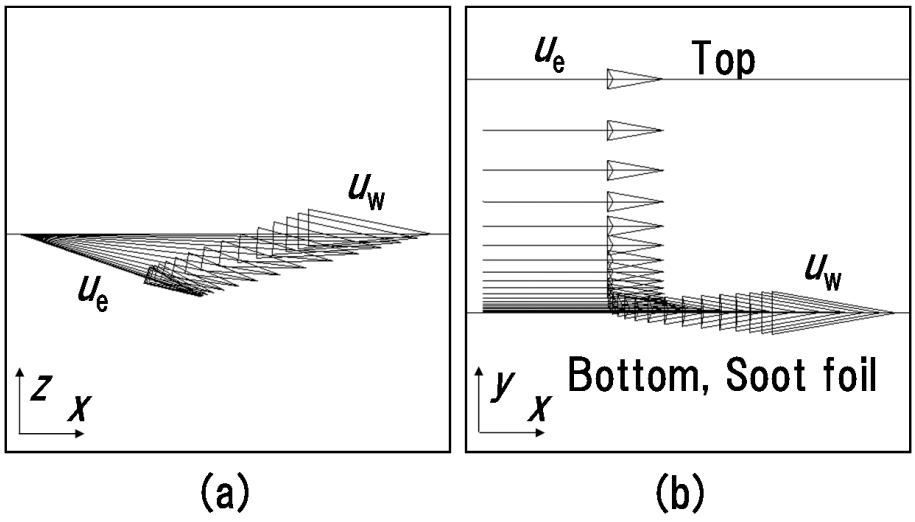

Figure 4.5: Vectors of velocity components, for 3-D skewed boundary layer at x = 0.153 m. (a) Top view. (b) Side view.

fewer grid points are necessary to achieve the same precision as those in the laboratory coordinate system. The boundary layer, however, becomes more complicated and is treated as the 3-D skewed boundary layer induced by the shock wave. In Cartesian coordinates, the 3-D compressible boundary-layer continuity and momentum equations, for steady flow, become

$$\frac{\partial(\rho u)}{\partial x} + \frac{\partial(\rho v)}{\partial y} + \frac{\partial(\rho w)}{\partial z} = 0 \tag{4.1}$$

$$\rho\left(u\frac{\partial u}{\partial x} + v\frac{\partial u}{\partial y} + w\frac{\partial u}{\partial z}\right) = -\frac{dP}{dx} + \frac{\partial}{\partial y}\left(\mu\frac{\partial u}{\partial y}\right) = \rho U\frac{\partial U}{\partial x} + \rho W\frac{\partial U}{\partial z} + \frac{\partial}{\partial y}\left(\mu\frac{\partial u}{\partial y}\right) \tag{4.2}$$

$$\rho\left(u\frac{\partial w}{\partial x} + v\frac{\partial w}{\partial y} + w\frac{\partial w}{\partial z}\right) = -\frac{dP}{dz} + \frac{\partial}{\partial y}\left(\mu\frac{\partial w}{\partial y}\right) = \rho U\frac{\partial W}{\partial x} + \rho W\frac{\partial W}{\partial z} + \frac{\partial}{\partial y}\left(\mu\frac{\partial w}{\partial y}\right) \tag{4.3}$$

where $U(x,z)$ and $W(x,z)$ are the free-stream velocity components (White, 1991, Chap. 4-12 & 7-1). If the potential flow depends on x but not on z, i.e. $U = U(x)$; $W = W(x)$, then the system of equations is simplified in that there is no dependence on z. Assuming that $U = U_\infty = const$ and $W = W_\infty = const$, we obtain

$$\frac{\partial(\rho u)}{\partial x} + \frac{\partial(\rho v)}{\partial y} = 0 \tag{4.4}$$

$$\rho\left(u\frac{\partial u}{\partial x} + v\frac{\partial u}{\partial y}\right) = \frac{\partial}{\partial y}\left(\mu\frac{\partial u}{\partial y}\right) \tag{4.5}$$

$$\rho\left(u\frac{\partial w}{\partial x} + v\frac{\partial w}{\partial y}\right) = \frac{\partial}{\partial y}\left(\mu\frac{\partial w}{\partial y}\right) \tag{4.6}$$

with $u(x,0) = u_w(x)$, $v(x,0) = w(x,0) = 0$, $u(x,\infty) \to U_\infty$, $v(x,\infty) = 0$, $w(x,\infty) \to W_\infty$. In this case, the pressure term in eqs. (4.2, 4.3) vanishes. From the initial velocity profile of case A, a hodograph plot of w vs. u normalized by the outer flow velocity u_e is obtained as shown in Fig. 4.6. Johnston (1960) suggests that a triangular hodograph shape is suitable for many unidirectional cross flows and Fig. 4.6 indicates good agreement with the triangle approximation. The correlation between u and w is confirmed, e.g. $w/u_e = -0.268u/u_e + 0.612$ for case A. If we model the main flow U by a 2-D velocity profile and correlate W with U through the hodograph, we can approximate such flow fields. Substitution the correlation equation into eq. (4.6) gives the same equation as eq. (4.5). Indeed, W depends on z in our

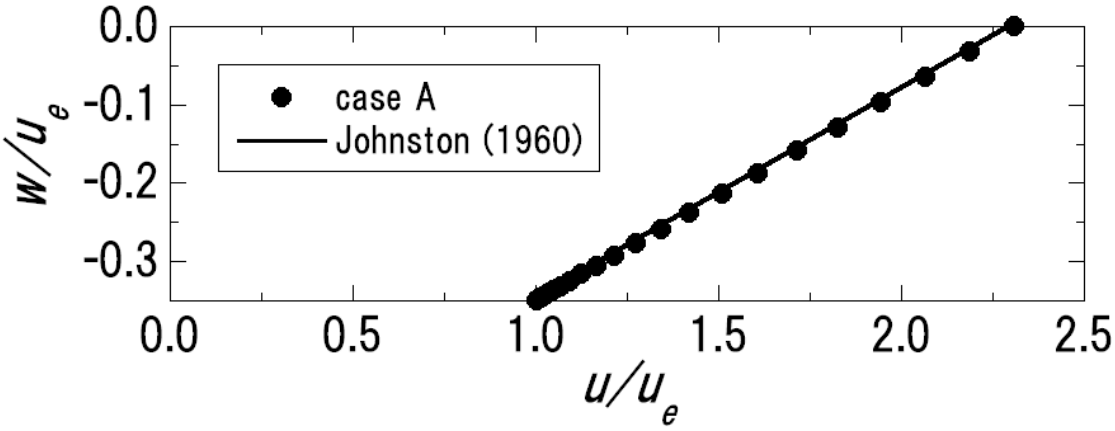

Figure 4.6: Hodograph of numerical solution in 3-D boundary layer with triangle approximation; Johnston (1960).

coordinate system because the incident shock is not orthogonal to the x-axis. The pressure term, however, still vanishes in the system where x- and z-axes are non-orthogonal under the conditions of $U = U_\infty$ and $W = W_\infty$.

With the application of Howarth's transformation (1948), Sturtevant & Okamura (1969) defined a boundary-layer variable η

$$\eta = \left(\frac{u_w + u_e}{2\nu_e x}\right)^{1/2} \int_0^y \frac{\rho}{\rho_e} dy \tag{4.7}$$

and a normalized stream function f such that

$$f'(\eta) = \frac{u - u_e}{u_w - u_e} \tag{4.8}$$

Assuming constant $\rho\mu$ and an ideal gas, the x-momentum equation and boundary conditions become

$$\begin{gathered} f''' + [\varepsilon\eta + (1 - 2\varepsilon)\, f]\, f'' = 0, \\ f'(0) = 1,\ f'(\infty) = 0,\ f(0) = 0 \end{gathered} \tag{4.9}$$

where $\varepsilon = u_e/(u_w + u_e)$: $\varepsilon = 1.0$ ($u_w = 0$; flat-plate boundary layer, Blasius solution), $\varepsilon = 0.5$ ($u_w = u_e$; weak shock waves), $\varepsilon = 0.43$ (cases C and D), $\varepsilon = 0.28$ (cases A and B), and $\varepsilon = 0.0$ ($u_w \gg u_e$; very strong shock waves).

4.3.3 Grid convergence study for gas-phase flows

In Fig. 4.7, the profiles $f'(\eta)$ of analytical solutions for $\varepsilon = 1.0$, 0.5, and 0.0 and numerical results in case A for $\varepsilon = 0.28$ (Benchmark, $151 \times 101 \times 51$ grid points) are plotted. With the definitions of eqs. (4.7) and (4.8), there is little dependence of $f'(\eta)$ on ε in analytical solutions. Every two points of numerical results are plotted at the distances from the shock along the x-axis: $l_x = 0.12$ m. For $\eta < 1$, numerical results are nearly universal and exist around the lines between $\varepsilon = 0.0$ and 0.5, while the results for $\eta > 1$ show little difference from analytical lines. As a comparison, the profiles $f'(\eta)$ obtained with grid size $189 \times 126 \times 64$ (Benchmark $\times 1.25^3$) and $226 \times 151 \times 76$ (Benchmark $\times 1.50^3$) at $l_x = 0.12$ m are also plotted in Fig. 4.7. Numerical results with higher grid resolution are closer to analytical lines than that of the benchmark result even if $\eta > 1$.

The local wall shear stress is determined from the velocity profiles of the bottom three grid points to obtain the velocity derivative near the wall surface. The thickness of the vorticity boundary layer depends on the distance from the shock wave l_x:

$$\delta_{b.l.} = \left(\frac{2\nu_e l_x}{u_w + u_e} \right)^{1/2}, \tag{4.10}$$

where ν_e is the kinematic viscosity outside the boundary layer. At $l_x = 0.16$ m, the thickness $\delta_{b.l.}$ of case A is 55.1 μm and is 36-times larger than the minimum grid spacing in the y direction, 1.53 μm. At $l_x = 0.04$ m, the thickness $\delta_{b.l.}$ is 27.5 μm and is still 18-times larger than the minimum grid spacing, in which half the grid points at $l_x = 0.16$ m exist in the boundary layer. The stretching factor in the y direction is 1.07 and the number of grid points in the boundary layer is less than 18 grid points (e.g. the tenth grid point from the wall is placed at $y = 23.7$ μm.)

For an ideal shock wave (zero thickness), the peak shear stress just behind the shock wave will be infinite. Because of the finite thickness of the shock wave in the numerical sim-

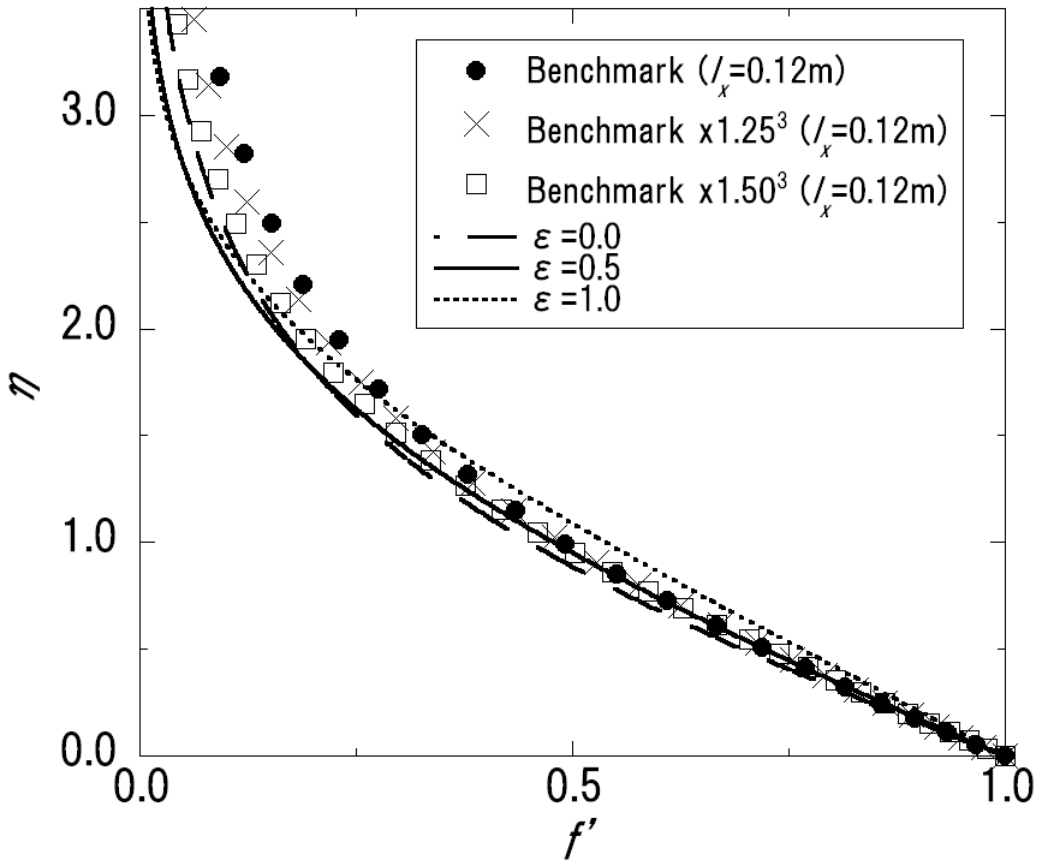

Figure 4.7: Normalized velocity profiles for numerical results ($\varepsilon = 0.28$) and three limiting cases ($\varepsilon = 1.0$, Blasius solution; $\varepsilon = 0.5$, weak shock waves; $\varepsilon = 0.0$, very strong shock waves).

ulation, the shear stress is finite just behind the shock front and the magnitude of the peak is dependent on the grid spacing. If we assume constant $\rho\mu$ and an ideal gas, then the dimensionless shear stress is defined as the friction coefficient C_f:

$$C_f = \frac{|\tau_{yx}|}{\frac{1}{2}\rho_e u_e^2} = \frac{\delta_{b.l.}}{l_x}\left[\left(\frac{u_w}{u_e}\right)^2 - 1\right] f''(0) \tag{4.11}$$

where $|\tau_{yx}|$ is the wall shear stress magnitude. Real gas effects and corrections for variable $\rho\mu$ are discussed by Mirels (1963, 1966) and Mirels & King (1966), and it is concluded that a real air solution is preferable for $M_S \geq 3$, and thus our numerical results can be discussed without real gas effects. The quantity of $f''(0)$ is evaluated by solving eq. (4.9): $\varepsilon = 1.0$, $f''(0) = 0.4696$; $\varepsilon = 0.5$, $f''(0) = 0.5641$; $\varepsilon = 0.0$, $f''(0) = 0.6275$. Figure 4.8 indicates the numerical (Benchmark) and analytical relations between the friction coefficient C_f and the distance from the shock l_x. The skin frictions in numerical simulations have finite peaks just behind the shock, and the gap between numerical and analytical skin frictions increases as the distance from the shock decreases. The finer resolution results (Benchmark $\times 1.25^3$, Benchmark $\times 1.50^3$) have larger peaks than that of the benchmark, depending on the grid spacing. In the case of $l_x > 0.04$, all numerical plots indicate almost the same profile. The wall shear stress gradually decreases as a function of the distance from the shock with increasing boundary layer thickness, which results in decreasing of the derivative of the velocity profile. It is confirmed that the wall shear profiles have the same tendency as the analytical curves.

4.3.4 Flow features of Mach reflections

Numerical simulation of Mach reflections over the wedge are investigated for parameters in Table 4.3. The flow features obtained in the cases with wedge angle 25° essentially show the same flow features as those cases with wedge angle 15°. Therefore we will discuss only the flow features of cases A and D, which have the same conditions as in the experimental pictures

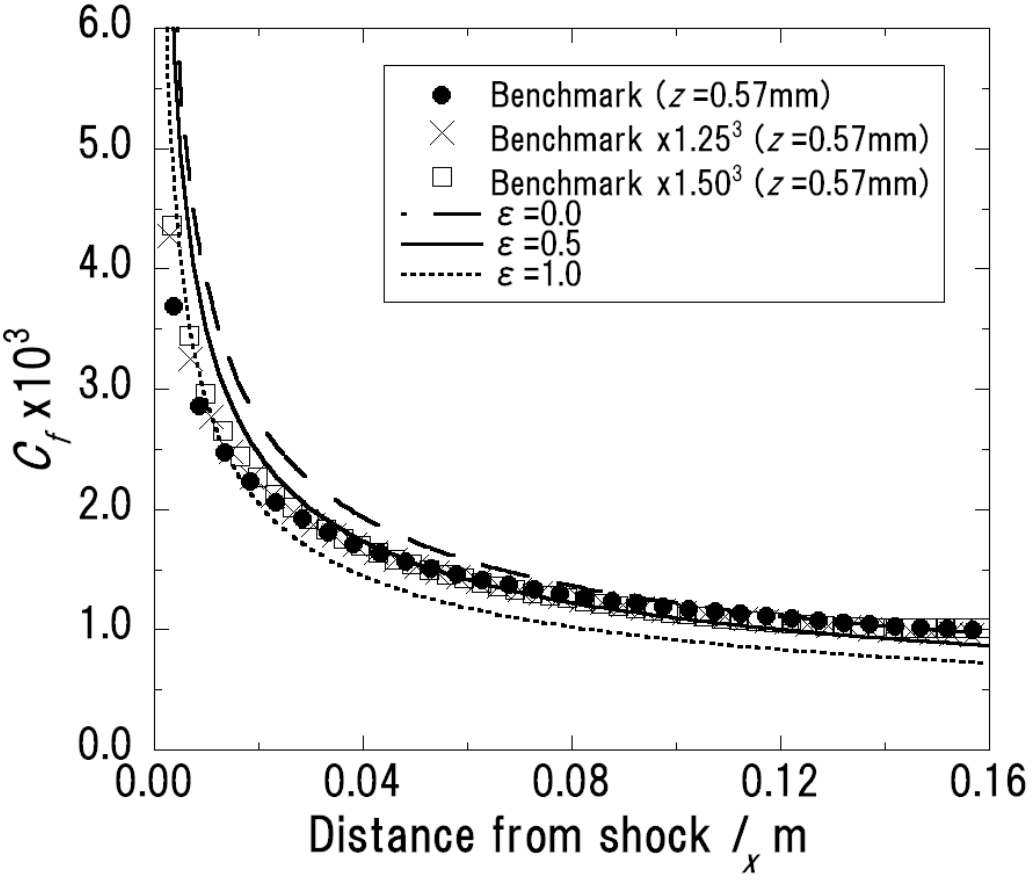

Figure 4.8: Relation between local friction coefficient and distance from shock for numerical results and three limiting cases.

of Fig. 4.2, and summarize cases B and C in §4.3.5 which discusses trajectory angles of triple points.

Figure 4.9 shows the flow feature of case A at t = 21.1 ms (100,000 time-steps) after the reflection of the incident shock wave. The triple point appears and gradually moves upward in the z direction as time-step increases because the normal shock progresses along the wedge in the experimental coordinate. Figure 4.9(a) shows the pressure contour distribution on the top $x - z$ plane (y = 4.91 mm) that is representative of the flow outside the boundary layer. Figures 4.9(b) and (c) show the temperature contour distributions on the top $x - z$ plane (y = 4.91 mm) and the bottom $x - z$ plane corresponding to the soot foil ($y = \Delta y_{min}$ = 1.53 μm). Since the outermost-computational grids are used for the boundary conditions and no ghost cell is adopted, above flow features are interior distributions bounded on the computational boundaries. Single Mach reflection (SMR) is expected to appear in case A, according to a number of previous studies (e.g. Hornung, 1986; Ben-Dor, 1992). Figures 4.9(a) and (b) indicate the typical flow features of SMR that consist of the incident shock I, the Mach stem M, and the reflected shock R. Although a slip line SL extending from the triple point in Fig. 4.9(b) is well defined in a flow far from the boundary layer, it becomes vague on the soot foil in Fig. 4.9(c) because the isothermal boundary condition and 3-D boundary layer obscure the slip line.

Figures 4.10(a) and (b) show pressure and temperature profiles on the top $x-z$ plane and the soot foil at three limiting cross-sections on three typical points: M (z = 0.57 mm), on Mach stem; T (z = 0.046 m), on triple point; I (z = 0.103 m), on incident shock. The profiles on the top plane are plotted with open symbols, and the soot foil with closed symbols. Post-shock pressure and temperature behind the incident shock (y = 4.91 mm, z = 0.103 m) maintain initial values in Table 4.3. Although suction of the boundary layer is generally assumed, the computational domain is sufficiently wide in the y direction for post-shock profiles not to be affected by the effect of suction. The difference between the top and the soot foil on pressure

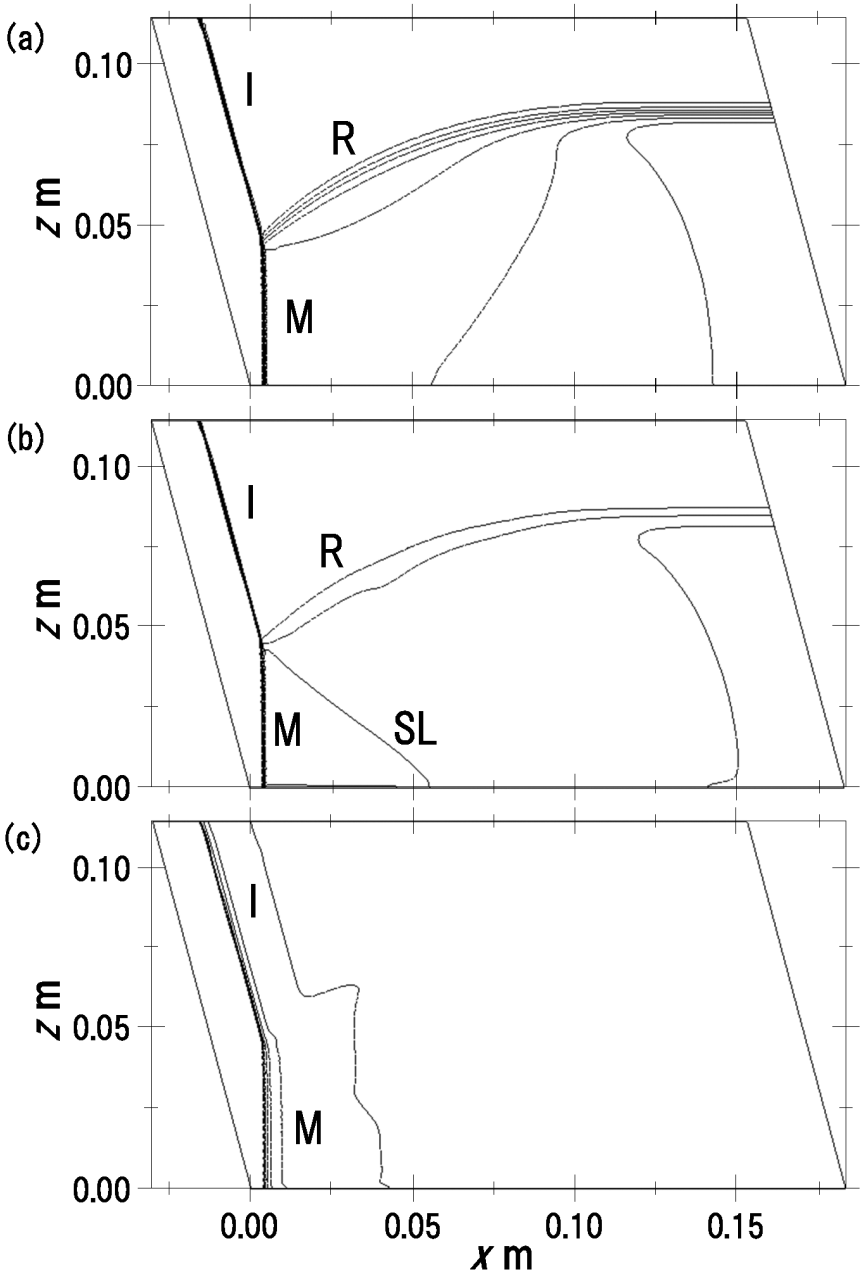

Figure 4.9: Flow features of case A, (a) pressure contour distribution on the top $x - z$ plane at $y = 4.91$ mm, (b) temperature contour distribution on the top plane, (c) temperature contour distribution on the soot foil at $y = 1.53$ μm (M: Mach stem, I: Incident shock, R: Reflected shock, SL: Slip line).

profiles in Fig. 4.10(a) is quite small, and thus pressure gradient in the y direction is little in accord with common assumptions in a boundary layer. Shock waves give remarkable jumps in temperature profiles on the top plane in Fig. 4.10(b), while boundary layers on the soot foil prevent temperature profiles from those jumps.

Strehlow & Biller (1969) defined the transverse wave strength S by the pressure jump across the reflected shock to evaluate the transverse wave which plays an important role in detonation propagation: $S = P_2/P_1 - 1$, where P_1 and P_2 are post-incident shock pressure and post-reflected shock pressure, respectively. Following Strehlow, reflected shock strength in case A is specified as $S = 0.26$. Previous experiments reported that transverse wave strength S of a gaseous detonation is approximately constant at 0.3–0.7 with an average value of about 0.5 (Strehlow & Biller 1969; Fickett & Davis 1979). Hence the Mach reflection appearing in case A corresponds to the weakest Mach reflection in detonation phenomena.

In the same way, the pressure and temperature contour distributions of case D at $t = 22.9$ ms (100,000 time-steps) are presented in Fig. 4.11. Previous experiments and numerical studies of Colella & Henderson (1990), Sasoh *et al.* (1992), Olim & Dewey (1992), Sasoh & Takayama (1994), Hunter & Brio (2000), and Zakharian *et al.* (2000) reported that von Neumann Mach Reflection (NMR) appears in weak shock reflection for comparatively low Mach number ($M_S \leq 1.5$) as in case D. Although 2-D numerical study with adoptive mesh refinement was performed by Zakharian *et al.* (2000), very few simulations have been conducted for NMR in a 3-D problem. In Figs. 4.11(a) and (b), the flow features of the top $x - z$ plane ($y = 4.91$ mm) indicate the typical NMR in which the incident shock wave and the Mach stem appear to be a single wave with a smoothly turning tangent around the triple point. Therefore the triple point is not a well-defined point. Instead of a clear slip line, there is the distributed shear layer SH in Fig. 4.11(b) that can be identified by a comparison of the contours behind the Mach stem against Fig. 4.11(a). In Fig. 4.11(c), small temperature variations are still observed behind the

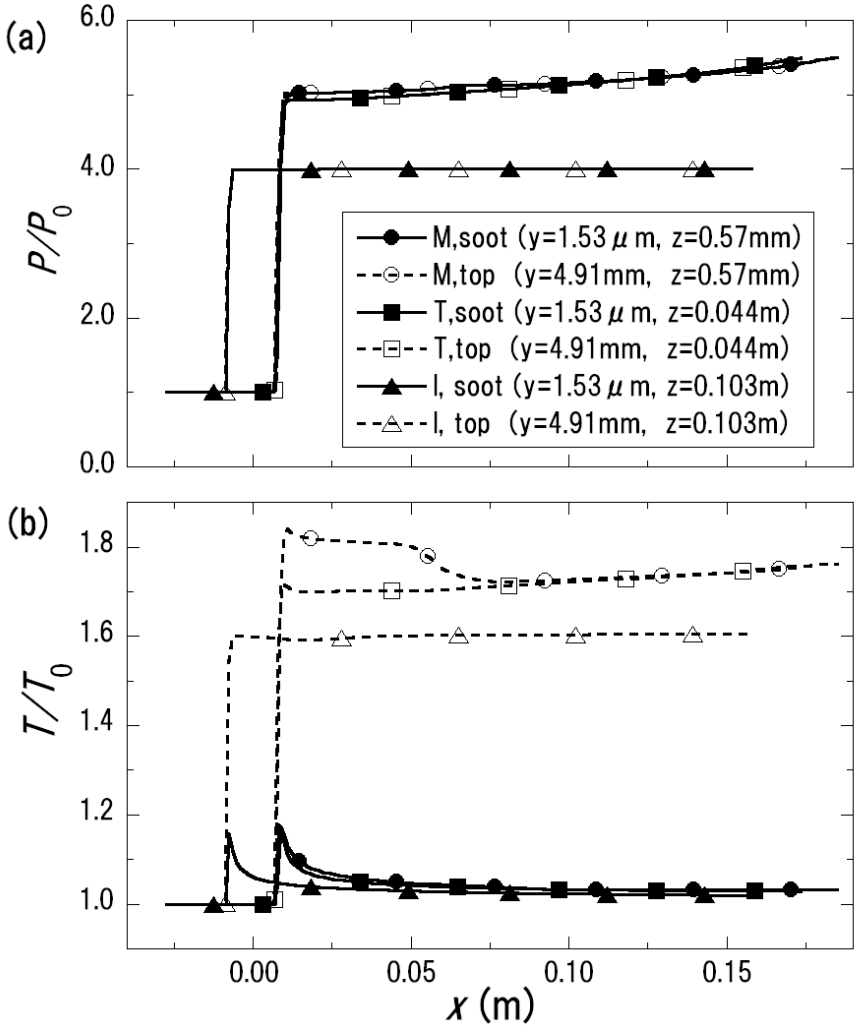

Figure 4.10: Three cross-section profiles on the top $x - z$ plane and the soot foil. (a) normalized pressure by the initial pressure P_0, (b) normalized temperature by initial temperature T_0 (M, z = 0.57 mm; T, z = 0.044 m; I, z = 0.103 m).

Mach stem, but it is hard to detect the shear layer in the flow near the soot foil.

Figures 4.12(a) and (b) show the cross-sections of pressure and temperature profiles along the *x*-axis in the same way as Figs. 4.10(a) and (b): (M) $z = 0.57$ mm, on Mach stem; (T) $z = 0.011$ m, the maximum curvature point on the Mach stem; (I) $z = 0.103$ m, on incident shock. Pressure gradient in the *y* direction does not appear as well as in case A, and pressure and temperature profiles on the Mach stem (M) have sharper peaks than those of case A. Transverse wave strength S around a triple point equals 0.20 and obviously falls below the strength of ordinary detonations.

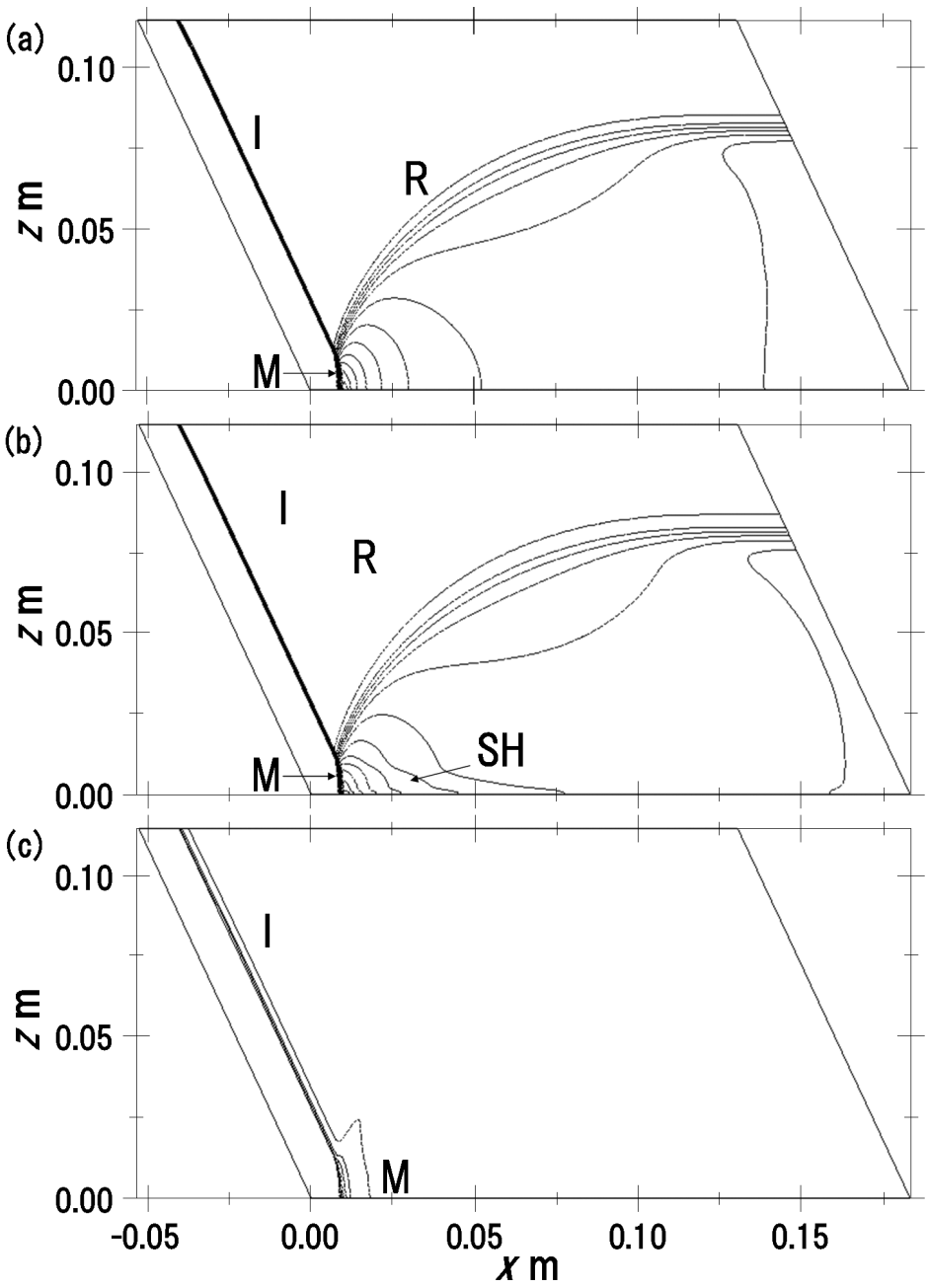

Figure 4.11: Flow features of case D, (a) pressure contour distribution on the top $x - z$ plane at y = 4.91 mm, (b) temperature contour distribution on the top plane, (c) temperature contour distribution on the soot foil at y = 1.53 μm (M: Mach stem, I: Incident shock, R: Reflected shock, SL: Slip line).

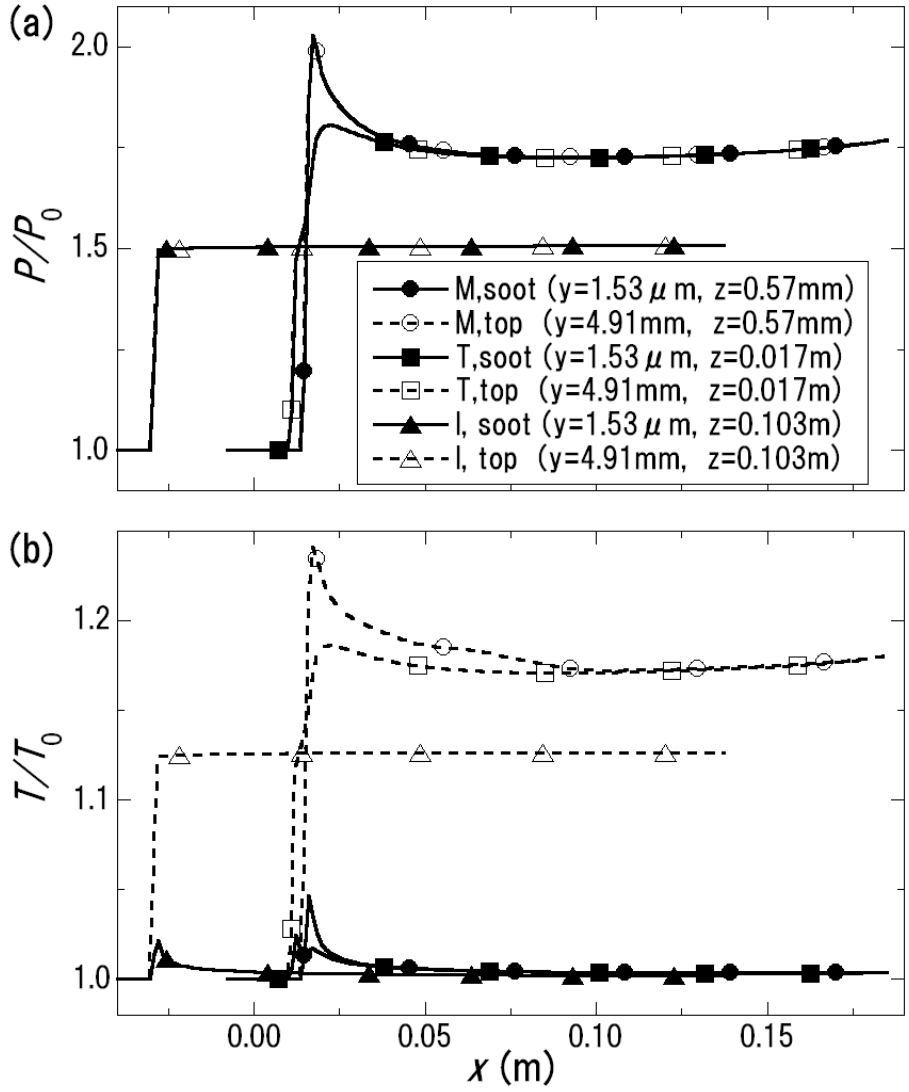

Figure 4.12: Three cross-section profiles on the top $x-z$ plane and the soot foil. (a) normalized pressure by the initial pressure P_0, (b) normalized temperature by initial temperature T_0 (M, z = 0.57 mm; T, z = 0.011 m; I, z = 0.103 m).

4.3.5 Numerical triple point track and experimental soot track angles

Soot track angles in experiments and trajectory angles of triple points in numerical simulations and theoretical analysis are presented in Table 4.4. Angles of soot track F in Fig. 4.2 are presented in Table 4.4, while the angles of soot track S are not because of non-straightness. Numerical trajectory angle of triple points in cases A and B (SMR) are readily detected while in cases C and D, two kinds of trajectory angles are given in Table 4.4. The angle χ_1 is the angle at the wedge to the trajectory where the incident shock meet with the reflected shock and the local curvature of the shock front vanishes. The other angle χ_2 is the angle at the wedge to the trajectory at which the Mach stem curvature becomes a maximum between foot of the Mach stem and the curvature vanishing point. Theoretical angles in cases A and B (SMR) are derived from the three-shock theory, and those in cases C and D (NMR) are calculated with glancing incidence angle of Ames (1953) and shock-shock angles of Whitham (1957) and Chisnell (1957). Sasoh *et al.* (1992) reported that the trajectory angle χ_1 is in agreement with the glancing incidence angle at small apex angles, the trajectory angle χ_2 corresponds to the shock-shock angle, and both angles tend asymptotically to merge at large apex angles. In cases A and B, experimental soot track angles show good agreement with numerical and theoretical angles of triple points. In cases C and D, experimental angles are close to numerical trajectory angle χ_2 and Whitham's shock-shock angles.

In case 1, the second soot track S looks nearly parallel to track F and locates almost in the middle between track F and the wedge as shown in Fig. 4.2. It is reasonable to suppose that the first soot tracks F are closely related to the triple point tracks. Hence a dark belt observed in experiments turns out to be built inside the Mach stem funnel. Figure 4.13(a) shows contours of maximum pressure history P_{max} reached at each location in space for case A. At the same speed of incident shock waves, instantaneous pressure distributions in the shock-

stationary system are gradually dislocated and superimposed onto the computational domain to obtain maximum histories in the laboratory system. The incident shock wave propagates from the right boundary through the computational domain and continues. In previous speculations, soot tracks are explained as scratching of the soot foils by the high pressure region around triple points. The explanation of scratching by the pressure peak does not accommodate experimental observation because there is not a higher pressure region around a triple point than the surroundings as shown in the maximum pressure history of Fig. 4.13(a).

Figures 4.13(b) and (c) show the instantaneous contours of vorticity magnitude $|\omega|$ on the top plane (exterior to the boundary layer, y = 4.91 mm) and the soot foil (y = 1.53 μm), respectively. According to Fig. 4.13(b), it is notable that variations of vorticity magnitude exist behind the Mach stem, especially along the slip line SL. In Fig. 4.13(c), vorticity variations along the slip line is not remarkable on the soot foil because the boundary layer obscures the slip line in the same way as temperature contours of Fig. 4.9. Hence, it would not be appropriate to explain the soot track formation by the effects of milling off due to vortices around slip lines.

Both compression due to pressures and scratching vorticity would be useful for understanding the soot blown off, but are not enough to discuss the explanation for the mechanism that piles up the soot around triple point trajectories and forms the dark belt in Fig. 4.2. On the basis of those results, it is proposed that shear stress variations, in direction and magnitude, created by the boundary layer adjacent to the soot foil, are dominant causes in soot track formation. In the following sections, the shear stress mechanism is verified by performing numerical simulation of soot motions with a simple interaction model of soot particles, or soot continuum, against gas phase flow.

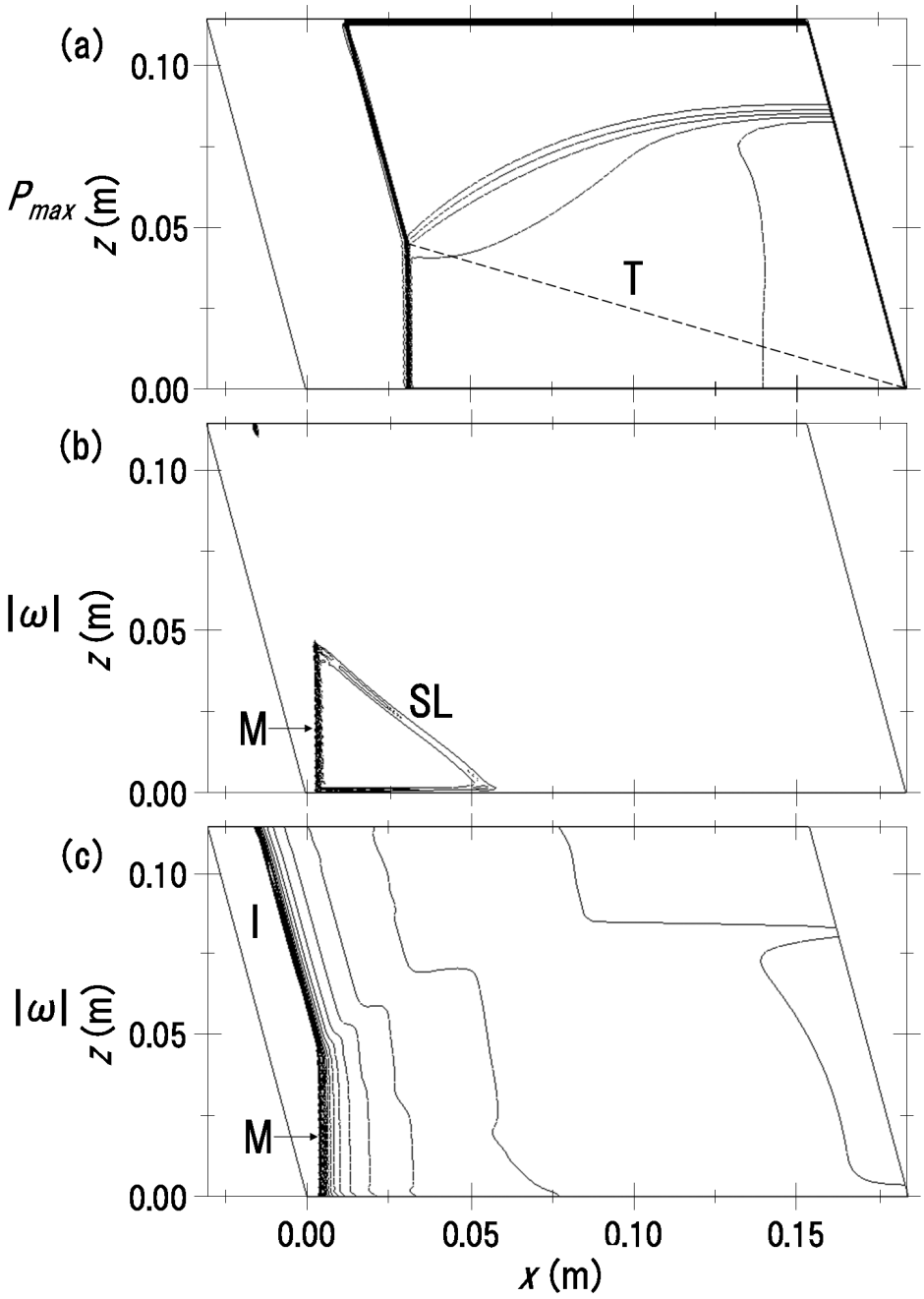

Figure 4.13: Contour distributions of (a) maximum pressure history P_{max} and vorticity magnitude $|\omega|$ (b) on the top plane at y = 4.91 mm, (c) on the soot foil at y = 1.53 μm. (M: Mach stem, I: Incident shock, R: Reflected shock, SL: Slip line).

Table 4.4: Summary of experimental soot track angles, numerical and theoretical trajectory angles of triple points, and numerical soot track angles.

case	M_S	θ_w (°)	Experiment (°) –first track F–	Simulation (°) –triple point track–	Simulation (°) –numerical soot track–	Three shock (°)	Ames (°)	Whitham (°)
A	1.9	15	15.6	16.7	14.9	17.1	-	14.7
B	1.9	25	9.9	11.9	9.0	11.0	-	11.1
C	1.2	15	7.8	χ_1: 12.8, χ_2: 11.2	8.8	-	10.5	9.1
D	1.2	25	5.2	χ_1: 7.7, χ_2: 5.9	5.3	-	0.5	6.3

χ_1: Trajectory angles of curvature vanishing point, χ_2: Trajectory angles of maximum curvature point, Ames (1953): Glancing incidence angle, Whitham (1957): Shock-shock angle.

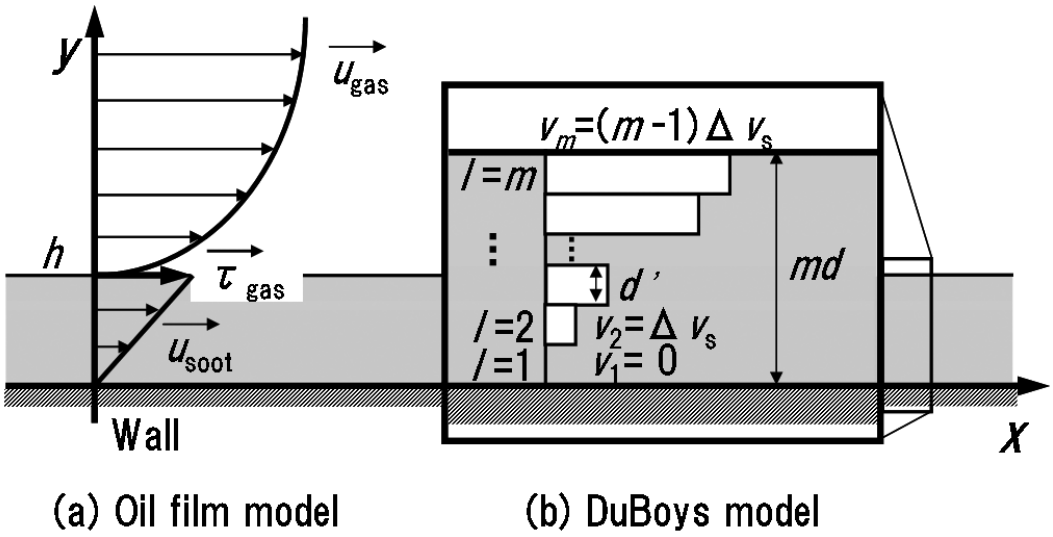

Figure 4.14: Schematic diagrams of (a) oil film interaction with gas flow and (b) moving layers of sediment as conceived by Duboys (Chang, 1988).

4.4 Shear Stress Mechanism on Soot Motion

4.4.1 Modeling of soot motion

The modeling of soot motion is carried out with two aspects; the first is that the soot is treated as a continuum, like thin oil film; the second is that the soot is regarded as an aggregate of particles, such as sediments in rivers.

a) Oil film model. A study of the motion of oil films on surfaces in air flow have been experimentally and theoretically performed for the surface oil flow technique for use in high-speed wind tunnels (Fig. 4.14(a)). There is a similar transportation mechanism of sediment movement in rivers to the oil film model. In the river engineering textbook of Chang (1988), DuBoys' formula for the bed-load is derived, assuming that uniform sediment grains move as a series of superimposed layers with each thickness d' of the same magnitude as the grain diameter (Fig. 4.14(b)). Hence, the flow sorted into the Couette flow occurs not only in general fluid, such as gas and liquid, but in bed-load transport. If the film is thin enough, the dominant force is the skin

friction, and a simple relation is obtained between the film thickness variation and the skin friction distribution. The pattern formation in oil flow visualization can be completely explained in terms of surface shear stress variations. The shear stresses τ must match at the air-soot interface in the wind-driven flows. Assuming that the soot is approximated as an incompressible fluid and the Coriolis acceleration is negligible, the soot thickness h obeys the following conservation equation (Squire, 1962);

$$\frac{\partial h}{\partial t} = -\frac{\partial}{\partial x}\int_0^h u dy - \frac{\partial}{\partial z}\int_0^h w dy \tag{4.12}$$

Assuming the Couette flow for soot, velocity components of u and w become (Tanner & Blows, 1976);

$$u = \frac{\tau_{yx} y}{\mu_s}, \quad w = \frac{\tau_{yz} y}{\mu_s} \tag{4.13}$$

where $u, w, \tau_{yx}, \tau_{yz}$ are the velocity components and the shear stresses arising from the gaseous boundary layer in the x and z directions, respectively, and μ_s is the viscosity coefficient of the soot layer. Hence, the key for understanding the soot thickness redistribution (the amount of soot on the foil) is to obtain unsteady distributions of shear stress of air (gas phase).

The governing equations (4.12, 4.13) are discretized with the MacCormack scheme (1971) in the 2-D computational domain (301×101 grid points) that has the same cross-section area of the 3-D benchmark grid for air. Shear stresses of air drive soot, though soot thickness distributions do not affect air flow; i.e., one-way coupling. Instantaneous distributions of shear stresses in air are simulated in advance, saved as history, and used to simulate time-dependent motion of soot. In soot redistribution simulations, the incident shock and the Mach stem are assumed to propagate from the right boundary through the computational domain, and shear stress distributions vary according to the shock positions.

b) Sliding particle model. A similar phenomenon to the soot motion appears in the sediment transport in rivers. Hence, a modeling of soot-particle motion is achieved in consideration of

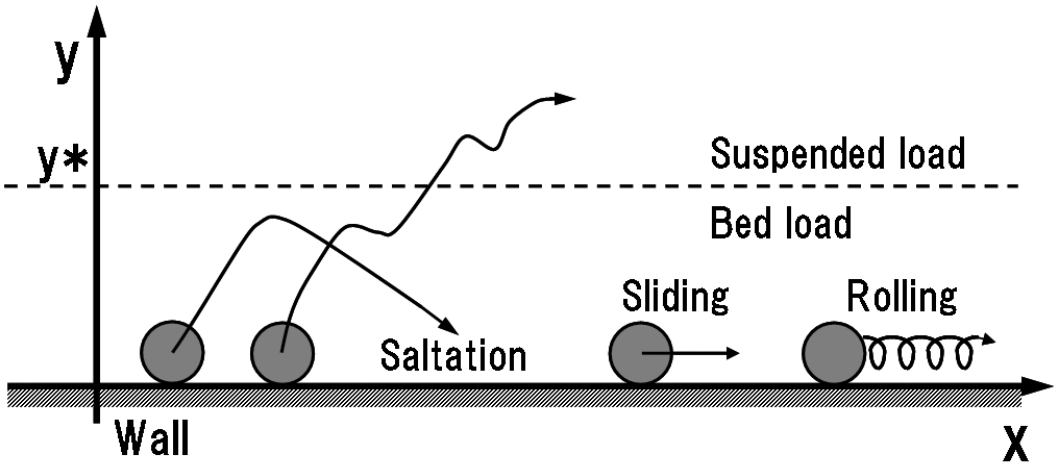

Figure 4.15: Schematic diagrams of sediment movement such as a sliding, rolling, and saltation.

river engineering. Sediment transportation in a stream is generally classified into bed load and suspended load (Chang, 1988; Leopold *et al*., 1995). Bed load applies to the sediment that moves by sliding, rolling, or saltation on or very near the bed, and suspended load moves in suspension when a particle jumps over limit height $y*$ as shown in Fig. 4.15. Physically, soot appears as grape-like clusters of fairly small spheres; the single spherules typically reach 10–25 nm in radius (Warnatz *et al*. 2001). Soot foil records can be clearly obtained in round and rectangular tubes even though they are placed upside down. According to characteristics of soot and soot foil records, it is assumed that gravity is not important in the soot redistribution process, and soot particles slide on the wall in the form of the bed load.

The discrete particle approach is utilized for numerical simulations of soot redistribution. This amounts to a statistical formulation of the problem, since there is a finite number of soot particles present in the field. Each of these computational particles characterizes a set of physical particles having the same characteristics such as location, velocity, radius, and mass. In this simulation, the particle is assumed to consist of spherical particles which distribute in the computational $x - z$ plane extracted from the 3-D grid in Fig. 4.3. On account of these

assumptions, the governing equations of soot particles become;

$$\frac{\mathrm{d}\mathbf{I}_i}{\mathrm{d}t} = \mathbf{F}_i, \quad \mathbf{I}_i = \begin{bmatrix} x_i \\ z_i \\ u_i \\ w_i \end{bmatrix}, \quad \mathbf{F}_i = \begin{bmatrix} u_i \\ w_i \\ \left(f_x/m_p\right)_i \\ \left(f_z/m_p\right)_i \end{bmatrix} \tag{4.14}$$

where $f_x = \pi r_p^2 \overline{\tau}_{yx}$, $f_z = \pi r_p^2 \overline{\tau}_{yz}$ are tractive forces for the x- and z-components, $m_p = 4/3\pi r_p^3 \rho_s$ and r_p are mass and radius of a soot particle, respectively, and $\rho_s = 1200$ kg/m^3 is soot density (National Astronomical Observatory of Japan, 2003, p.370). The accelerations by the forces are in inverse proportional to the radius of a soot particle. The averaged shear stress $\overline{\tau}$ is determined from shear stresses on four grid points that surround the particle i, and depends on the location of the particle in a computational cell. The governing equations (4.14) are solved by the fourth-order Runge-Kutta method. Initially, 64 particles are arranged in each computational cell (300 $\times$ 100 cells) and the total number of particles is 300 $\times$ 100 $\times$ 64. Each numerical particle has the representative volume initially determined by multiplying the 1/64 cell area by the initial soot height. The local soot thickness is the sum of representative volumes of particles existing around the grid divided by the cell area.

4.4.2 Shear stress distributions on the soot foil

Although combustion of soot due to the formation of soot tracks remains a matter to be discussed further, soot tracks due to a non-reactive shock are obtained by Mach reflection experiments. Pattern formation in oil flow visualization is explained with a simple interaction model of an air-oil interface; the shear stresses must match at the air-oil interface (White, 1991). Instantaneous distribution of shear stress at the soot foil (bottom $x - z$ plane) that affects the soot layer is derived from the 3-D simulation results. In the shock stationary frame, the wall shear stress has opposite sign to that in the laboratory frame. Figure 4.16(a) displays contour distri-

bution and vectors of shear stress magnitudes $|\tau|$ in case A. In Fig. 4.16(a), vectors of shear stress near the shock front change their direction across the triple points (z = 0.046 m). Figures 4.16(b) and (c) show cross-section profiles of the x- and z-components of shear stresses τ_{yx} and τ_{yz}, respectively, along z = 0.57 mm, on the Mach stem; z = 0.046 m, on the triple point; z = 0.103 m, on the incident shock. In Fig. 4.16(b), the peak and profile of shear stress τ_{yx} on the incident shock is comparatively close to those of τ_{yx} on the Mach stem; $[\tau_{yx}]_I = -1083$ N/m^2; $[\tau_{yx}]_M = -1263$ N/m^2. On the contrary, in Fig. 4.16(c), the profile of shear stress τ_{yz} on the Mach stem indicates a remarkable difference from that on the incident shock. The peak shear stress τ_{yz} on the incident shock equals 28.6 % of the peak shear stress τ_{yx} on the incident shock while the peak shear stress τ_{yz} on the Mach stem is small; $[\tau_{yz}]_I = -310$ N/m^2; $[\tau_{yz}]_M = -30$ N/m^2. As for the shear stress τ_{yz} on the triple point, it originally has a minus sign but gradually increases until it has a plus sign because of the flow induced by the reflected shock. The magnitudes of shear stresses on the incident shock and the Mach stem are comparatively close; $|\tau|_I = 1126$ N/m^2; $|\tau|_M = 1264$ N/m^2. To sum up, the soot behind both the Mach stem and the incident shock are equally driven along the x-axis, but the soot behind the incident shock is transported toward the wedge surface due to negative shear stress in the z-component.

Figure 4.17(a) shows contour distribution and vectors of the shear stress magnitudes $|\tau|$ in case D. Regarding the shear stress vectors, their directions gradually change from the incident shock through the Mach stem. Figures 4.17(b) and (c) indicate cross-section profiles of shear stresses along z = 0.57 mm, on the Mach stem; z = 0.011 m, on the maximum curvature point; z = 0.103 m, on the incident shock. The peak shear stress τ_{yx} on the Mach stem is almost twice that on the incident shock as shown in Fig. 4.17(b); $[\tau_{yx}]_I = -237$ N/m^2; $[\tau_{yx}]_M = -473$ N/m^2. According to Fig. 4.17(c), the peak shear stress τ_{yz} on the Mach stem is half of that on the incident shock, and the profile on the Mach stem immediately decrease behind the shock; $[\tau_{yz}]_I = -114$ N/m^2; $[\tau_{yz}]_M = -50$ N/m^2. The magnitude of shear stresses on the incident shock

is nearly half of that on the Mach stem; $|\tau|_I = 262$ N/m^2; $|\tau|_M = 475$ N/m^2. In case D, the shock strength increases as it approaches the wedge, and thus the soot inside the Mach funnel is driven by stronger shear stress than outside the funnel.

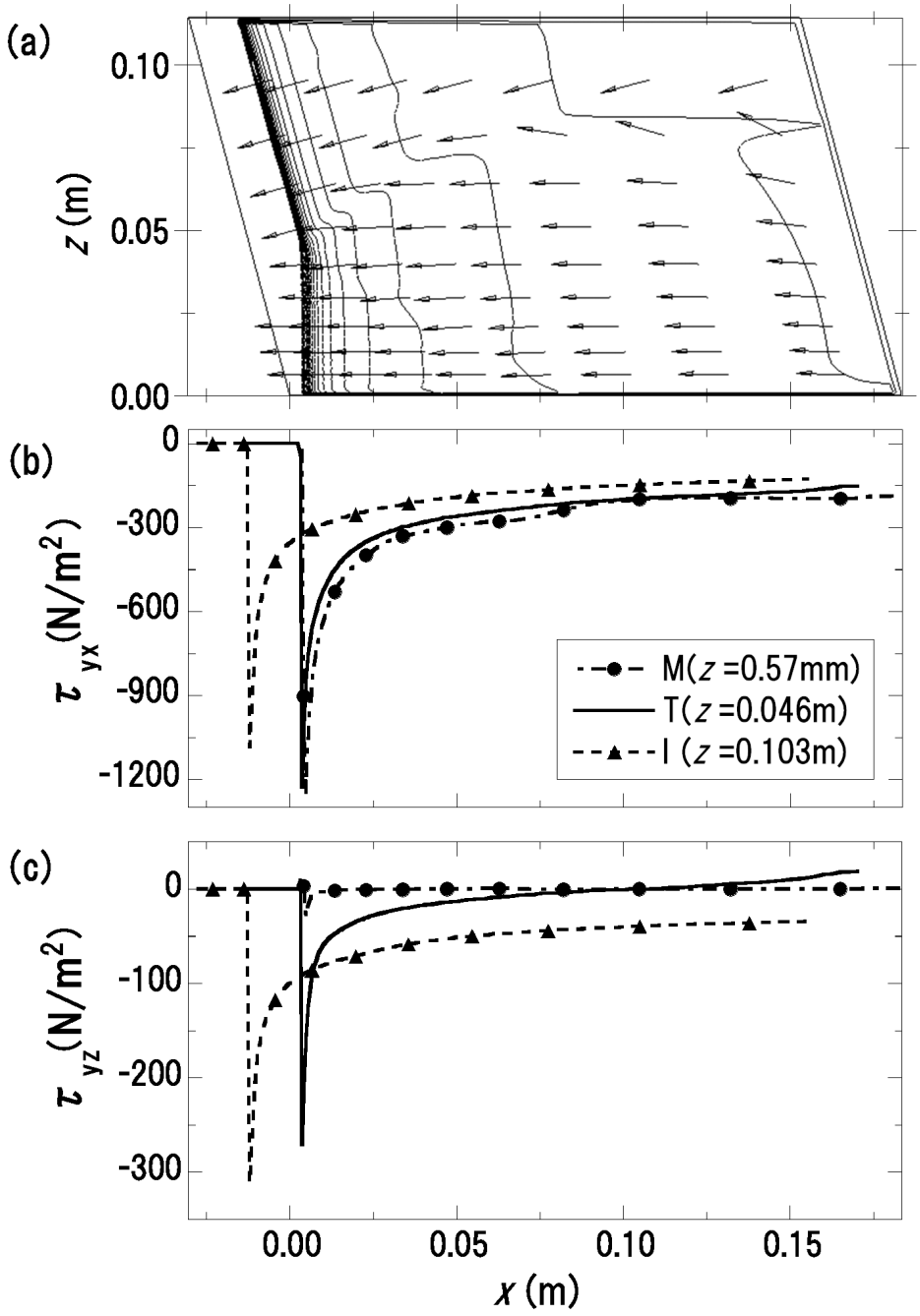

Figure 4.16: Instantaneous shear stress in case A. (a) Contour distributions and vectors of magnitude $|\tau|$, (b) τ_{yx} profiles, (c) τ_{yz} profiles. M, profile on Mach, z = 0.57 mm; T, profile on triple point, z = 0.044 m; I, profile on incident shock, z = 0.103 m.

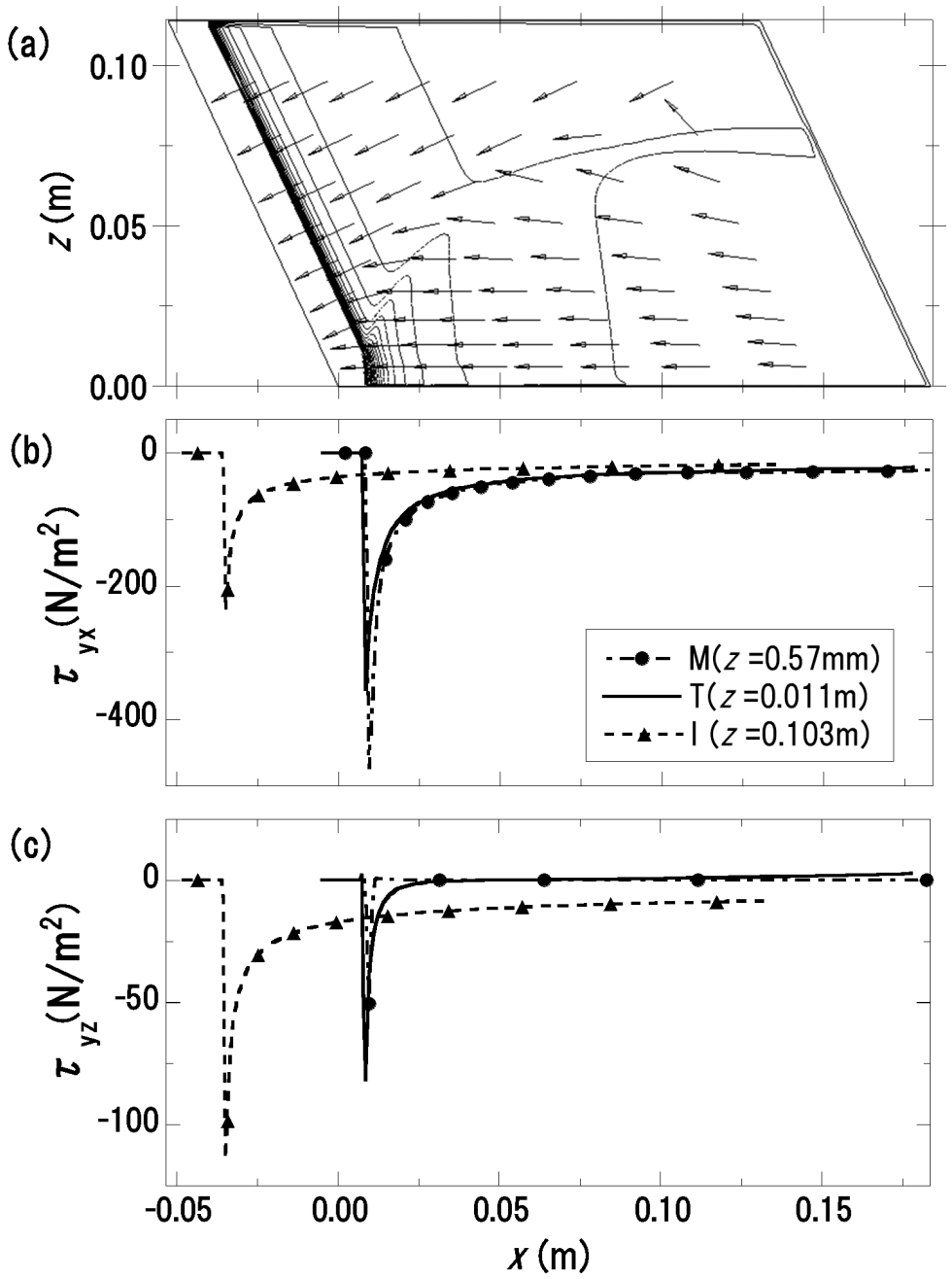

Figure 4.17: Instantaneous shear stress in case A. (a) Contour distributions and vectors of magnitude $|\tau|$, (b) τ_{yx} profiles, (c) τ_{yz} profiles. M, profile on Mach, z = 0.57 mm; T, profile on triple point, z = 0.011 m; I, profile on incident shock, z = 0.103 m.

4.4.3 Soot redistribution simulations

Figure 4.18(a) shows the soot thickness h normalized by the initial soot thickness h_0 in case A with the oil film model, explained in §4.4.1, in the form of gray-scale distribution. The darker color indicates the thicker region. In this model, parameters are initial soot thickness h_0 (= 5.0 mm) and soot viscosity. The soot viscosity is not well known and is approximated with water viscosity $\mu_0 = 8.9 \times 10^{-4}$ Pa s at 298.15 K. Initial soot thickness is determined so that the variation of soot thickness Δh of the same order as the initial soot thickness h_0 and thus the variation of soot redistribution clearly appears. As the initial soot thickness is decreased with the fixed viscosity, variation of soot thickness becomes small and most of the soot behind the shock wave remains on the wall. Hence, even if an arbitrary viscosity coefficient is chosen (e.g. $\mu_{air} = 18.2 \times 10^{-6}$ Pa s), the same feature of soot tracks can be obtained with the appropriate initial soot thickness (e.g. h_0 = 0.1 mm for air).

There are two notable thick regions of soot in Fig. 4.18(a): dark regions just behind the shock front and around the trajectory of the triple point. Figure 4.18(b) indicates cross-sections of soot thickness on the Mach stem, $z = 0.57$ mm; on the triple point, $z = 0.046$ m; and on the incident shock, $z = 0.103$ m. The peak soot thickness on the incident shock turns out to be close to that on the Mach stem; $h_I/h_0 = 1.14$; $h_M/h_0 = 1.13$. In Fig. 4.18(b), soot thickness gradually decreases from peaks away from the front along the x-axis. Figure 4.18(c) shows cross-sections of soot thickness on the lines (i), (ii), and (iii) drawn in Fig. 4.18(a). In Fig. 4.18(c), it can be seen that soot piles up and forms three peaks. The soot tracks are not completed, especially behind the shock fronts. Hence, the trajectory of the soot track is determined at the intersection of the soot track and the line (ii). Soot track angle around the leading edge is 14.9° (the bottom right corner, $x = 0.185$ m, $z = 0.0$ m), as shown in Table 4.4, and is fairly close to the experimental track angle of case 1 in Table 4.1. The slope of the

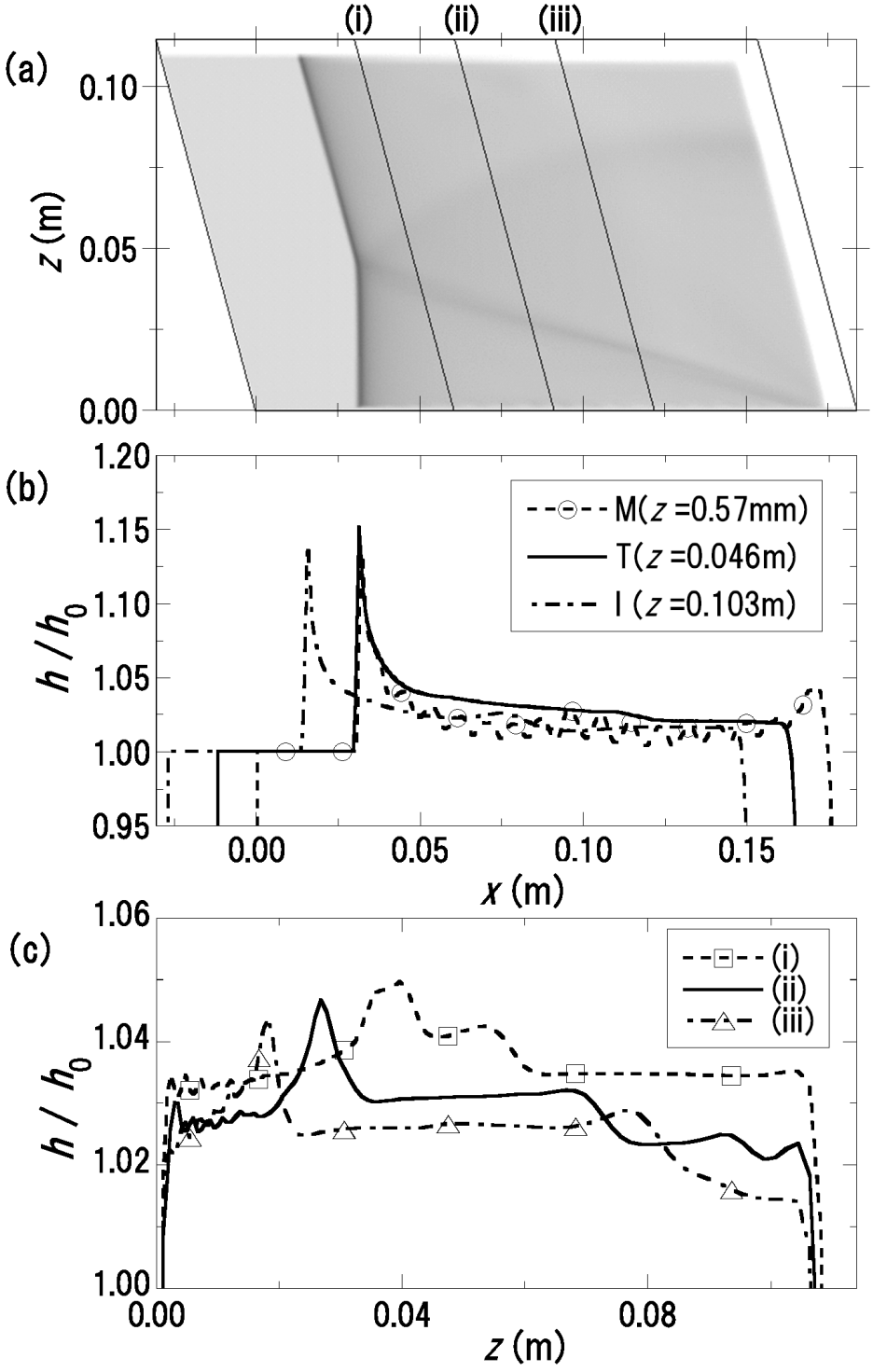

Figure 4.18: Soot thickness profiles of the oil film model in case A. (a) Contour distribution, (b) Profiles along the *x*-axis. (c) Profiles along the *z*-axis.

soot track itself is 16.4°, which is close to the angle of the triple point of air; 16.7° (refer to Table 4.4). Soot track angles in experiments are measured as the angle around the leading edge and the soot tracks in the same manner as the former numerical angles around the leading edge. Therefore, all numerical soot track angles listed in Table 4.4 are obtained in this manner.

The soot track angles in experiments are smaller than numerical and theoretical angles of triple points. The parameters adopted in the simulations for soot redistributions are regarded as adjusting parameters, and thus arbitrary angles of numerical soot tracks might be obtained. The whole angles, however, would become less than the angles of triple points because soot is redistributed, being shifted downstream. This might be the reason track angles of experiments are generally less than numerical and theoretical angles. In Figs. 4.18(b) and (c), soot thickness of all lines seems to increase from unity while the total amount of soot is conserved. In the simulations, the soot does not enter from the right and top boundaries, even if shear stress turns their vectors toward the computational domain. Hence, increasing portion of soot thickness is transported from those boundaries and the soot around the boundaries decreases to less than unity.

With the sliding particle model, a similar result to the oil film model is obtained as shown in Fig. 4.19(a). Parameters in the sliding particle model are initial soot thickness h_0(= 20 μm) and particle radius r_p(= 0.27 nm). In this model, initial soot thickness is not important for the shade of soot tracks, but the particle radius dominates the magnitude of soot thickness variations. Parameters are chosen by the same criterion as the oil film model and thus the computational particle radius of 0.27 nm becomes much smaller than that of typical soot particle radius. In Fig. 4.19(b), cross-sections of soot thickness on the lines (i), (ii), and (iii) are presented. The solution of the sliding particle model is not as smooth as than of the oil film model (Fig. 4.18(c)). Moreover, the simulation of the particle sliding model requires much more CPU time and memory. To perform simulations of soot redistributions in case A, it is better to

use the oil film model. Both the drag force, defined by drag coefficient of Henderson (1976), and skin friction between the particle and the wall due to gravity, are adopted for simulations, but there was little influence on results under those parameter sets.

In experimental cases 1 and 2 (SMR), it was pointed out in the previous section §4.2.2 that dark soot belts between the first track F and the second track S remain inside the Mach stem funnel. Since only the soot behind the incident shock moves toward the wedge surface, the dark soot belts pile up inside the Mach stem funnel by the collision of soot behind the incident shock and the Mach stem. It is clear that the dark soot belt (the second track S) observed in cases 1 and 2 are formed by this effect, the variation of the shear stress τ_{yz}.

In the same manner as in case A, soot redistribution simulations are performed in case D with the oil film model (Fig. 4.20) and the sliding particle model (Fig. 4.21). In Fig. 4.20, the initial soot thickness h_0 is set to be 0.9 mm and the viscosity of soot is the same as in case A ($\mu_0 = 8.9 \times 10^{-4}$ Pa s). As the initial soot thickness increases, soot tends to move more. When the initial soot thickness increases to more than 0.9 mm, the simulation is not performable due to numerical stiffness. Cross-sections of soot thickness are presented in Fig. 4.20(b), and indicate two prominent peaks; soot tracks due to the triple point structure ($z < 0.02$ m) and the reflected shock ($z \geq 0.02$ m). In Fig. 4.20(a), the soot inside the Mach stem funnel is generally darker than its surroundings, which can be seen in Fig. 4.20(b) when $z \leq 0.01$ m. In the oil film model, the soot piles up inside the Mach stem funnel. Soot track angle with the point of the trough on line (ii) equals 5.3°, and shows good agreement with the experimental result of 5.2° in case 4, Table 4.4.

In the sliding particle model, a soot removal process can be simulated. When the radius of soot particle is sufficiently decreased, the particle finally moves at the same speed as the frontal shock. Figure 4.21(a) shows a distribution of soot thickness in case D with the initial soot thickness $h_0 = 2.5$ μm and the particle radius $r_p = 0.033$ nm. With those parameters,

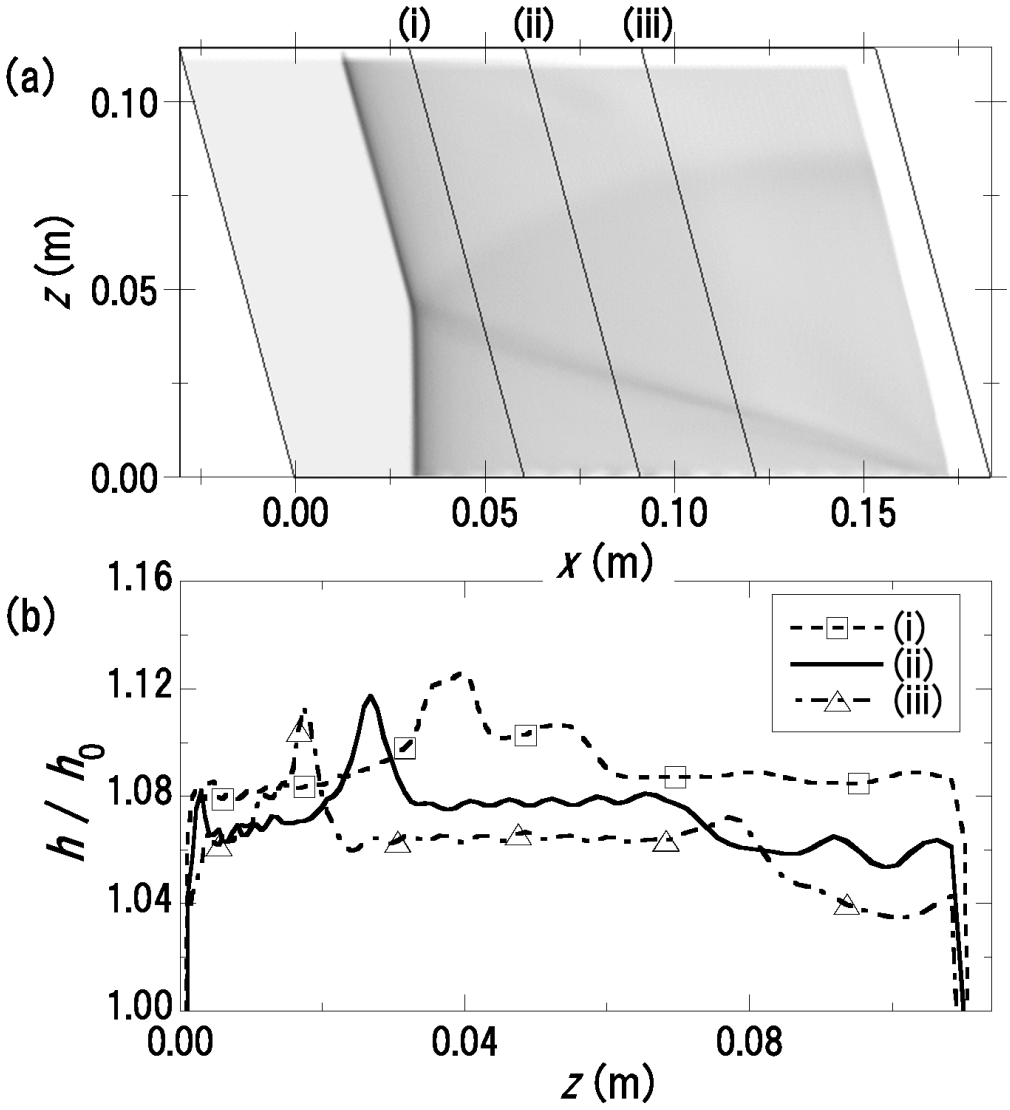

Figure 4.19: Soot thickness profiles of the sliding particle model in case A. (a) Contour distribution. (b) Profiles along the *z*-axis.

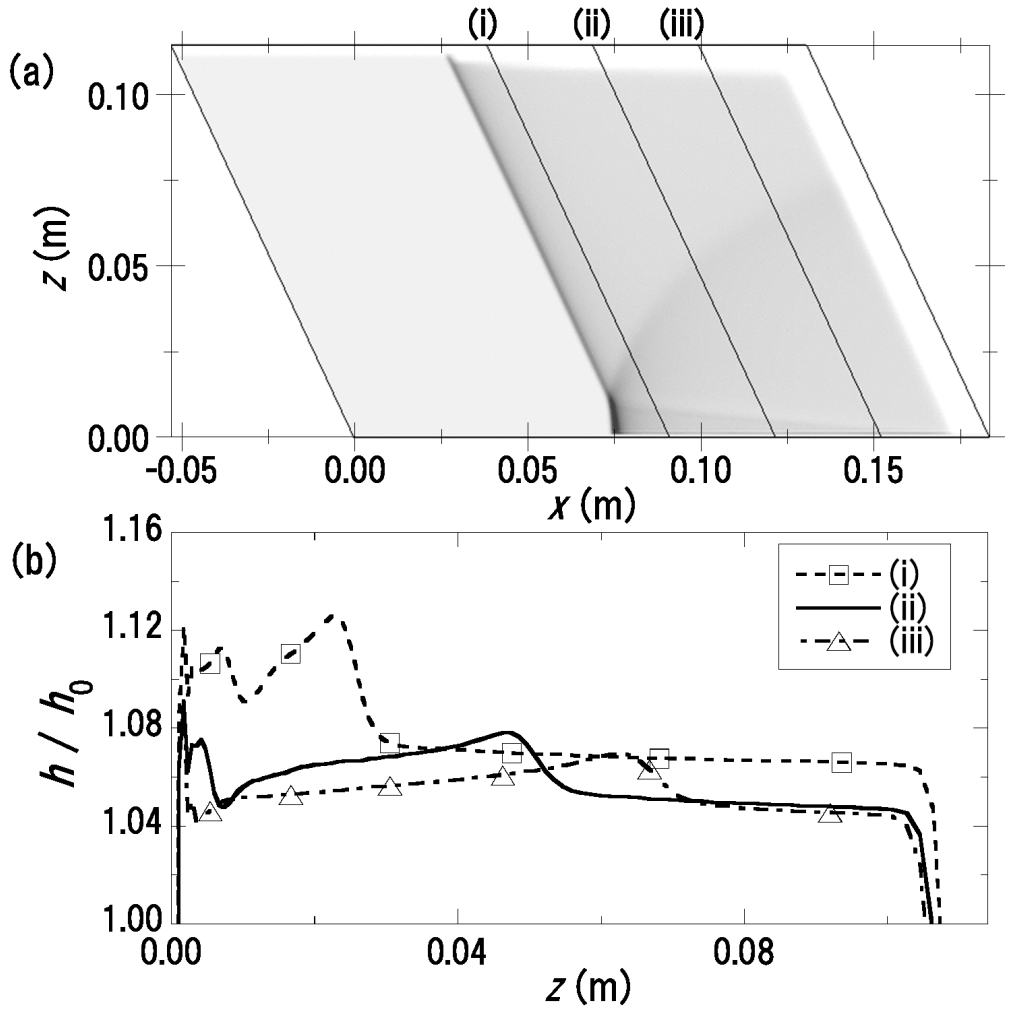

Figure 4.20: Soot thickness profiles of the oil film model in case D. (a) Contour distribution. (b) Profiles along the *z*-axis.

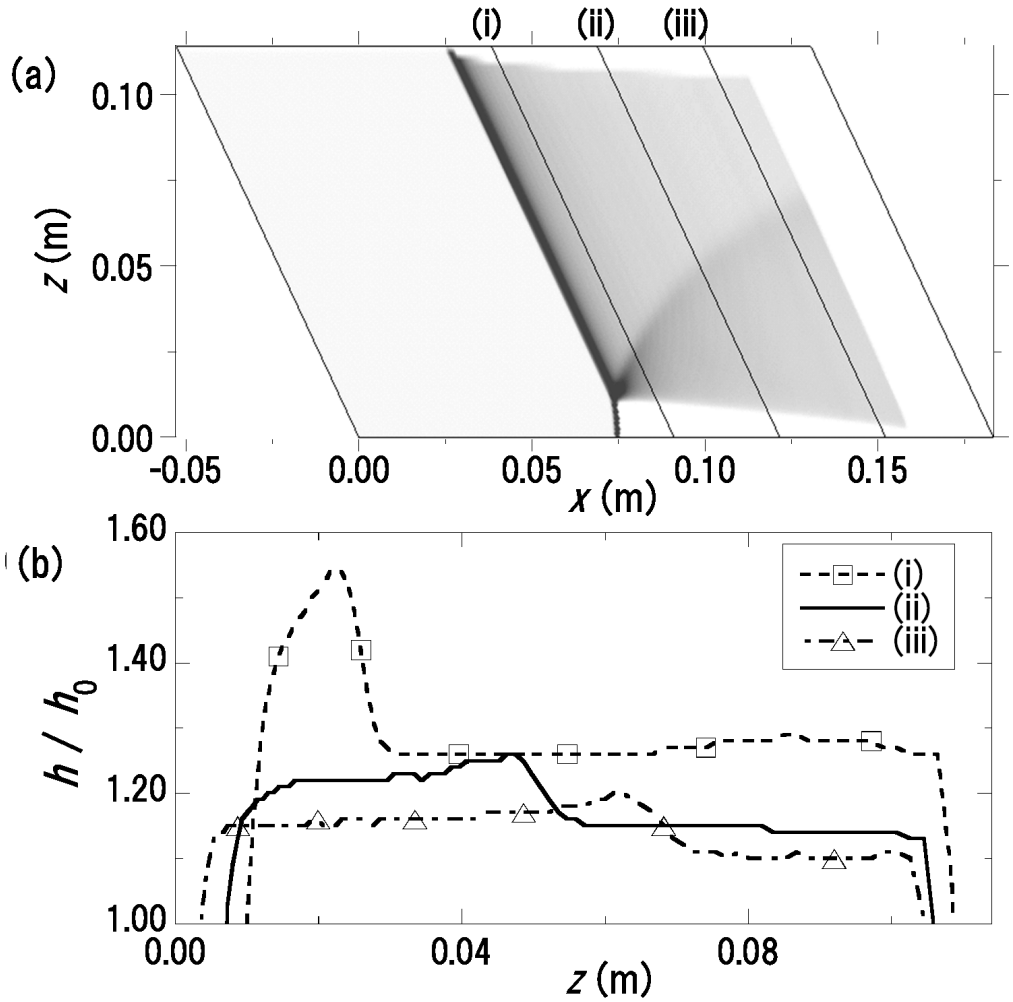

Figure 4.21: Soot thickness profiles of the sliding particle model in case D. (a) Contour distribution. (b) Profiles along the *z*-axis.

the soot is readily transported and removed off the wall below the trajectory of the triple point (white region below the trajectory in Fig. 4.21(a)). In the experiment of case 4, the soot inside the Mach stem funnel is removed off the plate (refer to §4.2.2). This model proves to be more appropriate in treating soot redistribution than the oil film model because of the robustness against stiffness in representing the soot removal. Soot track angle with the point on line (ii) that is the boundary of removed soot is 6.4°, a little larger than the experimental result in case 4.

4.4.4 Application to soot track formation in detonation

On soot foil records in detonations, the soot where the Mach stem propagates is usually darker than the region where the incident shock propagates. Some soot tracks of H_2-O_2-Ar mixture have dark soot belts in the Mach stem funnel. Figure 4.22(a) indicates the striped soot foil records in detonation, prepared by removing tapes after being covered with soot. Many streams of soot can be observed inside the removed soot regions and lengths of those streams have some cyclic tendency. To examine the detail of those streams, an enlarged image is presented in Fig. 4.22(b). This image shows the soot inside the Mach funnel is darker than that of the incident shock side. Moreover, the soot looks piled up inside the funnel. The soot piled up inside the trajectory of triple points seems to be pushed forward due to the effect of the post-shock flow. Figure 4.22(c) illustrates the schematic diagram of the mechanism of soot track formation in detonation. In Fig. 4.22(c), the Mach stem is rather bent than straight and thus the soot behind the Mach stem also impinges the triple point track. The mechanism in detonation can be explained with the same mechanism observed in Mach reflections with the exception of the curvature of the Mach stem.

The effect of the pressure gradient in the shock front on the particles can be estimated as impulsive acceleration due to the diffraction of the shock over the particle. The particles are comparable to or smaller than the wave thickness, so this is not quite correct but is a useful starting point. The pressure gradients due to the shock wave only exist within the shock front, which is very thin, 0.5 μm for a Mach 5 shock in air at 0.1 MPa initial pressure. This is similar to the size of a clump of soot particles. So even though the forces are large, the pressure gradient only acts on a single clump of particles for a short period of time, 25 ns for a $M = 6.0$ shock in air. The soot layer is incompressible so that the forces due to the pressure gradient in the shock only act on the soot particles at the top of the soot layer. Otherwise, the

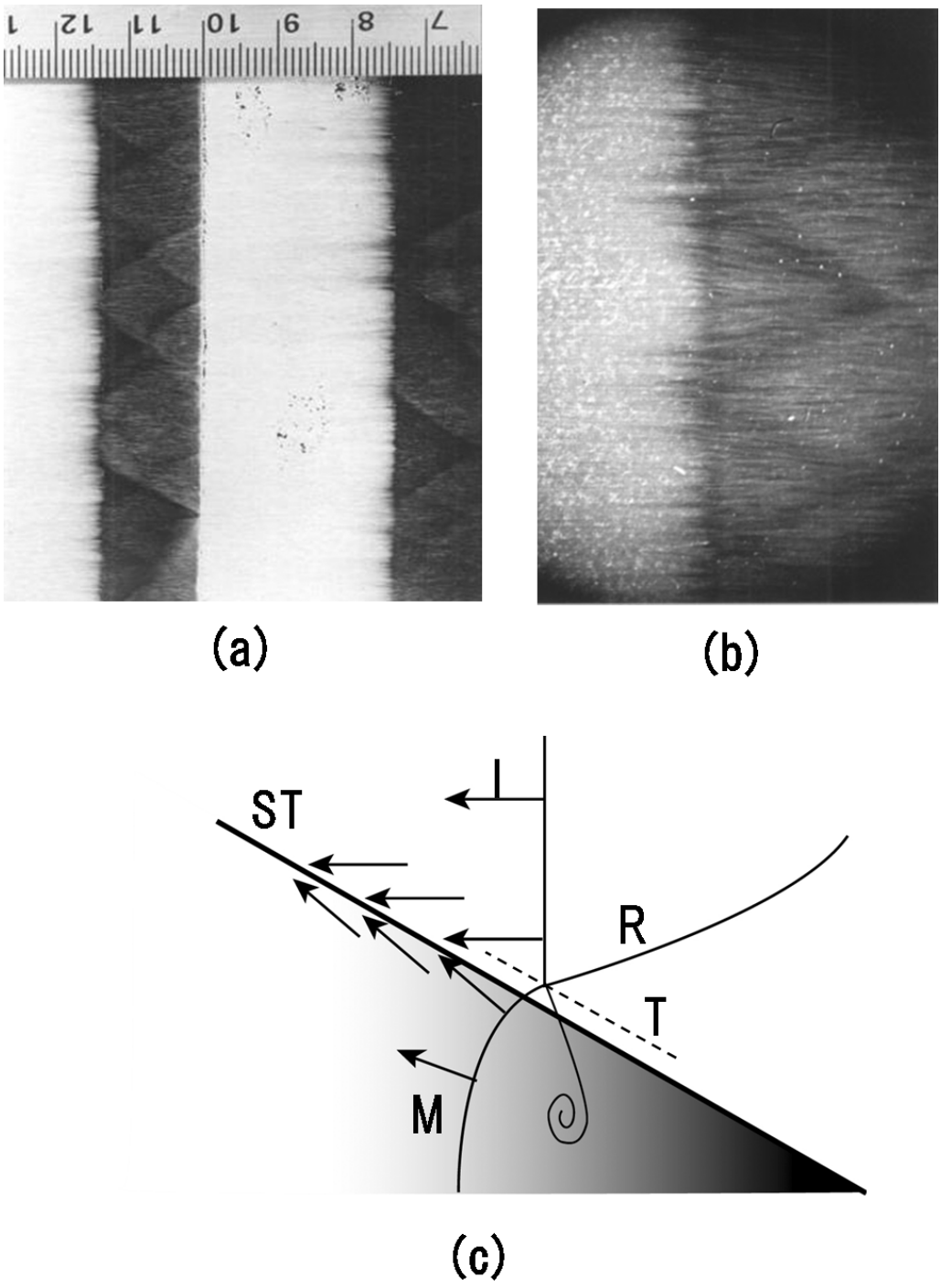

Figure 4.22: Detonation soot tracks and its formation mechanism. (a) Striped soot tracks. (b) Enlargement of (a) with microscope. (c) Schematic diagram of soot track formation. (M, Mach stem; I, Incident shock; R, Reflected shock; T, Trajectory of triple point; ST, Soot Track.)

pressure is normal to the surface and if the surface is very flat, there is no component along the surface even if there are large gradients.

The effect of a large pressure gradient, acting for a short time on the particle, is to create an impulse (integral of force with respect to time). The impulse causes the particles in the top layer of the soot surface to accelerate quickly and have a finite velocity after the shock has passed, if the impulse is sufficiently large to overcome the van der Waals forces that attract the soot particle to other soot particles. The simplest estimate of the maximum force will be the jump in pressure, across the shock, times the area of the particle. This can, at most, occur during the time it takes for the shock to pass over the particle, which is 25 ns. This gives an impulse which we can divide by the mass of the particle to get a velocity. If 50 μm is chosen as the particle size (this is the size of a clump of individual particles), then the velocity becomes 2.0 m/s. Because of the moment transfer to the adjacent particles, the actual velocity is much smaller.

Attraction of the other soot particles causes the top soot particle to transfer momentum to the particles below it. The top layer slows down and the bottom layers speed up. At the very bottom of the soot layer the particles are strongly attracted to the wall and not moving. The net effect is that the initial momentum imparted to the top layer of particles is diffused through the layer. A short distance behind the shock, the top layer of soot will be moving much slower than the 2.0 m/s estimate due to the initial impulse. Estimating the momentum in a layer one particle wide with a linear velocity profile (assumed in the fluid layer model) and equating this to the momentum of the single particle at the top of the layer, gives a computed reduction in the top layer velocity by $(h_{soot}/D_p)^2$ due to the momentum transfer. Thus, the equivalent surface velocity induced by the shock depends on the soot layer thickness. If the soot layer is 10 particles thick, then the velocity is only 0.02 m/s and the displacement in 1.0 ms (this is an upper bound on the time it takes for the reflected waves to reach the original location — the soot

tracks should be formed by then or else they will be destroyed) is only 0.02 mm — not enough to account for what is observed in the experiment with streaks that are 5–10 mm long.

4.5 Summary

Mach reflections over a wedge were investigated in experiments with soot foil records and in 3-D numerical simulations. The soot track angles obtained in experiments were slightly smaller than the theoretical and numerical triple-point track angles. It is for this reason that the soot tracks are piled up, being shifted from the trajectory of the triple point. Dark soot belts inside the Mach stem funnel were discovered in experiments for the single Mach reflection. It was proposed that the soot tracks were due to variations in the direction and magnitude of the shear stress created by the boundary layer adjacent to the soot foil. To verify this proposal, soot redistribution simulations were performed by modeling soot in the same manner as oil film and river sediment particles. Soot behind the incident shock was determined to be transported downward, due to the variation in the component of shear stress parallel to the shock front, and piled up with the soot behind the Mach stem, which resulted in the dark belt. Since detailed observation of striped soot foil records in detonations revealed the soot transport behavior, it was suggested that the same formation mechanism of soot tracks as the Mach reflections might be applicable to explain the soot track formation in detonations.

Chapter 5

Conclusions

The dynamics of cellular structures in gaseous detonations was investigated minutely in terms of aerothermochemistry and its derivation. Frontal instabilities of gaseous detonations were revealed to be the direct interactions between the shock front and the reaction front or passive interactions through compression waves in one-dimensional detonations. In Chapter 2, oscillation characteristics in one-dimensional oscillations depended fully on averaged post-shock pressures. In two-dimensional detonations, transverse wave properties in cellular structures were roughly classified as acoustic waves propagating behind the detonation front and discontinuous jumps accompanied by energy release. Moreover, it was revealed that the speed of sound behind the detonation front was important for propagation of detonation, concerning acoustic coupling between a sound wave and a frontal transverse wave. In Chapter 3, the mixture was assumed to be thermally perfect so the speed of sound and specific heat would be close to physical conditions. A study of transverse wave properties with a detailed reaction mechanism revealed that acoustic coupling was not dominant in the system diluted with nitrogen and lead to transverse wave intensity, a new quantitative tool to evaluate transverse waves. In Chapter 4, the mechanism of soot track formation based on shear stress variation was proposed and validated with experiments and numerical simulations. The following are the detailed results obtained in each chapter:

1) One-dimensional overdriven detonations and two-dimensional Chapman-Jouguet (C-J) detonations were successfully simulated with Korobeinikov's two-step reaction mechanism for stoichiometric hydrogen-air mixtures, initially at 42.7 kPa and 293 K. In one-dimensional detonations started from the steady solutions, high frequency, low frequency, and chaotic modes were observed with degree of overdrive. The simulation started by overdriving a quiescent combustible gas by a piston with a constant degree of overdrive also exhibited three oscillation modes, depending on the locally averaged post-shock pressures. At the same initial conditions, two-dimensional detonations were simulated to compare one-dimensional oscillations. The two-dimensional detonations were initiated by the initial energy release in blast initiation. Although two-dimensional detonations were initiated by a different method from the one-dimensional piston initiation, the transition in oscillation characteristics appeared in both detonations. Oscillation characteristics on the centerline profile of two-dimensional detonations were compared to one-dimensional detonations. Two-dimensional oscillation characteristics depended on the degree of overdrive against the frontal triple point in the narrow channel where the average velocities of transverse waves were less than the speed of sound at C-J conditions. Acoustic coupling of the frontal transverse wave and a sound wave propagating in a channel were examined by the ratio of the average velocity of the transverse wave to the speed of sound at C-J conditions. Detonation propagation with various channel widths indicated that if the detonation satisfied the acoustic coupling criterion, the detonation propagated stably in the channel.

2) Detonation simulations in various two-dimensional channels were performed with a stoichiometric hydrogen-oxygen detonation diluted with nitrogen or argon. The transverse wave strengths were defined as the dimensionless pressure increase across the reflected shock at the triple point. The maximum channel widths were determined by the channel width where a single

transverse wave appeared. The transverse wave strength was strongest at the maximum channel width. When a detonation propagated through a narrow channel, the shock structure showed the single and double Mach reflections (the ordinary behavior). In the mixture diluted with nitrogen at 0.101 MPa, the transverse wave strength increased up to values of marginal detonations with channel width. The flow feature showed the single, double, and complex Mach reflections (the marginal behavior). In both the hydrogen-air mixture at 0.013 MPa and the hydrogen-oxygen mixture diluted with argon at 0.101 MPa, the transverse wave strength did not increase beyond 0.85, but the flow features showed the complex Mach reflection. In the hydrogen-oxygen-argon mixture at 0.013 MPa, the transverse wave evolved up to the double Mach reflection, and the flow feature showed the ordinary behavior with transverse wave strength of values of ordinary detonations.

At the maximum channel width, the cell widths and aspect ratios showed comparatively good agreement with previous experimental data. Based on the acoustic coupling, average transverse wave velocities were specified by cell aspect ratios and C-J velocities. The ratio of average transverse wave velocity to speed of sound at C-J conditions varied from unity to 1.3 (mixture diluted with nitrogen at 0.101 MPa) at the maximum channel width. The strong transverse detonation occurred preferentially in the wide channel where the transverse wave propagated at high average velocity. When the post-shock conditions varied across the second explosion limit, strong transverse detonations appeared in the flow fields. These results lead us to conclude that empirical irregularities of a cell for the mixture diluted with nitrogen at 0.101 MPa were caused by the flexibility of the cell width due to the occurrence of the strong detonation and the instability due to the out-of-phase acoustic coupling.

3) Mach reflections over a wedge were investigated in experiments with soot foil records and in three-dimensional numerical simulations. The soot track angles obtained in experiments

were slightly smaller than the theoretical and numerical triple point track angles. The soot tracks would be piled up, being shifted from the trajectory of the triple point. Dark soot belts inside the Mach stem funnel were discovered in experiments for a single Mach reflection. The soot tracks were formed by variations in the direction and magnitude of the shear stress created by the boundary layer adjacent to the soot foil. To verify the proposal, the soot redistribution simulations were performed by modeling soot in the same way as oil film and sediment particles in rivers. It was concluded that the soot behind the incident shock was transported downward due to the variation of the component of shear stress parallel to the shock front and was piled up with the soot behind the Mach stem, which resulted in the dark belt. Since a detailed observation of striped soot foil records in detonations showed similar soot transport behavior, it was reasonable that the same formation mechanism of soot tracks as the Mach reflections could explain the detonation soot tracks.

Bibliography

Alpert, R. L. and T. Y. Toong (1972). Periodicity in exothermic hypersonic flow around blunt projectiles. *Astronaut. Acta 17*, 539–560.

Ames research staff (1953). Equations, tables and charts for compressible flow. Rep. 1135, NACA.

Arienti, M. (2002). *A numerical and analytical study of detonation diffraction*. Ph.D. dissertation, California Institute of Technology.

Austin, J. M. and J. E. Shepherd (2003). Detonations in hydrocarbon fuel blends. *Combust. Flame 132*, 73–90.

Barthel, H. O. (1986). Predicted spacings in hydrogen-oxygen-argon detonations. *Phys. Fluids 106*, 263–293.

Baurle, R. A. and D. R. Eklund (2002). Analysis of dual-mode hydrocarbon scramjet operation at Mach 4–6.5. *AIAA J. Prop. Power 18*, 990–1002.

Ben-Dor, G. (1991). *Shock wave reflection phenomena*. Springer-Verlag, New York.

Bourlioux, A. and A. J. Majda (1992). Theoretical and numerical structure for unstable two-dimensional detonations. *Combust. Flame 90*, 211–229.

Bourlioux, A. and A. J. Majda (1995). Theoretical and numerical structure of unstable detonations. *R. Soc. Lond. A 350*, 29–68.

Bourlioux, A., A. J. Majda, and V. Roytburd (1991). Theoretical and numerical structure for

unstable one-dimensional detonations. *SIAM J. Appl. Math. 51*, 303–343.

Bull, D. C., J. E. Elsworth, and P. J. Shuff (1982). Detonation cell structures in fuel/air mixtures. *Combust. Flame 45*, 7–22.

Chang, H. H. (1988). *Fluvial process in river engineering*. Krieger publishing company, Florida.

Chisnell, R. F. (1957). The motion of a shock wave in a channel with applications to cylindrical and spherical shock waves. *J. Fluid Mech. 2*, 286–298.

Clavin, P. and L. He (1996). Stability and nonlinear dynamics of one-dimensional overdriven detonation in gases. *J. Fluid Mech. 306*, 353–378.

Collela, P. and L. F. Henderson (1990). The von Neumann paradox for the diffraction of weak shock waves. *J. Fluid Mech. 213*, 71–94.

Daimon, Y. and A. Matsuo (2003). Detailed features of one-dimensional detonations. *Phys. Fluids 15*, 112–122.

Eckett, C. A. (2001). *Numerical and analytical studies of the dynamics of gaseous detonations*. Ph.D. dissertation, California Institute of Technology.

Edwards, D. H., G. Hooper, E. M. Job, and D. J. Parry (1970). The behavior of the frontal and transverse shocks in gaseous detonation waves. *Astronaut. Acta 15*, 323–333.

Edwards, D. H., G. O. Thomas, and M. A. Nettleton (1979). The diffraction of a planar detonation wave at an abrupt area change. *J. Fluid Mech. 95*, 79–96.

Erpenbeck, J. J. (1964). Stability of idealized one-reaction detonations. *Phys. Fluids 7*, 684–694.

Fickett, W. and W. C. Davis (1979). *Detonation*. University of California Press.

Fickett, W., J. D. Jacobson, and G. L. Schott (1972). Calculated pulsating one-dimensional detonations with induction-zone kinetics. *AIAA J. 105*, 514–516.

Fletcher, B. (1976). The interaction of a shock with a dust deposit. *J. Phys. D: Appl. Phys. 9*, 197–202.

Gamezo, V. N., D. Desbordes, and E. S. Oran (1999a). Formation and evolution of two-dimensional cellular detonations. *Combust. Flame 116*, 154–165.

Gamezo, V. N., D. Desbordes, and E. S. Oran (1999b). Two-dimensional reactive flow dynamics in cellular detonation waves. *Shock Waves 9*, 11–17.

Gamezo, V. N., A. A. Vasil'ev, A. M. Khokhlov, and E. S. Oran (2000). Fine cellular structures produced by marginal detonations. In *28th Symp. (Intl.) on Combustion*, pp. 611–617.

Gardiner, Jr., W. C. (1984). *Combustion Chemistry*. Springer-Verlag, New York.

Gavrikov, A. I., A. A. Efimenko, and S. B. Dorofeev (2000). A model for detonation cell size prediction from chemical kinetics. *Combust. Flame 120*, 19–33.

Hanana, M., M. H. Lefebvre, and P. J. Van Tiggelen (2001). Pressure profiles in detonation cells with rectangular and diagonal structures. *Shock Waves 11*, 77–88.

He, L. and J. H. S. Lee (1995). The dynamical limit of one-dimensional detonations. *Phys. Fluids 7*, 1151–1158.

Henderson, C. B. (1976). Drag coefficients of spheres in continuum and rarefied flows. *AIAA J. 14*, 707–708.

Hornung, H. (1996). Regular and Mach reflection of shock waves. *Ann. Rev. Fluid Mech. 18*, 33–58.

Howarth, L. (1948). Concerning the effect of compressibility on laminar boundary layers and

their separation. *Proc. Roy. Soc. Lond. A 194*, 16–42.

Hunter, J. K. and M. Brio (2000). Weak shock reflection. *J. Fluid Mech. 410*, 235–261.

Igra, O. and K. Takayama (1993). Shock tube study of the drag coefficient of a sphere in a non-stationary flow. *Proc. R. Soc. Lond. A 442*, 231–247.

Jachimowski, C. J. (1988). An analytical study of the hydrogen-air reaction mechanism with application to scramjet combustion. TP 2791, NASA.

Johnston, J. P. (1960). On the three-dimensional turbulent boundary layer generated by secondary flow. *J. Basic Eng. 82*, 233–248.

Kailasanath, K. (2000). Review of propulsion applications of detonation waves. *AIAA J. 38*, 1698–1708.

Kailasanath, K., E. S. Oran, J. P. Boris, and T. R. Young (1985). Determination of detonation cell size and the role of transverse waves in two-dimensional detonations. *Combust. Flame 61*, 199–209.

Kamiyama, Y. and A. Matsuo (2000). Flow features of shock-induced combustion around cylindrical projectiles. In *28th Symp. (Intl.) on Combustion*, pp. 671–677. The Combustion Institute.

Kasahara, J., T. Horii, T. Endo, and T. Fujiwara (1997). Unsteady combustion and oblique detonation induced by hypersonic projectiles flying in hydrogen-air mixtures. *Journal of the Japan Society for Aeronautical and Space Sciences 45*, 102–109.

Kasahara, J., K. Takazawa, T. Arai, Y. Tanahashi, S. Chiba, and A. Matsuo (2002). Experimental investigations of momentum and heat transfers on pulse detonation engines. In *29th Symp. (Intl.) on Combustion*, pp. 2847–2854. The Combustion Institute.

Knystautas, R., J. H. S. Lee, and C. M. Guirao (1982). The critical tube diameter for detona-

tion failure in hydrocarbon-air mixtures. *Combust. Flame 48*, 63–83.

Korobeinikov, V. P., V. A. Levin, V. V. Markov, and G. G. Cher (1972). Propagation of blast waves in a combustible gas. *Astronaut. Acta 17*, 529–537.

Krehl, P. and M. V. D. Geest (1991). The discovery of the Mach reflection effect and its demonstration in an auditorium. *Shock Waves 1*, 3–15.

Kumar, R. K. (1990). Detonation cell widths in hydrogen-oxygen-diluent mixtures. *Combust. Flame 80*, 157–169.

Lee, J. H. S. (1977). Initiation of gaseous detonation. *Ann. Rev. Phys. Chem. 28*, 75–104.

Lee, J. H. S. (1984). Dynamic parameters of gaseous detonations. *Ann. Rev. Fluid Mech. 16*, 311–336.

Lefebvre, M. H. and E. S. Oran (1995). Analysis of the shock structures in a regular detonation. *Shock Waves 4*, 277–283.

Lefebvre, M. H., E. S. Oran, K. Kailasanath, and P. J. Van Tiggelen (1993). The influence of the heat capacity and diluent on detonation structure. *Combust. Flame 95*, 206–218.

Lehr, H. F. (1972). Experiments on shock-induced combustion. *Astronaut. Acta 17*, 589–597.

Leopold, L. B., M. G. Wolman, and J. P. Miller (1995). *Fluvial processes in geomorphology*. Dover publications, Inc. New York., Chap. 6.

MacCormack, R. W. (1971). Numerical solution of the interaction of a shock wave with a laminar boundary layer. In *Lecture Notes in Physics*, pp. 151–163. Springer-Verlag.

Mader, C. L. (1998). *Numerical Modeling of Explosives and Propellants, Second Edition*. CRC Press.

Matsuo, A. and K. Fujii (1995). Computational study of large-disturbance oscillations in unsteady supersonic combustion around projectiles. *AIAA J. 33*, 1828–1835.

Matsuo, A. and K. Fujii (1996). Detailed mechanism of the unsteady combustion around hypersonic projectiles. *AIAA J. 34*, 2082–2089.

Matsuo, A. and K. Fujii (1997). Numerical investigation of the one-dimensional piston supported detonation waves. *Energy Convers. Mgmt 38*, 1283–1295.

Matsuo, A. and K. Fujii (1998). Prediction method of unsteady combustion around hypersonic projectile in stoichiometric hydrogen-air. *AIAA J. 36*, 1834–1841.

Matsuo, A., K. Fujii, and T. Fujiwara (1995). Flow features of shock-induced combustion around projectile traveling at hypervelocities. *AIAA J. 33*, 1056–1063.

Matsuo, A. and T. Fujiwara (1993). Numerical investigation of oscillatory instability in shock-induced combustion around a blunt body. *AIAA J. 31*, 1835–1841.

McVey, J. B. and T. Y. Toong (1971). Mechanism of instabilities of exothermic hypersonic blunt-body flow. *Combust. Sci. Technol. 3*, 63–76.

Mirels, H. (1963). Test time in low-pressure shock tubes. *Phys. Fluids 6*, 1201–1214.

Mirels, H. (1966a). Correlation formulas for laminar shock tube boundary layer. *Phys. Fluids 9*, 1265–1272.

Mirels, H. (1966b). Series solutions for shock-tube laminar boundary layer and test time. *AIAA J. 4*, 782–789.

National Astronomical Observatory of Japan (ed.) (2003). *Rika nenpyo (Chronological Scientific Tables)*. Maruzen Co., Ltd.

Ng, H. D. and J. H. S. Lee (2003). Direct initiation of detonation with a multi-step reaction scheme. *J. Fluid Mech. 476*, 179–211.

Olim, M. and J. M. Dewey (1992). A revised three-shock solution for the Mach reflection of weak shocks ($1.1 < m_i < 1.5$). *Shock Waves 2*, 167–176.

Oran, E. S., J. W. Weber, Jr., E. I. Stefaniw, M. H. Lefebvre, and J. D. Anderson, Jr. (1998). A numerical study of a two-dimensional H_2-O_2-Ar detonation using a detailed chemical reaction model. *Combust. Flame 113*, 147–163.

Otani, Y., H. Emi, T. Morizane, and J. Mori (1993). Removal of fine particles from wafer surface by pulse air jets. *Kagaku Kogaku Ronbunshu 19*, 114–119.

Pintgen, F., C. A. Eckett, J. M. Austin, and J. E. Shepherd (2003). Direct observations of reaction zone structure in propagating detonations. *Combust. Flame 133*, 211–229.

Pintgen, F. and J. E. Shepherd (2003). Simultaneous soot foil and PLIF imaging of propagating detonations. In *19th ICDERS*.

Radulescu, M. I., G. J. Sharpe, J. H. S. Lee, C. B. Kiyanda, A. J. Higgins, and R. K. Hanson (2004). The ignition mechanism in irregular structure gaseous detonations. In *30th Symp. (Intl.) on Combustion*, pp. (in pres).

Reynolds, W. C. (1986). The element potential method for chemical equilibrium analysis: Implementation in the interactive program STANJAN. Technical report, Stanford University, Dept. of Mech. Engng.

Roache, P. J. (1997). Quantification of uncertainty in computational fluid dynamics. *Ann. Rev. Fluid Mech. 29*, 123–160.

Sánchez, A. L., M. Carretero, P. Clavin, and F. A. Williams (2001). One-dimensional overdriven detonations with branched-chain kinetics. *Phys. Fluids 13*, 776–792.

Sasoh, A. and K. Takayama (1994). Characterization of disturbance propagation in weak shock-wave reflections. *J. Fluid Mech. 277*, 331–345.

Sasoh, A., K. Takayama, and T. Saito (1992). A weak shock wave reflection over wedges. *Shock Waves 2*, 277–281.

Sharpe, G. J. (2001a). Numerical simulations of pulsating detonations: II. piston initiated detonations. *Combust. Theory Modeling 7*, 401–416.

Sharpe, G. J. (2001b). Transverse waves in numerical simulations of cellular detonations. *J. Fluid Mech. 4*, 557–574.

Sharpe, G. J. and S. A. E. G. Falle (2000a). Numerical simulations of pulsating detonations: I. nonlinear stability of steady detonations. *Combust. Theory Modeling 4*, 557–574.

Sharpe, G. J. and S. A. E. G. Falle (2000b). Two-dimensional numerical simulations of idealized detonations. *Proc. Roy. Soc. Lond. A 456*, 2081–2100.

Shepherd, J. E. (1986). Chemical kinetics of hydrogen-air-diluent detonations. *Prog. Astronaut. Aeronaut. 106*, 263–293.

Singh, D. J. and C. J. Jachimowski (1994). Quasiglobal reaction model for ethylene combustion. *J. AIAA 32*, 213–215.

Smedley, G. T., D. J. Phares, and R. C. Flagan (1999). Entrainment of fine particles from surfaces by impinging shock waves. *Experiments in Fluids 26*, 116–125.

Soloukhin, R. I. (1966). Multiheaded structure of gaseous detonation. *Combust. Flame 10*, 51–58.

Squire, L. C. (1962). The motion of a thin oil sheet under the boundary layer on a body. *AGARDograph 70*, 7–28.

Stamps, D. W. and S. R. Tieszen (1991). The influence of initial pressure and temperature on hydrogen-air-diluent detonations. *Combust. Flame 83*, 353–364.

Strehlow, R. A. (1968). *Fundamentals of Combustion*. International Textbook Company.

Strehlow, R. A. (1970). Multi-dimensional detonation wave structure. *Astronaut. Acta 17*, 345–357.

Strehlow, R. A. and J. R. Biller (1969). On the strength of transverse waves in gaseous detonation. *Combust. Flame 13*, 577–582.

Strehlow, R. A. and A. J. Crooker (1974). The structure of marginal detonation waves. *Acta Astronautica 1*, 303–315.

Strehlow, R. A. and C. D. Engel (1969). Transverse waves in detonations: II. Structure and spacing in H_2-O_2, C_2H_2-O_2, CH_4-O_2 systems. *AIAA J. 7*, 492–496.

Strehlow, R. A., R. Liaugminas, R. H. Watson, and J. R. Eyman (1967). Transverse wave structure in detonations. In *11th Symp. (Intl.) on Combustion*, pp. 683–692.

Strehlow, R. A., R. E. Maurer, and S. Rajan (1969). Transverse waves in detonations: I. Spacing in the hydrogen-oxygen system. *AIAA J. 7*, 323–328.

Sturtevant, B. and T. T. Okamura (1969). Dependence of shock-tube boundary layers on shock strength. *Phys. Fluids 12*, 1723–1725.

Sussman, M. A. (1994). *Numerical simulation of shock induced combustion*. Ph.D. dissertation, Stanford University.

Suzuki, T., Y. Sakamura, T. Adachi, and S. Kobayashi (1995). An experimental study on the initial mechanism of particle liftup by a shock passage. *Trans. Jpn. Soc. Aero. Space Sci. 38*, 243–250.

Takai, R., K. Yoneda, and T. Hikita (1974). Study of detonation wave structure. In *15th Symp. (Intl.) on Combustion*, pp. 69–78.

Taki, S. and T. Fujiwara (1978). Numerical analysis of two-dimensional nonsteady detonations. *AIAA J. 16*, 73–77.

Tanaka, K. (1985). Detonation properties of high explosives calculated by revised Kihara-Hikita equation of state. In *8th Symp. (Intl.) on Detonation*, pp. 548–557. NSWC MP

86-194.

Tanner, L. H. and L. G. Blows (1976). A study of the motion of oil films on surfaces in air flow, with application to the measurement of skin friction. *J. Phys. E: Sci. Instrum. 9*, 194–202.

Terao, K. and T. Azumatei (1989). Cellular pattern formation in detonation waves as a stochastic phenomenon. *Jpn. J. Appl. Phys. 28*, 723–728.

Toong, T. Y. (1983). *Combustion Dynamics*. McGraw-Hill Book Company.

Urtiew, P. A. (1970). Reflections of wave intersections in marginal detonations. *Astronaut. Acta 15*, 335–343.

Voebodsky, V. V. and R. I. Soloukhin (1965). On the mechanism and explosion limits of hydrogen-oxygen chain self-ignition in shock waves. In *10th Symp. (Intl.) on Combustion*, pp. 279–283.

Warnatz, J., U. Maas, and R. W. Dibble (2001). *Combustion: Physical and Chemical Fundamentals, Modeling and Simulation, Experiments, Pollutant Formation, 3rd ed.* Springer-Verlag, Berlin/Heidelberg/New York.

Westbrook, C. (1982). Chemical kinetics of hydrocarbon oxidation in gaseous detonations. *Combust. Flame 46*, 191–210.

White, F. M. (1991). *Viscous Fluid Flow 2nd ed.* McGraw-Hill.

Whitham, G. B. (1957). A new approach to problems of shock dynamics. part 1. two-dimensional problems. *J. Fluid Mech. 2*, 145–171.

Williams, D. N., L. Bauwens, and E. S. Oran (1996). A numerical study of the mechanisms of self-reignition in low-overdrive detonations. *Shock Waves 6*, 93–110.

Wilson, G. J. and R. W. MacCormack (1992). Modeling supersonic combustion using a

fully-implicit numerical method. *AIAA J. 30*, 1008–1015.

Yee, H. C. (1987). Upwind and symmetric shock capturing schemes. TM 89464, NASA.

Zakhaeian, A. R., M. Brio, J. K. Hunter, and G. M. Webb (2000). The von Neumann paradox in weak shock reflection. *J. Fluid Mech. 422*, 193–205.

Appendix A

Modified Jachimowski H_2-O_2 Reaction Mechanism

Table A.1: Modified Jachimowski's reaction mechanism for H_2-Air systems, from Wilson & MacCormack (1992). $k_{f_l} = A_l T^{n_l} \exp(-E_l/RT)$ (cm^3-s-mol-cal-K).

	Reaction	A_l	n_l	E_l
1.	$H_2 + O_2 = HO_2 + H$	1.00e+14	0.	56000
2.	$H + O_2 = OH + O$	2.60e+14	0.	16800
3.	$O + H_2 = OH + H$	1.80e+10	1.	8900
4.	$OH + H_2 = H + H_2O$	2.20e+13	0.	5150
5.	$OH + OH = O + H_2O$	6.30e+12	0.	1090
6.	$H + OH + M = H_2O + M$	2.20e+22	-2.	0
7.	$H + H + M = H_2 + M$	6.40e+17	-1.	0
8.	$H + O + M = OH + M$	6.00e+16	-0.6	0
9.	$H + O_2 + M = HO_2 + M$	2.10e+15	0.	-1000
10.	$O + O + M = O_2 + M$	6.00e+13	0.	-1800
11.	$HO_2 + H = OH + OH$	1.40e+14	0.	1080
12.	$HO_2 + H = H_2O + O$	1.00e+13	0.	1080
13.	$HO_2 + O = O_2 + OH$	1.50e+13	0.	950
14.	$HO_2 + OH = H_2O + O_2$	8.00e+12	0.	0
15.	$HO_2 + HO_2 = H_2O_2 + O_2$	2.00e+12	0.	0
16.	$H + H_2O_2 = H_2 + HO_2$	1.40e+12	0.	3600
17.	$O + H_2O_2 = OH + HO_2$	1.40e+13	0.	6400
18.	$OH + H_2O_2 = H_2O + HO_2$	6.10e+12	0.	1430
19.	$H_2O_2 + M = OH + OH + M$	1.20e+17	0.	45500

Enhanced third-body efficiencies for three-body reactions: Reaction 6, H_2O = 6.0; Reaction 7, H_2O = 6.0, H_2 = 2.0; Reaction 8, H_2O = 5.0; Reaction 9, H_2O = 16.0, H_2 = 2.0; Reaction 19, H_2O = 15.0.

Appendix B

Molecular Constants

This appendix gives the molecular constants and thermochemical data used for the ten species present in the hydrogen-oxygen-nitrogen/argon gas model. The molecular constants for each of the ten species are found in Table B.1. The source of thermochemical data is NASA polynomials from Appendix C of Gardiner (1984) which have the following form for each species

$$\frac{C^{\circ}_{p,i}}{R_i} = a_{1i} + a_{2i}T + a_{3i}T^2 + a_{4i}T^3 + a_{5i}T^4, \tag{B.1}$$

$$\frac{H^{\circ}_i}{R_i T} = a_{1i} + \frac{a_{2i}}{2}T + \frac{a_{3i}}{3}T^2 + \frac{a_{4i}}{4}T^3 + \frac{a_{5i}}{5}T^4 + \frac{a_{6i}}{T}, \tag{B.2}$$

$$\frac{S^{\circ}_i}{R_i} = a_{1i}\ln T + a_{2i}T + \frac{a_{3i}}{2}T^2 + \frac{a_{4i}}{3}T^3 + \frac{a_{5i}}{4}T^4 + a_{7i}, \tag{B.3}$$

where the superscript on the enthalpy H° and the entropy S° are for a reference state of one atmosphere. The coefficients for these curve fits are found in Table B.2. There is one set of coefficients for the temperature range 300 K to 1000 K and another for the temperature range 1000 K to 5000 K. The enthalpy H° includes the enthalpy of formation.

Table B.1: Molecular weight of species W_i (kg/kmol).

H_2	O_2	H	O	OH	H_2O	HO_2	H_2O_2	N_2	Ar
2.0159	31.9988	1.0079	15.9994	17.0073	18.0153	33.0067	34.0147	28.0134	39.9480

Table B.2: NASA thermochemical polynomials.

Temperature Range 300K to 1000K							
species	a_1	a_2	a_3	a_4	a_5	a_6	a_7
H_2	0.33553514e+01	0.50136144e-03	-0.23006908e-06	-0.47905324e-09	0.48522585e-12	-0.10191626e+04	-0.35477228e+01
O_2	0.37837135e+01	-0.30233634e-02	0.99492751e-05	-0.98189101e-08	0.33031825e-11	-0.10638107e+04	0.36416345e+01
H	0.25000000e+01	0.0	0.0	0.0	0.0	0.25471627e+05	-0.46011762e+00
O	0.30309401e+01	-0.22525853e-02	0.39824540e-05	-0.32604921e-08	0.10152035e-11	.29136526e+05	.26099342e+01
OH	0.38737300e+01	-0.13393772e-02	0.16348351e-05	-0.52133639e-09	0.41826974e-13	0.35802348e+04	0.34202406e+00
H_2O	0.41677234e+01	-0.18114970e-02	0.59471288e-05	-0.48692021e-08	0.15291991e-11	-0.30289969e+05	-0.73135474e+00
HO_2	0.35964102e+01	0.52500748e-03	0.75118344e-05	-0.95674952e-08	0.36597628e-11	-0.89333502e+03	0.66372671e+01
H_2O_2	0.33887536e+01	0.65692260e-02	-0.14850126e-06	-0.46258055e-08	0.24715147e-11	-0.17663147e+05	0.67853631e+01
N_2	0.37044177e+01	-0.14218753e-02	0.28670392e-05	-0.12028885e-08	-0.13954677e-13	-0.10640795e+04	0.22336285e+01
Ar	0.25000000e+01	0.0	0.0	0.0	0.0	-0.74537500e+03	0.43660000e+01
Temperature Range 1000K to 5000K							
species	a_1	a_2	a_3	a_4	a_5	a_6	a_7
H_2	0.30667095e+01	0.57473755e-03	0.13938319e-07	-0.25483518e-10	0.29098574e-14	-0.86547412e+03	-0.17798424e+01
O_2	0.36122139e+01	0.74853166e-03	-0.19820647e-06	0.33749008e-10	-0.23907374e-14	-0.11978151e+04	0.36703307e+01
H	0.25000000e+01	0.0	0.0	0.0	0.0	0.25471627e+05	-0.46011762e+00
O	0.25342961e+01	-0.12478170e-04	-0.12562724e-07	0.69029862e-11	-0.63797095e-15	0.29231108e+05	0.49628591e+01
OH	0.28897814e+01	0.10005879e-02	-0.22048807e-06	0.20191288e-10	-0.39409831e-15	0.38857042e+04	0.55566427e+01
H_2O	0.26110472e+01	0.31563130e-02	-0.92985438e-06	0.13331538e-09	-0.74689351e-14	-0.29868167e+05	0.72091268e+01
HO_2	0.40173060e+01	0.22175883e-02	-0.57710171e-06	0.71372882e-10	-0.36458591e-14	-0.11412445e+04	0.37846051e+01
H_2O_2	0.45731667e+01	0.43361363e-02	-0.14746888e-05	0.23489037e-09	-0.14316536e-13	-0.18006961e+05	0.50113696e+00
N_2	0.28532899e+01	0.16022128e-02	-0.62936893e-06	0.11441022e-09	-0.78057465e-14	-0.89008093e+03	0.63964897e+01
Ar	0.25000000e+01	0.0	0.0	0.0	0.0	-0.74537500e+03	0.43660000e+01

Appendix C

Chemical Source Term for the Equations of Species

The general form of each chemical reaction can be written as

$$\sum_{i=1}^{N} \nu'_{ik}\chi_i \Leftrightarrow \sum_{i=1}^{N} \nu''_{ik}\chi_i, \tag{C.1}$$

where χ represents species and ν'' and ν' are the stoichiometric coefficients of the reactant and products for each chemical reaction k. The source terms for the different species equations i can be written

$$\omega_i = W_i \sum_{k=1}^{N} (\nu''_{ik} - \nu'_{ik})\, RP_k. \tag{C.2}$$

Note that $\sum_{i=1}^{N} \omega_i = 0$ satisfies overall mass conservation. The RP_k indicates the rate of progress variable of chemical reaction k and is given as

$$RP_k = k_{f,k} \prod_{i=1}^{N} (c_{\chi i})^{\nu'_{ik}} - k_{b,k} \prod_{i=1}^{N} (c_{\chi i})^{\nu''_{ik}}, \tag{C.3}$$

where $c_{\chi i}$ is mole concentration of species i, and $k_{f,k}$ and $k_{b,k}$ are the forward and backward rate constant of reaction k. The forward rate constants $k_{f,k}$ for each reaction k are given by the extended Arrhenius expression

$$k_{f,k} = A_k T^{nk} \exp\left(-\frac{E_{ak}}{RT}\right), \tag{C.4}$$

where T is the temperature and A_k, n_k, and E_k are constants found in the reaction mechanism in Table A. The backward rate constants $k_{b,k}$ are calculated using the equilibrium constant Kc_k for

each reaction and the relation

$$k_{b,k} = \frac{k_{f,k}}{Kc_k}. \tag{C.5}$$

The equilibrium constant Kc_k is related to the pressure equilibrium constants as

$$Kc_k = Kp_k \left(\frac{P_{atm}}{R_u T}\right)^{\sum_{i=1}^{N}\left(\nu''_{ik}-\nu'_{ik}\right)}, \tag{C.6}$$

where P_{atm} = 1(atm) and R_u is the universal gas constant. The pressure equilibrium constant Kp_k is calculated using the enthalpy and the standard state entropy as

$$Kp_k = \exp\left[\sum_{i=1}^{N}\left\{(\nu''_{ik}-\nu'_{ik})\frac{s_i^\circ}{R_i}\right\} - \sum_{i=1}^{N}\left\{(\nu''_{ik}-\nu'_{ik})\frac{h_i}{R_i T}\right\}\right]. \tag{C.7}$$

If the third-body efficiency is considered in chemical reactions, the rate of progress variable is given as

$$RP_k = \left\{\sum_{i=1}^{N}(\alpha_{ik}c_{\chi i})\right\}\left\{k_{f,k}\prod_{i=1}^{N}(c_{\chi i})^{\nu'_{ik}} - k_{b,k}\prod_{i=1}^{N}(c_{\chi i})^{\nu''_{ik}}\right\}. \tag{C.8}$$

The α_{ik} is the third efficiency factor for reaction k and is described in Table A.1. The equation of state for pressure is given by the Dalton's law for a mixture of thermally perfect gases,

$$P = \sum_{i=1}^{N}\frac{\rho_i}{W_i}R_u T, \tag{C.9}$$

where W_i is the molecular weight of species i.

Appendix D

Point-Implicit Finite Difference Scheme

The governed equations are solved by a finite difference method and the unsteady solutions are obtained at each time-step through the time marching procedure. The non-MUSCL type TVD upwind algorithm developed by Yee (1987) is used in the present simulations. This algorithm is second-order in time and space for the system of equations.

The point-implicit finite difference scheme of equation (3.1) is written as:

$$\mathbf{D}^n_{j,k}\Delta\mathbf{U}_{j,k} = -\frac{\Delta t}{\Delta x}\left(\tilde{\mathbf{F}}^n_{j+1/2,k} - \tilde{\mathbf{F}}^n_{j-1/2,k}\right) - \frac{\Delta t}{\Delta y}\left(\tilde{\mathbf{G}}^n_{j,k+1/2} - \tilde{\mathbf{G}}^n_{j,k-1/2}\right) + \Delta t\mathbf{S}^n_{j,k}, \tag{D.1}$$

$$\mathbf{U}^{n+1}_{j,k} = \mathbf{U}^n_{j,k} + \Delta\mathbf{U}_{j,k}, \tag{D.2}$$

$$\mathbf{D}^n_{j,k} = \left(\mathbf{I} - \frac{\Delta t}{2}\frac{\partial\mathbf{S}}{\partial\mathbf{U}}\right)^n_{j,k}, \tag{D.3}$$

where the approximations are referred to as ”point-implicit” because all convection terms are evaluated at the time n, whereas the source term of the chemical reactions is evaluated at the time $n+1$. The Jacobian of the chemical source term $\partial\mathbf{S}/\partial\mathbf{U}$ in eq. (D.3) is written in Appendix E.

The functions $\tilde{\mathbf{F}}_{j+1/2,k}$ and $\tilde{\mathbf{G}}_{j,k+1/2}$ are the numerical fluxes in the $\xi-$ and $\eta-$axes evaluated at $(j+1/2,k)$ and $(j,k+1/2)$, respectively. Typically, $\tilde{\mathbf{F}}_{j+1/2,k}$ for a non-MUSCL TVD algorithm can be expressed as:

$$\tilde{\mathbf{F}}_{j+1/2,k} = \frac{1}{2}\left(\hat{\mathbf{F}}_{j,k} + \hat{\mathbf{F}}_{j+1,k} + \mathbf{R}_{j+1/2,k}\mathbf{\Phi}_{j+1/2,k}\right), \tag{D.4}$$

where $\mathbf{R}_{j+1/2,k}$ is the matrix whose columns are right eigenvectors of flux Jacobian $\partial\hat{\mathbf{F}}\big/\partial\hat{\mathbf{U}}$. The elements of the vector $\mathbf{\Phi}_{j+1/2,k}$ for a second-order upwind TVD scheme, denoted by $\left(\phi^l_{j+1/2}\right)^{\mathbf{U}}$,

are

$$\left(\phi^l_{j+1/2}\right)^{\mathbf{U}} = \sigma\left(a^l_{j+1/2}\right)\left(g^l_{j+1} + g^l_j\right) - \psi\left(a^l_{j+1/2} + \gamma^l_{j+1/2}\right)\alpha^l_{j+1/2}, \tag{D.5}$$

where $a^l_{j+1/2}$is the l-th eigenvalue of $\partial\hat{\mathbf{F}}\big/\partial\hat{\mathbf{U}}$ and $\alpha^l_{j+1/2}$ is the difference vector of the characteristic variables in the local $\xi-$direction denoted, for example, as

$$\alpha^l_{j+1/2} = \left(\mathbf{R}^{-1}_{j+1/2}\right)^l\left(\hat{\mathbf{U}}^l_{j+1} - \hat{\mathbf{U}}^l_j\right). \tag{D.6}$$

The $\psi(z)$ is an entropy correction function that is expressed as:

$$\psi(z) = \begin{cases} |z| & |z| \geq \delta_1 \\ \left(z^2 + \delta_1^2\right)\big/2\delta_1 & |z| < \delta_1 \end{cases}, \tag{D.7}$$

and the functions $\sigma(z)$ and $\gamma^l_{j+1/2}$ are expressed as:

$$\sigma(z) = \frac{1}{2}\left[\psi(z) - \frac{\Delta t}{\Delta x}z^2\right] \tag{D.8}$$

$$\gamma^l_{j+1/2} = \sigma^l_{j+1/2}\begin{cases} \left(g^l_{j+1} - g^l_j\right)\big/\alpha^l_{j+1/2} & \alpha^l_{j+1/2} \neq 0 \\ 0 & \alpha^l_{j+1/2} = 0 \end{cases}. \tag{D.9}$$

The function δ_1 defines the range of entropy correction and should be a function of the contravariant velocity and the corresponding speed of sound for simulations. The form of the function used here is

$$\delta_1 = \tilde{\delta}\left(|U| + |V| + c\sqrt{\xi_x^2 + \xi_y^2 + \eta_x^2 + \eta_y^2}\right) \tag{D.10}$$

with a constant $\tilde{\delta}$ setting from 0.1 to 0.15.

Several types of the form of the limiter functions are suggested by Yee (1987). In the present study, the following limiter functions are used:

$$g^l_j = \text{minmod}\left(\alpha^l_{j+1/2}, \alpha^l_{j-1/2}\right), \tag{D.11}$$

where the minmod functions are given as:

$$\min\text{mod}(x, y) = \text{sgn}(x)\cdot\max\{0, [|x|, y\cdot\text{sgn}(x)]\}. \tag{D.12}$$

Appendix E

Jacobian of Chemical Source Term for the Equations of Species

The chemical reaction source term vector S is described in eq. (3.1). The $\partial S/\partial U$ in eq. (D.3) for the equations of species is written as follows:

$$\frac{\partial \mathbf{S}}{\partial \mathbf{U}} = \begin{bmatrix} 0 & 0 & 0 & 0 & 0 & \cdots & 0 & \cdots & 0 \\ 0 & 0 & 0 & 0 & 0 & \cdots & 0 & \cdots & 0 \\ 0 & 0 & 0 & 0 & 0 & \cdots & 0 & \cdots & 0 \\ 0 & 0 & 0 & 0 & 0 & \cdots & 0 & \cdots & 0 \\ \frac{\partial \omega_1}{\partial \rho} & \frac{\partial \omega_1}{\partial (\rho u)} & \frac{\partial \omega_1}{\partial (\rho v)} & \frac{\partial \omega_1}{\partial E} & \frac{\partial \omega_1}{\partial \rho_1} & \cdots & \frac{\partial \omega_1}{\partial \rho_i} & \cdots & \frac{\partial \omega_1}{\partial \rho_N} \\ \vdots & \vdots & \vdots & \vdots & \vdots & & \vdots & & \vdots \\ \frac{\partial \omega_i}{\partial \rho} & \frac{\partial \omega_i}{\partial (\rho u)} & \frac{\partial \omega_i}{\partial (\rho v)} & \frac{\partial \omega_i}{\partial E} & \frac{\partial \omega_i}{\partial \rho_1} & \cdots & \frac{\partial \omega_i}{\partial \rho_j} & \cdots & \frac{\partial \omega_i}{\partial \rho_N} \\ \vdots & \vdots & \vdots & \vdots & \vdots & & \vdots & & \vdots \\ \frac{\partial \omega_N}{\partial \rho} & \frac{\partial \omega_N}{\partial (\rho u)} & \frac{\partial \omega_N}{\partial (\rho v)} & \frac{\partial \omega_N}{\partial E} & \frac{\partial \omega_N}{\partial \rho_1} & \cdots & \frac{\partial \omega_N}{\partial \rho_j} & \cdots & \frac{\partial \omega_N}{\partial \rho_N} \end{bmatrix}, \tag{E.1}$$

where the elements of the matrix are given as:

$$\frac{\partial \omega_i}{\partial \rho} = \frac{\partial T}{\partial \rho} \cdot W_i \sum_{k=1}^{K} \left[(\nu''_{ik} - \nu'_{ik}) \left\{ \sum_{l=1}^{N} (\alpha_{lk} c_{\chi l}) \right\} \left\{ \frac{dk_{f,k}}{dT} \prod_{l=1}^{N} (c_{\chi l})^{\nu'_{lk}} - \frac{dk_{b,k}}{dT} \prod_{l=1}^{N} (c_{\chi l})^{\nu''_{lk}} \right\} \right] \tag{E.2}$$

$$\frac{\partial \omega_i}{\partial (\rho u)} = \frac{\partial T}{\partial (\rho u)} \cdot W_i \sum_{k=1}^{K} \left[(\nu''_{ik} - \nu'_{ik}) \left\{ \sum_{l=1}^{N} (\alpha_{lk} c_{\chi l}) \right\} \left\{ \frac{dk_{f,k}}{dT} \prod_{l=1}^{N} (c_{\chi l})^{\nu'_{lk}} - \frac{dk_{b,k}}{dT} \prod_{l=1}^{N} (c_{\chi l})^{\nu''_{lk}} \right\} \right] \tag{E.3}$$

$$\frac{\partial \omega_i}{\partial (\rho v)} = \frac{\partial T}{\partial (\rho v)} \cdot W_i \sum_{k=1}^{K} \left[(\nu''_{ik} - \nu'_{ik}) \left\{ \sum_{l=1}^{N} (\alpha_{lk} c_{\chi l}) \right\} \left\{ \frac{dk_{f,k}}{dT} \prod_{l=1}^{N} (c_{\chi l})^{\nu'_{lk}} - \frac{dk_{b,k}}{dT} \prod_{l=1}^{N} (c_{\chi l})^{\nu''_{lk}} \right\} \right] \tag{E.4}$$

$$\frac{\partial \omega_i}{\partial E} = \frac{\partial T}{\partial E} \cdot W_i \sum_{k=1}^{K} \left[(\nu''_{ik} - \nu'_{ik}) \left\{ \sum_{l=1}^{N} (\alpha_{lk} c_{\chi l}) \right\} \left\{ \frac{dk_{f,k}}{dT} \prod_{l=1}^{N} (c_{\chi l})^{\nu'_{lk}} - \frac{dk_{b,k}}{dT} \prod_{l=1}^{N} (c_{\chi l})^{\nu''_{lk}} \right\} \right] \tag{E.5}$$

$$\frac{\partial \omega_i}{\partial \rho_i} = W_i \sum_{k=1}^{K} \left[(\nu''_{ik} - \nu'_{ik}) \left(\frac{\alpha_{jk}}{W_j} \right) \left\{ k_{f,k} \prod_{i=1}^{N} (c_{\chi i})^{\nu'_{ik}} - k_{b,k} \prod_{i=1}^{N} (c_{\chi i})^{\nu''_{ik}} \right\} \right]$$
$$+ W_i \sum_{k=1}^{K} \left[(\nu''_{ik} - \nu'_{ik}) \left\{ \sum_{l=1}^{N} (\alpha_{lk} c_{\chi l}) \right\} \left\{ k_{f,k} \frac{\nu'_{jk}}{\rho_j} \prod_{l=1}^{N} (c_{\chi l})^{\nu'_{lk}} - k_{b,k} \frac{\nu''_{jk}}{\rho_j} \prod_{l=1}^{N} (c_{\chi l})^{\nu''_{lk}} \right\} \right]$$
$$+ \frac{\partial T}{\partial \rho_j} \cdot W_i \sum_{k=1}^{K} \left[(\nu''_{ik} - \nu'_{ik}) \left\{ \sum_{l=1}^{N} (\alpha_{lk} c_{\chi l}) \right\} \left\{ \frac{dk_{f,k}}{dT} \prod_{l=1}^{N} (c_{\chi l})^{\nu'_{lk}} - \frac{dk_{b,k}}{dT} \prod_{l=1}^{N} (c_{\chi l})^{\nu''_{lk}} \right\} \right] \quad \text{(E.6)}$$

The derivatives of the temperature and the reaction rate constant in the elements of the matrix are written as

$$\frac{\partial T}{\partial \rho} = \frac{1}{\sum_{j=1}^{N} \rho_j R_j} \left[\frac{1}{1 - \sum_{j=1}^{N} \rho_j C_{p,j} \Big/ \sum_{j=1}^{N} \rho_j R_j} \left\{ -\frac{1}{2} \left(u^2 + v^2 \right) \right\} \right] \quad \text{(E.7)}$$

$$\frac{\partial T}{\partial (\rho u)} = \frac{1}{\sum_{j=1}^{N} \rho_j R_j} \left[\frac{u}{1 - \sum_{j=1}^{N} \rho_j C_{p,j} \Big/ \sum_{j=1}^{N} \rho_j R_j} \right] \quad \text{(E.8)}$$

$$\frac{\partial T}{\partial (\rho v)} = \frac{1}{\sum_{j=1}^{N} \rho_j R_j} \left[\frac{v}{1 - \sum_{j=1}^{N} \rho_j C_{p,j} \Big/ \sum_{j=1}^{N} \rho_j R_j} \right] \quad \text{(E.9)}$$

$$\frac{\partial T}{\partial E} = \frac{1}{\sum_{j=1}^{N} \rho_j R_j} \left[\frac{-1}{1 - \sum_{j=1}^{N} \rho_j C_{p,j} \Big/ \sum_{j=1}^{N} \rho_j R_j} \right] \quad \text{(E.10)}$$

$$\frac{\partial T}{\partial \rho_i} = \frac{1}{\sum_{j=1}^{N} \rho_j R_j} \left[\frac{1}{1 - \sum_{j=1}^{N} \rho_j C_{p,j} \Big/ \sum_{j=1}^{N} \rho_j R_j} \left\{ h_i - \frac{\sum_{j=1}^{N} \rho_j C_{p,j}}{\sum_{j=1}^{N} \rho_j R_j} R_i T \right\} - R_i T \right] \quad \text{(E.11)}$$

$$\frac{\partial k_{b,k}}{\partial T} = \frac{1}{K c_k} \left[\frac{dk_{f,k}}{dT} - \frac{k_{f,k}}{T} \left[\sum_{i=1}^{N} \left\{ (\nu''_{ik} - \nu'_{ik}) \frac{h_i}{R_i T} \right\} - \sum_{i=1}^{N} (\nu''_{ik} - \nu'_{ik}) \right] \right] \quad \text{(E.12)}$$

Appendix F

Preliminary Study of Cellular Structures at Experimental and Numerical Mixture Conditions

A 2-D simulation is performed with the same initial condition of Oran *et al*. (1998) and Eckett (2001); $2H_2+O_2+7Ar$, initially 6.7 kPa and 298 K. The same grid size and initial setup, including the size of perturbation to produce cellular structures, are used, except for the detailed reaction mechanisms. The present cell sizes are listed in Table F.1, and agree well with the previous results of Oran *et al*. and Eckett. The difference in cell sizes is expected to be caused by the different reaction mechanism. The present simulations are performed with the Jachimowski's reaction mechanism (1988), which is prepared for air-breathing engines in a space plane ($2H_2+O_2+3.76N_2$, 0.1 MPa), while a mixture simulated here is highly diluted with Ar and at extremely low initial pressure.

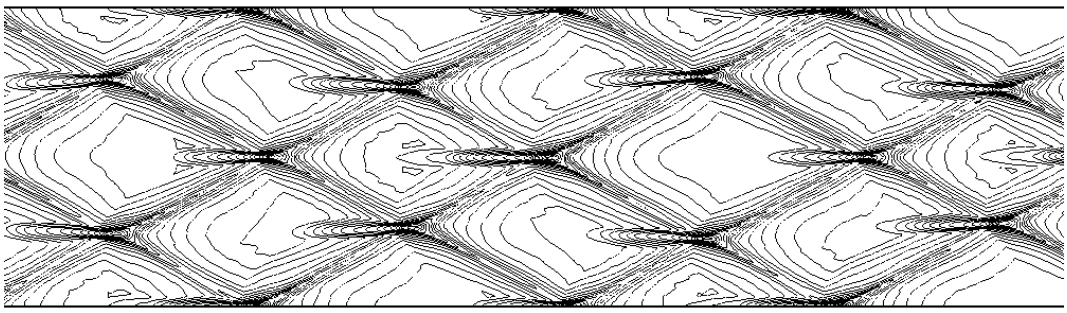

Figure F.1: Cellular structures for a 2-D C-J detonation in $2H_2+O_2+7Ar$, initially 6.7 kPa and 298 K.

Table F.1: Cell sizes for a 2-D C-J detonation in $2H_2+O_2+7Ar$, initially 6.7 kPa and 298 K.

	Cell length a (mm)	Cell width b (mm)	Aspect ratio a/b
Present simulation	59 ± 8.0	30 ± 2.0	2.0
Oran *et al.* (1998)	54	31	1.7
Eckett (2001)	55 ± 1.0	30 ± 1.0	1.8

A 2-D simulation is also performed with the same mixture condition of Strehlow & Crooker (1974). Although the 2-D tube width in the simulation is almost half of one of rectangular tube width in the Strehlow's experiment, the same number of transverse waves exists across a channel. Cell sizes listed in Table F.2 show a significant difference, except for a cell aspect ratio. The only way to accurately compute the natural cell size or distribution of cell sizes in a given mixture with given initial conditions is to use a channel sufficiently wide that many cells fit across its width (Eckett, 2001). Clearly, two and a half cells across the channel is inadequate in this respect, to say nothing of one transverse wave in §2.4 and 3. Cell width presented in those sections can be interpreted as the 2-D maximum cells, a rough estimate of the cell size, which are not affected by the "slapping" transverse waves in the third dimension for a square or rectangular channel. The regularity of cellular structure is also different between the numerical and experimental results. Although in the experiment, cellular structures have excellent regularity, the experiment are performed in the channel having a transverse dimension not much larger than the cell size, resulting in detonations with considerable wall losses. Decreasing the detonation velocity due to the wall losses reduces the post-shock temperature and pressure, thereby increasing the reaction length and other related chemical length scales, including the cell size. Therefore, the difference between experiments and simulations is expected to arise from above reasons.

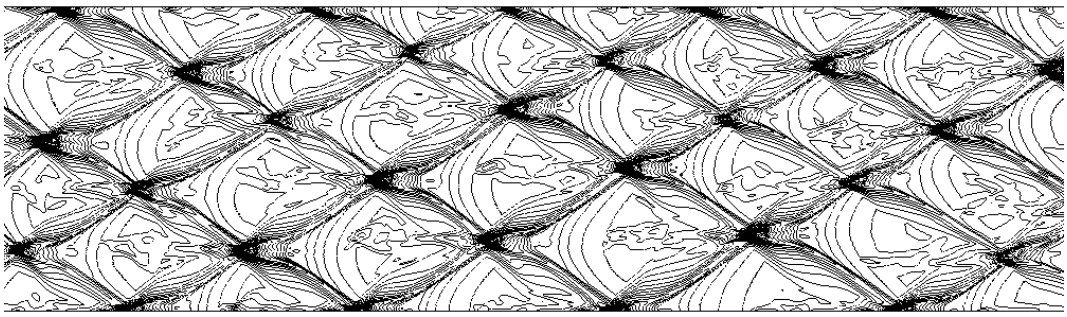

Figure F.2: Cellular structures for a 2-D C-J detonation in $2H_2+O_2+3Ar$, initially 7.7 kPa and 298 K.

Table F.2: Cell sizes for a 2-D C-J detonation in $2H_2+O_2+3Ar$, initially 7.7 kPa.

	Cell length a (mm)	Cell width b (mm)	Aspect ratio a/b
Present simulation	18 ± 2.0	10 ± 1.0	1.8
Strehlow & Crooker (1974)	47	26	1.8

Appendix G

Numerical Study of Pulse Detonation Rocket Engines (PDREs)

The application of detonation phenomena is famous for Pulse Detonation Engines (PDEs) in the aerospace industry. PDEs have received considerable attention in the past twenty years and significant progress has been made in their development. Numerical simulations of ethylene-oxygen PDEs will be presented and compared with experimental results (Kasahara *et al*., 2002). Since a study of the practical use of PDEs is not the main objective of the present research, the topic of PDEs is placed in Appendix G.

A PDE is an internal combustion engine in which fuel is repetitively burned as self-sustained detonation waves. Since a PDE is of simpler structure and of higher theoretical thermal efficiency compared with a conventional internal combustion engine based on isobaric combustion, research and development for its practical applications are being studied world-wide. A PDE is described simply as a straight tube with fixed cross section. One end of the tube, the thrust wall, is closed, and the other end is open. A detonation wave, initiated at the closed end, propagates toward the open end. When the detonation wave breaks out from the open end, a rarefaction wave starts to propagate from the open end toward the closed end. This rarefaction wave is reflected by the closed end.

The computational domain is axisymmetric (Fig. G.1). Before a detonation reaches the open end of the PDRE tube, the flow field in the tube was calculated one-dimensionally along the axis of the tube. Only after the time t_{CJ} (= 4.21 μs, time at which the detonation wave

reaches the open end of the PDE tube), is the flow field in the whole computational domain shown in Fig. G.1 calculated axisymmetrically. The initial gas pressure and temperature are, respectively, 0.101 MPa and 300 K in the whole computational domain. For ethylene reactions, an elementary-reaction model of Signh & Jachimowski (1994) is adopted to calculate the heat release and the chemical composition, where nitrogen is treated to be inert (Table G.1). With different species and their total numbers (Table G.2), CJ states (velocity, Mach number and specific heat ratio at the CJ condition) are derived from the chemical equilibrium calculations with AISTJAN. To reproduce CJ states, more than 9 species must be considered as shown in Table G.3. Singh & Jachimowski's reaction mechanism consists of above 9 species, but their mechanism can not reproduce characteristic reaction lengths obtained with the detailed reaction mechanism by Lutz *et al*. (1988). Therefore, an application of Singh's mechanism should be restricted for PDE simulations, which is not related to detonation structures.

To initiate the detonation wave, an initial blast wave is artificially set up in a thin high-pressure region, which is 3.0 MPa in pressure, 3000 K in temperature, and 0.5 mm in thickness, on the thrust wall. According to Fig. G.2, thrust wall pressure histories in numerical results show comparatively agreement with experimental results. Thrust wall pressures are slightly larger in numerical simulations than those in experiments, probably because heat loss and friction loss are not included in numerical simulations. Hence, the numerical results of specific impulse I_{sp} for different conditions in Table G.5 is also slightly larger than the experimental results.

Table G.1: Simplified ethylene reactions by Singh & Jachimowski (1994).
$k_{fl} = A_l T^{n_l} \exp(-E_l/RT)$ (cm^3-s-mol-cal-K).

	Reaction	A_l	n_l	E_l
1	$C_2H_4 + O_2 = 2CO + 2H_2$	1.80e+14	0.0	35500
2	$CO + O = CO_2 + M$	5.30e+13	0.0	-4540
3	$CO + OH = CO_2 + H$	4.40e+06	1.5	-740
4	$H_2 + O_2 = OH + OH$	1.70e+13	0.0	48000
5	$H + O_2 = OH + O$	2.60e+14	0.0	16800
6	$OH + H_2 = H_2O + H$	2.20e+13	0.0	5150
7	$O + H_2 = OH + H$	1.80e+10	1.0	8900
8	$OH + OH = H_2O + O$	6.30e+13	0.0	1090
9	$H + H = H_2 + M$	6.40e+17	-1.0	0
10	$H + OH = H_2O + M$	2.20e+22	-2.0	0

Thrid-body efficiencies for all thermolecular reactions are 2.5 for $M = H_2$, 16.0 for H_2O, and 1.0 for all other M.

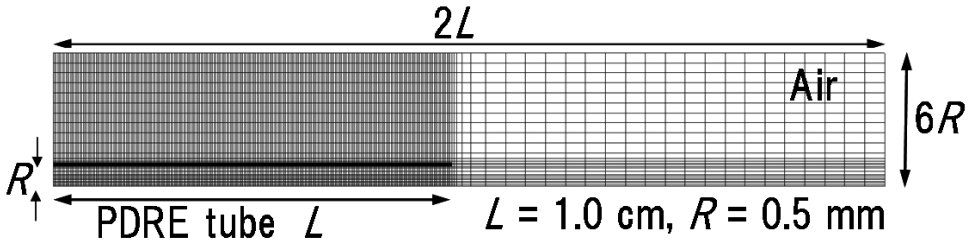

Figure G.1: Computational grid and geometrical conditions for PDRE simulations. (L: tube length; R: tube radius.)

Table G.2: Number and species for detonation simulations.

Number	Species	Notes
6 species	C_2H_4, CO_2, CO, H_2O, H_2, O_2	Baurle & Eklund (2002)
9 species	6 species + H, O, OH	Singh & Jachimowski (1994)
11 species	9 species + HO_2, H_2O_2	-
37 species	11 species + C, CH, CH_2, CH_2(S), CH_3, CH_4, HCO, CH_2O, CH_3O, CH_2OH, CH_3OH, C_2H, C_2H_2, C_2H_3, C_2H_5, C_2H_6, HCCO, HCCOH, CH_2CO, C_3H_2, C_3H_3, C_4H_2, C_4H_3, C_5H_2, C_5H_3, C_6H_2	Lutz *et al*. (1988)

Table G.3: Species number and C-J conditions in equilibrium state with those species.

Species number	D_{CJ} (m/s)	M_{CJ}	γ_{CJ}
6 species	2536.2	7.75	1.221
9 species	2376.4	7.26	1.239
11 species	2376.2	7.26	1.239
37 species	2376.2	7.26	1.239

Table G.4: Reaction mechanism and post-shock properties.

Reaction mode	T_{CJ} (K)	P_{CJ} (MPa)	L_{σ} ($\times 10^{-5}$ m)	$L_{Mach=0.75}$ ($\times 10^{-5}$ m)	$L_{Mach=0.9}$ ($\times 10^{-5}$ m)
Singh (1994)	3912	3.24	1.976	6.506	18.95
Lutz (1998)	3913	3.24	2.526	3.164	15.01

Table G.5: Specific impulse of numerical simulations and experiments. (1-D: one-dimensional results; 2-D axi.: two-dimensional axisymmetric results; Exp.: experimental results.)

Case	1-D		2-D axi.		Exp.	
	I_{sp} (s)	period ($1/t_{CJ}$)	I_{sp} (s)	period ($1/t_{CJ}$)	I_{sp} (s)	period ($1/t_{CJ}$)
100 % Full	178	9.48	174	9.14	157	8.60
50 % Air	245	8.18	243	7.96	207	6.36
50 % He	186	6.90	185	6.68	161	5.57

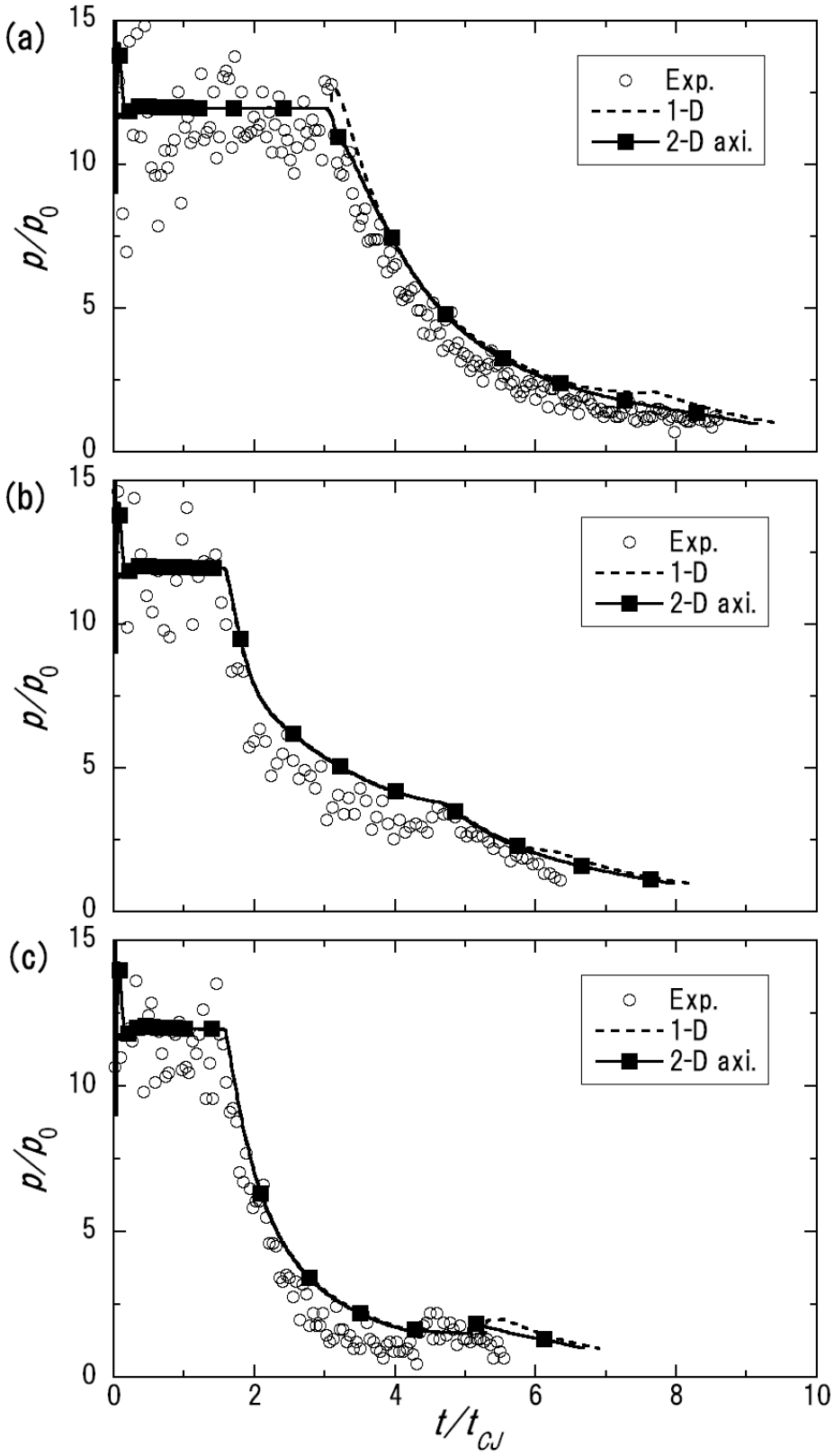

Figure G.2: Thrust wall pressure histories of experiments and 1-D & 2-D axisymmetric numerical results. (a) 100 % Fuel fill, (b) 50 % Air fill, (c) 50 % He fill.